

Chapter 8

Thermal Transformations of Polymeric Metal Chelates and Their Precursors in Nanocomposites Formation

Abstract The thermal transformations of polymeric metal chelates and their most typical precursors, resulting in the formation of nanocomposite materials, are considered. The attention is focused on the methodology of thermolysis including thermogravimetric, linear pyrolysis, volumetric, spray, chemical vapor deposition approaches as well as thermolysis under the action high-energy radiation. The metal chelates as «single-source» precursors are readily decomposed both in the pure state and the polymer matrix due to the formation of the polymeric shell by the destruction of the organic fragment. A new approach using metal chelate monomers as precursors (the conjugate thermolysis) is also considered. This method involves a simultaneous polymerization of monomers and the formation of metal-containing nanoparticles during the thermal transformation. Depending on the nature of the polymeric metal chelates and thermolysis conditions, different nanomaterials (for example, carbon, metal oxide, mixed-oxide, non-oxide nanocomposites, etc.) can be formed.

Existing methods of obtaining nanomaterials can be reduced to two fundamentally various ways: «top down» (descending way) or «bottom-up» (ascending way). The first one consists in grinding all sorts of large particles to nano-sized, «bottom-up» method is in the assembly of nanoparticles from individual atoms (or ions with following reduction) to a predetermined size of nanoparticles in the presence of the polymer matrix (or its precursor). The latter method, because of its diversity and potential, is more widely used than «top down» approach. The researcher can predict in advance the characteristics of the prepared nano-sized particles: choose the composition and properties of the starting components, stabilizing agents, to evaluate their role, to predict the conditions of nucleation and growth of nano-sized particles at all stages of design of the targeted nanocomposites. Properties that can be achieved in such materials are strictly dependent on the synergy between organic and inorganic nature of the components and surely defined nanostructure and the extent of their organization.

Among the known «bottom-up» approaches, high-temperature thermolysis of metal-containing samples is a general method allowing to preparing nanomaterials

with low crystalline defects, narrow size distribution, and regulated shapes [1, 2]. Many interesting concepts, for example, size distribution focusing, selective adhesion shape control and branching, have been developed [3–6]. It should be noted that solid-state thermolysis of different metal chelates is a promising way to the preparation of novel nanostructured materials.

Of particular interest are the polymeric metal chelates which thermal decomposition under different conditions is widely studied in order to obtain metal-containing nanocomposites with tunable sizes and morphologies [7–26]. It is important that various nano-sized materials, for example, metals, metal oxides, metal sulfides and metal halides, can be obtained using PMC or their precursors.

In this chapter, we analyze thermolysis as one of the comfortable, well-reproducible and easily controlled methods of nanocomposites formation an example of different types of metal chelates.

8.1 Thermolysis Methods of Polymeric Metal Chelates

The study of thermal transformations can be carried out using methods of external and internal heating as in isothermal and non-isothermal conditions, in closed or open systems. Depending on tasks the various methods are possible to control the degree of conversion, which determine the choice of equipment for the experimental study of the compounds thermolysis. First of all, it is the weight (thermogravimetry) or volumetric (volumetry) methods. In recent years, there is a tendency to design complex (synchronous) devices that simultaneously combine in a single device several ways for the conversion control in conjunction with their automation, using the capabilities of modern computer technology. We briefly analyze the specifics of the main methods used to study the kinetics of thermal decomposition (thermal degradation) of metal-containing compounds. Thermogravimetric analysis (TGA), differential scanning calorimetry (DSC), thermodilatometry and thermo-mechanical analysis, dielectrical analysis, micro- and nanoscale thermal analysis, including atomic force microscopy (AFM) and scanning thermal microscopy (STM) are the most frequently used methods of thermal analysis of different compounds, including metal-containing.

8.1.1 *Thermogravimetric Methods*

Their essence is to measure the relative change in the material weight as a function of temperature during its transformation with a programmed heating. Linear temperature dependence on time is usually used, sometimes TGA combined with tensimetry, in which the substance weight and gassing analysis is carried out simultaneously, usually under isothermal conditions in a dynamic vacuum and can be detected both continuously and discretely. To do this, a spring balance uses

during the study of the kinetics of consumption of volatile products of thermolysis. Modern thermobalance allow continuously (automatically) detect the variation of the sample weight (Δm) of time of the temperature. TGA methods are mostly the traditional non-isothermal variants of linear heating method.

At present, the different thermogravimetric variants found widespread use: differential thermogravimetry (DTG), when weight variation m of the time t (i.e. dm/dt) or of temperature (dm/dT) is recorded; differential thermal analysis (DTA), wherein the temperature difference between the reference and the substance is measured as a function of temperature at a programmed heating. It should be noted the development of a new research method called differential scanning calorimetry (DSC) to increase in the accuracy of quantitative determination of the thermal effects [27].

When the programmed heating rate such concepts as the temperature of the decomposition onset, the decomposition stages, the temperature ranges of stability of the intermediate compounds are the kinetic characteristics of the process [27]. To reduce the distortions introduced by the uncontrolled pressure and by the permanently increasing temperature, a new technique of TGA experiment was developed, which became the basis for the quasi-isothermal quasi-isobaric thermogravimetry method [28]. The principle of the method is based on a fine adjustment of heating, allowing keeping the constant weight change rate or constant pressure.

8.1.2 *Linear Pyrolysis Method*

Linear pyrolysis (LP) is a steady-state one-dimensional propagation of the reaction front of the thermal transformation in a condensed phase when heat is supplied from an external source [29]. LP is carried out in two regimes depending on the relationship between the parameters. In the first kinetic regime, pyrolysis macrokinetics coincides with the true kinetics of decomposition and $E_{\text{eff}} \approx E_{\text{tr}}$. The second route is internal diffusion regime (by heat), when $E_{\text{eff}} \approx E_{\text{tr}}/2$. LP method allows to studying the kinetics of fast high-temperature processes in condensed phase, for which to a change in the rate-limiting stage of the chemical transformation often takes place during the transition from one temperature region to another. The principle of operation of the devices based on LP-method is that the sample of the tested substance is constantly pressed upon the surface of the heating plate at constant temperature.

8.1.3 *Volumetric Methods*

Volumetric methods allow to studying the decomposition of small amount of a substance and to investigating the dependence of the volume of the evolved gas [$V(t)$] by discretely or continuously manner. The main disadvantage of pressure gauge units

is direct contact of gaseous products which can be chemically aggressive with the corroding metallic parts and mercury. Therefore, the using glass membrane type pressure gauges, where there are no metallic parts, is the more promising. The undoubted advantages of such setups are short response times, which allows to studying the rates of fast processes in a close reactor space by means of a Bourdon membrane-type pressure gauge. It should be noted that gas evolution during the thermal transformation proceeds in a self-generated atmosphere (SGA). Such method was called RAPET (Reaction under Autogenic Pressure at Elevated Temperature) (see, for example [30]).

8.1.4 Thermolysis Induced by High-Energy Radiation

This method is based on sample exposed to high frequency (HF) electric field as alternative source of heating [31–33]. Its essence lies in the fact that polar units of polymer molecules are oriented in accordance with change of polarity of a variable electric field. At the same time, thermal motion as well as other units hinders such orientation. Energy is spent on overcoming the disorientation of the polar units, as a result of which it dissipates and heats the sample. The electric field strength and frequency of oscillations are the main factors determining the intensity of heating. The absence of contact in the entire volume of the test sample is the main advantage of HF heating. Thus, the effect of high-frequency heating (the heating temperature can reach 510 K) with a frequency of 100–300 MHz of polymers containing electrically conductive metal-containing fillers or soot having a particle size of less than 500 μm in an amount of up to 85% of the weight of the material allows the production of a homogeneous composite material. In another example, the heating temperature reaches 495–770 K during heating metal-containing samples in a muffle oven and exposing to a 2450 MHz electromagnetic field with a 700 W power [34]. The prepared products are characterized by a pronounced crystalline structure, high surface area and particle sizes in the nanometer scale.

8.1.5 Spray Pyrolysis

By nature and design, such method is different from the above-mentioned procedures and is an efficient alternative method for obtaining metal and their oxide nanoparticles in the form of powders on a large scale, ceramics, nanostructured materials [35, 36]. Of substantial interest are also the ultrasound-, laser-, plasma-pyrolysis as and flame spray pyrolysis [37–39].

The aerosol spray pyrolysis is a promising strategy for increasing both surface area and crystallinity, enabling sequential, easy, and large-scale production of metal oxide spheres [23, 40–45].

Usually, spray pyrolysis proceeds in five main stages [46]. Although some stages of spray pyrolysis [47] continue to be developed (for example, drop formation [48], evaporation and drying [49], spray through a variety of devices - sprays, atomizers, ultrasonic generators, etc.), however so far there is no deep understanding of the effect the change of reaction conditions (concentration, flow rate, evaporation-precipitation stage of thermolysis) on the mechanism and the possibility of control of uniform nanoparticle formation. The most significant influence on the nanocrystal formation has a temperature. Nanocomposites based on metal oxides obtained by spray pyrolysis, described in sufficient detail (see, for example, [50–57]).

Intensively developing are new areas of gas phase synthesis in the condensed phase for the preparation of new ceramic materials. Of great synthetic potential is the flame spray pyrolysis, including aqua and non-aqua sol-gel technique, hydro- and solvothermal methods, pyrolysis of polymeric materials and high-pressure technique.

8.1.6 Chemical Vapor Deposition

Various variants of vapor deposition technology are commonly used for the preparation of metal-polymer nanocomposites [58, 59]. Their essence is combined or sequential deposition of metal and organic components and the metal nanoparticle formation in the growing composite film. Active metal atoms during the collision with the polymer surface may diffuse into the bulk polymeric matrix trapped by the surface defects, collided with each other, leading to aggregation and formation of cluster particles. The volume fraction of metal nano-sized particles in a polymer film can be regulated by the ratio of deposition rates of metallic and polymer components [60]. Methods of chemical vapor deposition of organometallic precursors are widely used for the preparation of semiconductor film materials [61, 62]. Metal chelate in gas-phase processes for obtaining nanocomposite materials have a number of advantages, because due to the presence of components with preformed bonds they may lead to a quality defect-free products with a stoichiometric composition [63], including thin-film materials based on cadmium [64, 65], iron [66, 67], antimony and bismuth sulfides [68], etc.

8.2 Metal Chelates As «Single-Source» Precursors of Nanocomposites

The synthetic strategy for the preparation of nanostructured materials is often based on the thermolysis of «single-source» precursors (SSP) into hot organic solvent. Usually it is also called «TOPO method», where TOPO is tri-*n*-octylphosphine

oxide, in which chelating precursor dispersed in tri-*n*-octylphosphine (TOP) or TOPO reacts with the metal compound in the hot surfactant/solvent at temperatures up to 350 °C to form metal-containing nanoparticles [69]. Despite the pervasiveness such approaches starting from two or more precursors they have limitations due to the fact that the formation of the nanocrystal often depends on the relative reactivity of these composite components, their stability, etc. Many of these problems, including the use of toxic and volatile compounds at high temperatures can be avoided if the precursors are metal chelates, which combine in one molecule as a metal ion, and composite elements, for example, chalcogenides to produce semiconductor nanoparticles. Typically, metal chelates are easily synthesized, stable with respect to moisture and atmospheric oxygen at room temperature, safe and in many cases lower cost-effective than multicomponent systems [70–72]. Besides, good scalability and controllability of the thermolysis process of metal chelates in the preparation of nanocomposites based on them are also attractive.

Equally important is the fact that the PMC thermolysis analysis is usually carried out by comparison with low molecular weight analogues, which are used as monomeric metal chelates. Therefore, the study of the kinetics of thermal transformations of metal chelates and the structure of the resulting products is important for the understanding of the general laws of PMC thermolysis.

The range used to date metal chelates is quite wide, including a variety of metals and chelating ligands. Among the most interesting examples of molecular metal chelates we note synthesis of magnetic Co₃O₄ nanostructures via a facile thermal treatment method at 700 °C by using *trans*-Na[Co(L)₂(NO₂)₄] \cdot H₂O (L is hexamethylenetetramine) as a precursor [73]. The target Co complex provides good conditions for preparation of magnetic octahedral nanostructures in a facile and surfactant-free method. It is found that the Co₃O₄ nanostructures exhibit a ferromagnetic behavior with a saturation magnetization of 8.69 emu g⁻¹ and a coercivity of 305.3 Oe at room temperature. In another example the chelating ligand 2,2'-diamino-5,5'-dimethyl-4,4'-bithiazole (L) was also used for obtaining Co₃O₄ nanoparticles [74]. In particular, Co₃O₄ nanostructures were prepared by direct thermolysis of nanoscale and single crystals of an azido Co(II) complex [Co(L)₂(N₃)₂] \cdot 0.25CH₃OH at 450 °C under air. It should be noted that the CdS nanoparticles were obtained using Cd(II) complex [Cd(L)₂(NO₂)₂] based on the same ligand as precursor via thermal decomposition [75]. However, during thermal decomposition of [Cd(L)₃](ClO₃)₂ an oxide-sulfide nanocomposite CdO–CdS was prepared [76].

The study of mechanism of thermolysis of bpy chelates of Zn(II) and Cd(II) [77, 78] as well as Ni(II) [79] and Fe(II) [80] is based on the composition and structure of the prepared products. In particular, thermolysis of tric(bpy)-Fe(II) dichloride proceeds in two stage (Fig. 8.1).

We note corresponding metal oxide nanocomposites/binary oxides obtained by heating of the heterometallic complexes [M₂Mn(OAc)₆(bpy)₂], where M=Cu, Co, Zn [81].

The thermolysis of [M(en)₂](NO₃)₂ (M=Cu, Co, Ni and Zn) chelates proceeds in two stages through evolving en and monoethylene diamine molecules and the

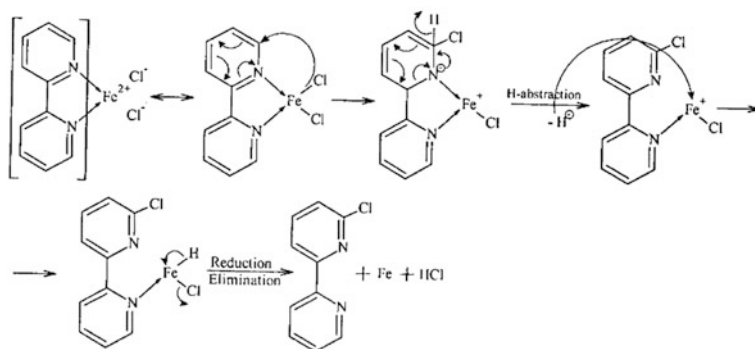


Fig. 8.1 Mechanism of thermal decomposition of tric(bpy)iron(II) dichloride to Fe(0) in an inert atmosphere

formation of high-dispersed metal oxides [82]. The process kinetics corresponds to second- and third-order equations, respectively.

The controlled thermolysis of $[\text{Ni}(\text{en})_2(\text{H}_2\text{O})_2](\text{NO}_3)_2$ chelate leads to the formation of nanocrystalline nickel (18.1 nm) [83]. The kinetics of a solid phase thermolysis of tris (ethylene diamine) nickel (II) sulphate includes two-stage deamination and two-stage decomposition [84].

Melt thermolysis was used to produce different Pd nanostructures based palladium complex with bis-1,2,4-triazole ligand [85]. Interestingly, the binding of the ligand to the metal atom is carried out by means of four N atoms of four 1,2,4-triazole groups without sulfur atoms. This type of coordination leads to the formation of spiro-metallocycle Pd(II) complex (Fig. 8.2). Depending on the temperature and atmosphere in which the complex thermolysis is carried nanoparticles of metallic Pd(0) (800 °C in N_2 medium) or Pd(0)-, Pd-PdO-, PdO- and Pd-PdO-nanostructures can be obtained at temperatures of 300, 500, 700 and 800 °C in air, respectively.

Numerous studies devoted to the investigation of the thermolysis of metal chelates of intracomplex type, in particular metal acetylacetonates. Thus, nanocrystalline $\alpha\text{-Al}_2\text{O}_3$ powders were prepared [86] by pyrolysis of $\text{Al}(\text{acac})_3$. The optimum calcination temperature of the precursor powder for crystallization of nano $\alpha\text{-Al}_2\text{O}_3$ was 1000 °C for 2 h. It was shown that the obtained materials could be modified from segregated nanoparticle to aggregates of nanoparticle with decrease in the volume ratio of alumina to acac from 8:2 to 5:5 in the precursor solutions.

The CdO nanoparticles (45 nm) were obtained by thermolysis of an azaromatic base adduct of Cd(II) thenoyltrifluoroacetate, $[\text{Cd}(\text{phen})(\text{TTA})_2]$, at 180 °C with oleic acid as a surfactant [87]. It is important that as a result of this reaction CdO nanoparticles are formed, in comparison with CdS formation from Cd/S-ligand complexes in the majority of the reactions below.

It should be noted using liquid-feed flame spray pyrolysis [88] for synthesis of Mg-Fe-based mixed-metal nanopowders in the $(\text{MgO})_x(\text{Fe}_2\text{O}_3)_{1-x}$ system from

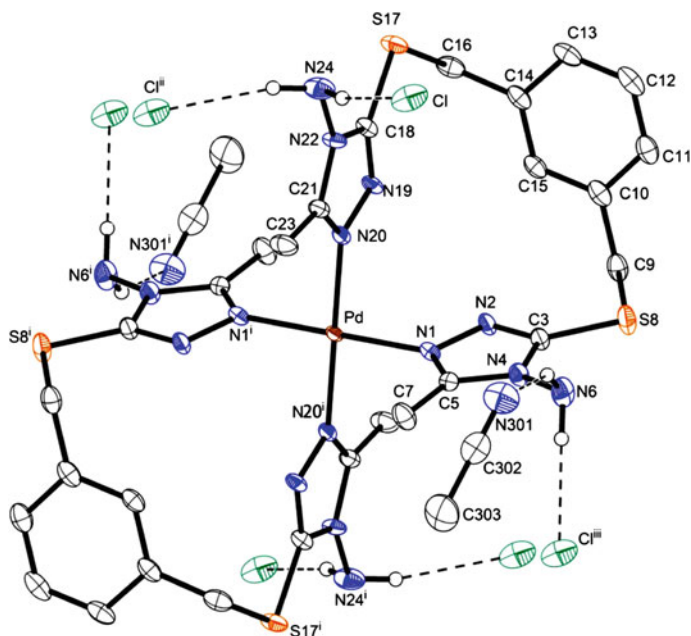
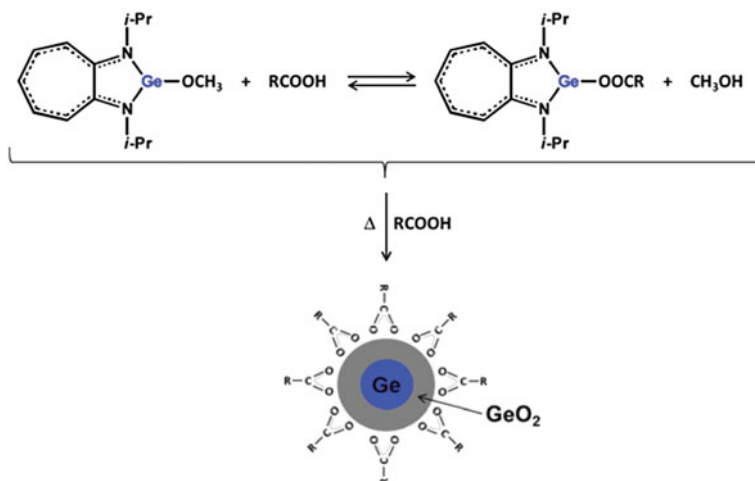


Fig. 8.2 The molecular structure of the metal chelate $[PdL_2]Cl_2 \cdot 4CH_3CN$ ($L = 5,5'-(1,3\text{-phenylenebis(methylene))bis(sulfanediy)bis(3-methyl-4H-1,2,4-triazol-4-amine)}$)

metal-complex precursors. Iron propionate $[Fe(O_2CCH_2CH_3)_3]$ and magnesium acetylacetonate $[Mg(acac)_2 \cdot 2H_2O]$ precursors were dissolved in ethanol, aerosolized with oxygen and combusted at $1500^\circ C$ and thereafter quenched rapidly. Final powders had a range of compositions ($x = 0.30, 0.45, 0.50, 0.65, 0.75,$ and 0.90 ± 0.02) and particle sizes generally increased as the fraction of MgO increased.

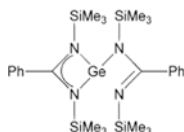
Of interest is a simple method of the preparation of nano-sized Co_3O_4 , which is important p-type semiconductor with catalytic, gas-sensor and electrochemical properties [89–91]. This method based on a solid-phase thermolysis of the metal chelate precursor—bis(salicylaldehyde)₂cobalt(II) at 773 K for 5 h in air [92, 93].

The key role of ligands and their dynamics during the nanoparticle synthesis can be clearly illustrated by the preparation of Ge/GeO₂ nanoparticles with core-shell structure with a mean diameter close to 5 nm with a narrow size distribution ($<15\%$). It was shown [94] that oleic acid, in addition to the stabilizing function is involved in the mechanism of thermal decomposition of the aminoimate germanium(II) (ATI)GeZ complex ($Z=OMe, NPh_2, ATI=N,N'$ -diisopropylaminotroponimate). Equilibrium is established between the initial metal chelate and formed intermediate (ATI)GeOI (OI is oleate) even at room temperature during mixing of (ATI)GeOMe with an acid (Scheme 8.1). Substitution of oleic acid by hexadecylamine (HDA) or its mixture with oleic acid does not lead to the nanoparticles formation. In this case it is also important that the original complex



Scheme 8.1 Mechanism of Ge/GeO nanoparticle formation by thermal decomposition of (ATI)GeOMe

(ATI)GeOMe is also in the reaction system. Note that the use of separately obtained (ATI)GeOI complex to produce nanoparticles is unsuccessful. It is assumed that the presence of the original complex (ATI)GeOMe in the system is necessary for the nucleation process, while the oleic acid promotes the decoordination of strong chelating ATI ligand by acidic proton. If in this example thermolysis is carried out at 320 °C, the use of a weaker chelating ligand as amidinate can significantly reduce (up to 160 °C) operating temperatures of the synthesis of germanium nanoparticles [94].



The most detailed study of the thermolysis kinetics and the structure of the resulting products were carried out by the example of chalcogenide and azomethine metal chelates.

8.2.1 Chalcogenide Metal Chelates

Currently, a wide variety of compounds as the metal dithio/diselenocarbamates and imino-bis(diisopropylphosphine)selenides [95–97], and Cd(TePh)₂ [98] or Zn

(TePh)₂ [99] are used as SSP for the synthesis of CdS, CdSe, ZnSe, CdTe/ZnS and other nanocrystals. A wide selection of solvents and surfactant molecules, varying the synthesis conditions allow largely to control the properties of the final products and to obtain materials with desired characteristics.

Thus, the hexagonal microcrystalline zinc oxide was prepared using Zn(II) cysteine complex [ZnI₂(L)]_n (L is 2-amino-3-mercaptopropanoic acid) as precursor by calcination at 600 °C for 2 h [100]. Pure greenish-blue cobalt chromite (CoCr₂O₄) nanoparticles having narrow particle range of 4.1 ± 1.9 nm and surface area of 78.2 m² g⁻¹ were prepared by the thermolysis of mixed metal chelates with chelating 2-mercaptopyridine N-oxide sodium salt [101]. Thermolysis led to the formation of nanoparticles with high surface area due to releasing a large amount of gas. It is important that the particle size reduction depends on the temperature and time of thermolysis.

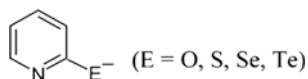
Dimeric cadmium(II) chelate with S-benzylthiocarbamate (L), [Cd(L)Cl₂]₂ was used for the bulk synthesis of CdS nanorods [102]. It should be noted that the decomposition of the chelate was carried out by heating at 160 °C in hexamethylenediamine (HMDA) to form amine capped CdS nanocrystals (rods) with yield ca. 90%.

Of interest is a template-free preparation of CdS microflowers by thermolysis of cadmium thiocyanate complex at 300 °C under open atmosphere [103]. The microflower morphology was self-assembled by intact thin nano-sheets.

It is important to underline that the concentration of the monomer precursor, the reaction temperature, stabilizing agents is important factors that determine the regime (thermodynamic or kinetic) in which the reaction occurs [6]. The high reaction temperatures and low monomer concentration promote the thermodynamic growth regime to the formation of isotropic nanocrystals. In contrast, kinetic nonequilibrium conditions caused by low reaction temperatures and high precursor concentrations lead to anisotropic structures (rods, tetrapods, etc.).

8.2.1.1 Influence of the Ligand Nature

Dialkylthiocarbamates [65, 104–107], thiosemicarbazides [108], xanthates [109, 110], thiourea [111, 112], dialkylchalcogenephosphates, dichalcogenimidophosphates [113] are the most commonly used chelating ligands of SSP. We note also that one of the most interesting families of chelating ligands for the synthesis of SSP is chalcogenopyridines:



Metal chelates of 2-thio [114] and 2-selenopyridines [115, 116] are well known, while the coordination chemistry of 2-telluriumpyridines begins to develop only [117, 118].

The nitrogen-containing chelating ligands like ppy, bpy, phen have a significant effect on the thermal stability and volatility of the chalcogenide metal complexes [119–121]. This thermal behavior is often confirmed by step weight loss character during TGA. In particular, two stages of thermal decomposition at temperatures of 130 and 320 °C are typical for the pyridine adduct of bis(piperidine dithiocarbamate) cadmium(II) [Cd(pip-dtc)₂] [62], the first of which corresponds to a loss of Py ligand (Fig. 8.3a). In contrast, dithiocarbamate Cd(II) complexes, which does not contain donor adducts, decompose single-stage at 331 and 320 °C with weight loss of 64.9 and 70.9% for the piperidine [Cd(pip-dtc)₂] and tetrahydroquinoline [Cd(thq-dtc)₂] complexes, respectively (Fig. 8.3b) [61]. The non-volatile residues represent 35.1 and 29.1%, that is slightly higher than the estimated values of CdS (33.4 and 27.3%), obtained from these complexes.

A similar thermal behavior is typical for Zn(pip-dtc)₂ and Zn(thq-dtc)₂ complexes. Their thermograms show a single-stage weight loss corresponding to thermal decomposition of the organic ligand with the endothermic peak on the DSC curves at 341.9 °C ($\Delta H = 214.3 \text{ J g}^{-1}$) and 294.5 °C ($\Delta H = 188.0 \text{ J g}^{-1}$) for Zn(pip-dtc)₂ and Zn(thq-dtc)₂ complexes, respectively [122]. At the same time a two-stage decomposition is observed with a weight loss at 210 (15.6%) and 304 °C (65.5%) in the case of Fe(pip-dtc)₃ [123]. According to the proposed mechanism based on the thermal analysis and gas chromatography-mass spectroscopy (GC-MS) the detachment of one of the three dtc ligand (*m/z* 160) proceeds initially to form a four-coordinated intermediate and then a final removal of organic components (*m/z* 290) leads to the final FeS (*m/z* 86) product (Scheme 8.2).

As seen from these examples, in the absence of donor adducts relatively high temperatures are required for decomposition of metal chelates of the considered type to form the desired metal sulfide nanoparticles. An interesting example is the metal chelates, which contain in addition to dithiocarbamate groups and other chelating ligands, in particular, bpy or phen (Fig. 8.4).

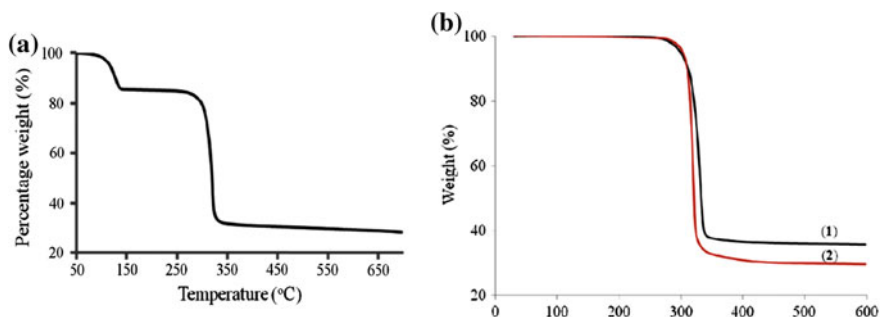
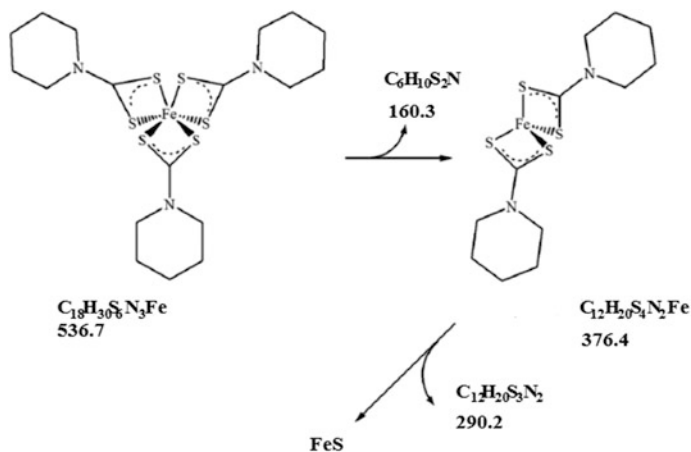


Fig. 8.3 Thermogravimetric curves for complexes of **a** [Cd(pip-dtc)₂(Py)] and **b** Cd(pip-dtc)₂ (1) and Cd(thq-dtc)₂ (2)



Scheme 8.2 Scheme of the thermal decomposition of $\text{Fe}(\text{pip-dtc})_3$

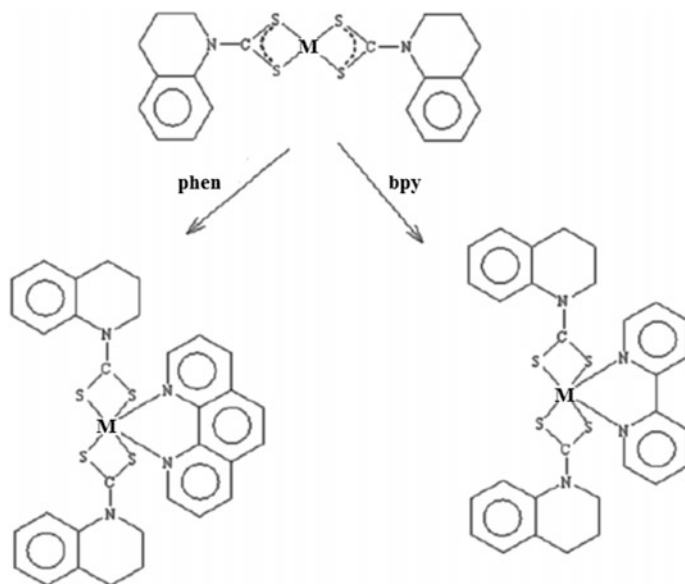
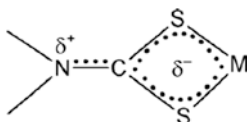


Fig. 8.4 Structure of $[\text{Cd}(\text{thq-dtc})_2]$ complexes with additional chelating ligands phen or bpy

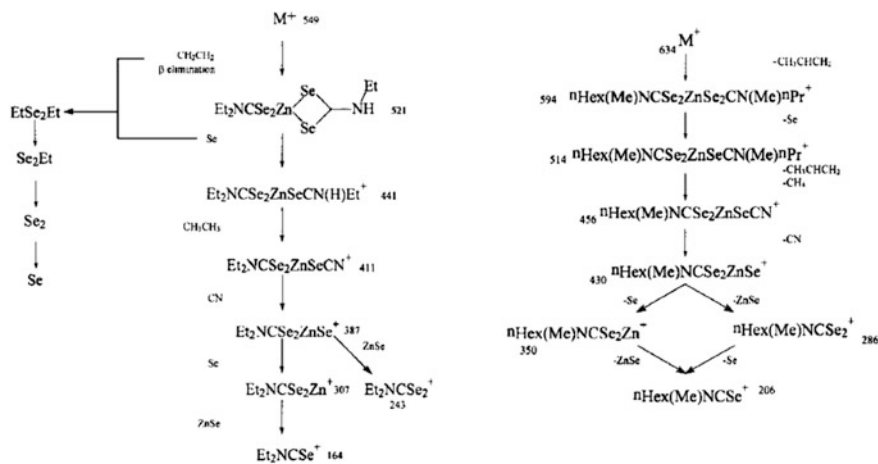
Additional nitrogen donor atom coordination with metal dithiocarbamate during the formation of adducts causes loosening of partially dual nature of nitrogen-carbon bond and as the result the redistribution of electron density from the carbon to the nitrogen atom in the dtc group:



As a rule, M–S bond elongation is observed in such complexes [62, 99], which is explained by an increase in the CN, and the steric influence of donor ligands. Depending on the nature of the substituent on the nitrogen atom in diseleno- and dithiocarbamates symmetrical diselenocarbamate complexes produced selenium clusters during the thermal decomposition, while metal selenides are formed in the case of asymmetric diselenocarbamates [124]. By mass spectrometry with electron ionization (electron ionization mass spectrometry EI–MS) and high resolution pyrolysis GC–MS analysis it shown that slight differences in the alkyl substituents on the nitrogen atom of the diselenocarbamate ligand of $\text{Zn}(\text{Se}_2\text{CNET}_2)_2$ and $\text{Zn}(\text{Se}_2\text{CNMe}^n\text{Hex})_2$ complexes are responsible for the two routes of their decomposition with the formation of Se_n clusters ($n = 1\text{--}7$) from the intermediate diethyldiselenide EtSe_2Et in the first case, and stable five-membered intermediate dihydroselenazole $\text{Zn}(\text{Se}_2\text{CNMe}^n\text{Hex})_2$ in the latter case, which completely eliminates from system and the final product thermolysis is metal selenide (Scheme 8.3).

8.2.1.2 Environment Influence

Palladium sulfide Pd_4S nanoparticles of various shapes were obtained from the single-source complex $[\text{PdCl}_2(\text{PhS-CH}_2\text{CH}_2\text{CH}_2\text{-NH}_2)]$. Thermolysis of 3-phenylsulfonylpropylamine complex of palladium chloride (Fig. 8.5) at 195 °C in oleylamine leads to the formation of flower shaped nanoparticles, whereas Pd_4S nano-



Scheme 8.3 The main routes of decomposition of the complexes $\text{Zn}(\text{Se}_2\text{CNET}_2)_2$ and $\text{Zn}(\text{Se}_2\text{CNMe}^n\text{Hex})_2$ according to data of EI–MS and high resolution pyrolysis GC–MS analysis

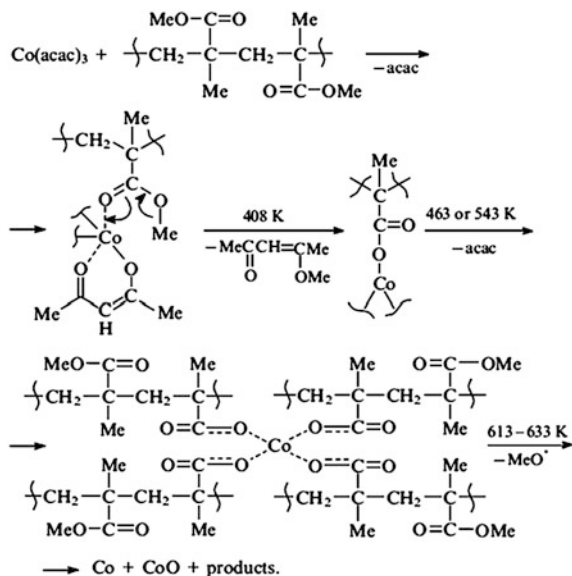


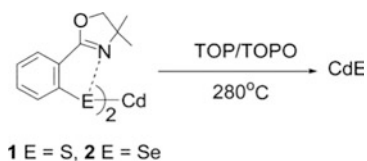
Fig. 8.5 The scheme for obtaining nanoparticles of palladium sulfide from molecular precursor $[\text{PdCl}_2(\text{PhS}-\text{CH}_2\text{CH}_2\text{CH}_2-\text{NH}_2)]$, where OA is oleic acid, ODE is octadecene, and OAm is oleylamine

spheres are formed in oleic acid and octadecene mixture (1:1) [125]. Perhaps the flower shape of the obtained nanoparticles is determined by the stronger complexing and reducing properties of oleylamine [126, 127].

It is important that the shape of the resulting nanoparticles is not changed by their attachment to the graphene oxide as a carrier and has a significant influence on the catalytic properties of these nanocomposites.

The determining factor in the anisotropic growth of nanocrystals is the surface energy of the crystallographic plane which can be modulated by the selective adsorption of surfactant molecule on the surface [128]. CdS nanoparticles were prepared during the thermal decomposition of $\text{Cd}(\text{pip-dtc})_2$ or $\text{Cd}(\text{thq-dtc})_2$, and their growth is effectively controlled using capping agents of HDA and TOPO of various concentrations [129]. When thermolysis was performed in HDA medium known by dynamic nature of adsorption on the crystallite surface due to its mobility sufficiently it provides monomeric species access, on the one hand and aggregation preventing of the other. As a result the obtained nanoparticles have the shape of rods, dipodies and tripods (Fig. 8.6).

When TOPO was used as a surfactant the quasi-spherical CdS nanoparticles with an average size of 4.33 ± 0.59 nm was formed. A similar pattern was observed during the preparation of ZnO nanoparticles from $\text{Zn}(\text{pip-dtc})_2$ and $\text{Zn}(\text{thq-dtc})_2$ complexes in TOPO medium [130]. Interestingly, thermolysis of $\text{Cd}[\text{E}(\text{L})_2]$ [E = S, Se; L = 2-(4,4-dimethyl-2-oxazoliny)benzene] in TOPO medium at 280 °C led to cadmium sulfide or selenide nanoparticles with a sufficiently large size up to 200 nm according to the following scheme [131]:



We note that the solution colloidal synthetic methods of chalcogenide nanoparticles preparation in TOP/TOPO medium are widely used [66, 119, 132], despite the high temperature reactions (200–350 °C) and the use of air-sensitive and highly toxic reagents, since they allow to obtain crystalline monodisperse, defect-free particles. Approach [133–135] based on the thermolysis of SSP of metal alkylxanthate type (dithiocarbamates, trithiocarbonates, dithiophosphates) in the medium

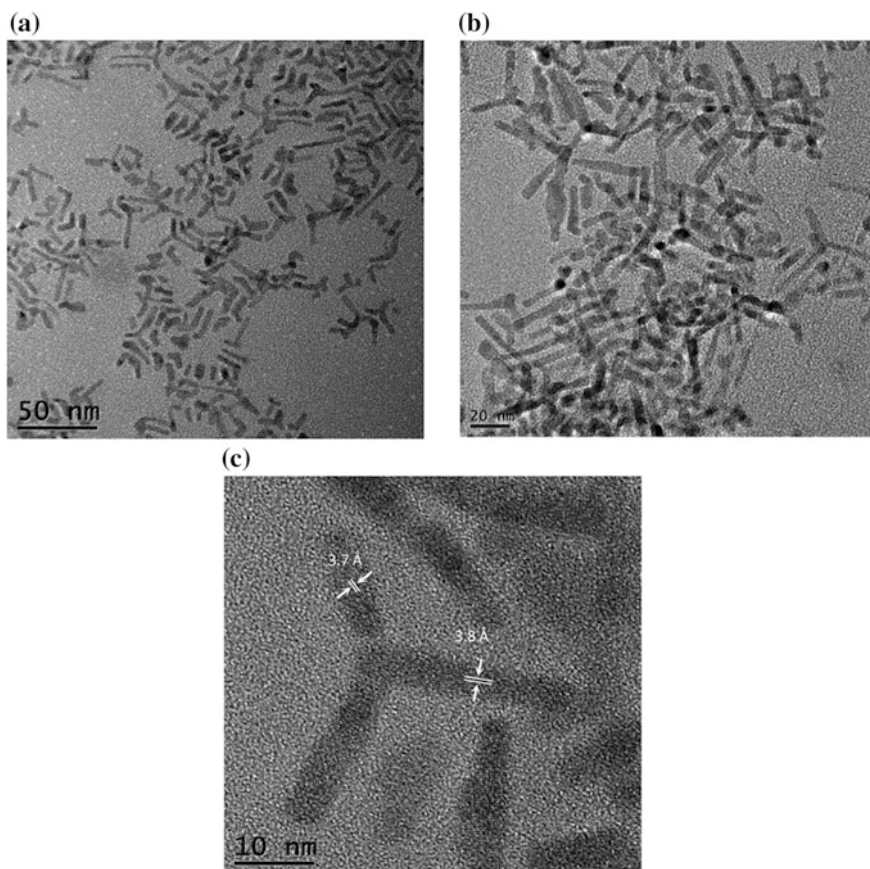
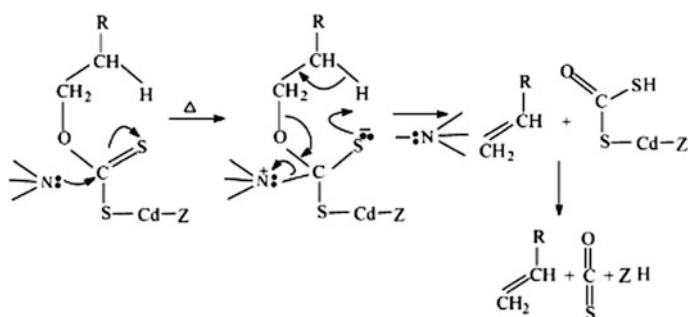


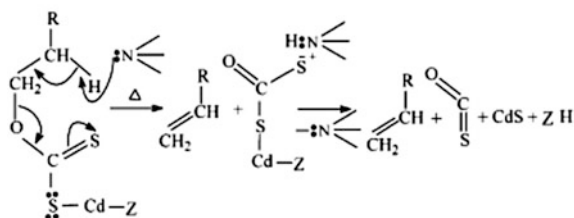
Fig. 8.6 TEM (a, b) and HRTEM (c) CdS nanoparticles images obtained by thermolysis of Cd (pip-dtc)₂ at temperatures 140 (a) and 180 °C (b, c) in HDA

of Lewis base performing a function of a thermal decomposition promoter and a stabilizing agent at a time, at moderate temperatures (120–150 °C) can be regarded as sufficient general method of nanoparticle synthesis for a wide range of metal chalcogenides (Cd, Zn, Pb, Hg, Cu, Ni, Mn, etc.), including nano-objects with the core-shell structure. It is expected that the thermal decomposition of cadmium dixantate can proceed through the concert mechanism of the shift of three electron pairs under the catalytic effect of the solvent. In this case, the solvent can activate O–C–S₂Cd group shifting the charge density from C–S bond to S–C bond according to scheme A (Fig. 8.7). In addition, the Lewis base as protonated intermediate may facilitate proton transfer required for the reaction (scheme B) and, finally, be a stabilizing ligand, reducing at least one of Cd–S bonds in dixantate, thereby promoting the CdS formation (scheme C).

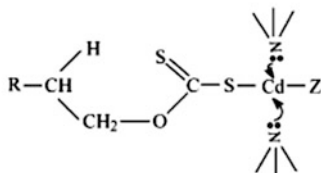
Experimental results [136] indicate that the ligand role in the reaction system is important not only for formed nanocrystals and starting precursor molecules.



(A) Nucleophilic attack on the (thio) carbonyl center



(B) Protonated intermediates



(C) Ligand stabilization of the metal center

Fig. 8.7 Possible ways of decomposition of metal chelate Cd(II) dixantate with a Lewis base $Z=R-O-C(=S)-S$

Rigidly-bound ligand with the monomer molecule determines primarily nucleation process, while strong ligands on the nanocrystal surface are crucial for the growth stage. Generally, it can be monitored the morphology and form of the obtained nanoparticles, as well as their phase composition. For ZnS thermodynamically stable sphalerite structure with a zig-zag conformation in the direction $\langle 111 \rangle$ and kinetically stable wurtzite structure with hindered conformation in the direction $\langle 002 \rangle$ is characteristic. The differences in the steric effect and coordinating capacity between HDA and TOP determine the diversity of their binding character. TOP is relatively strong ligand for the monomer precursor, i.e. it forms stable complexes. Therefore, nucleation proceeds slow and complexes have time to adapt advantageously, and steric hindrance between them and the ZnS lattice during growth is minimized. The staggered conformation is preferred in TOP, and the resulting ZnS has sphalerite structure [132, 137]. Due to the high symmetry of the structure spherical shape particles are formed predominantly, despite the monomer high concentration. Because the HDA is a weak ligand for the monomer and strong for zinc sulfide nanocrystals the nucleation occurs rapidly in alkylamine solution, and the resulting nanocrystals are associated with HDA molecules. Due to the absence of steric hindrances the clusters are connected to each other to form a wurtzite structure with the particle shape in the form of elongated rods.

It should be emphasized that SSP rational design, the appropriate choice of the ligands or substituents on metal atoms allows synthesis of nanostructured materials under milder conditions that successfully demonstrated for the nanocrystals based on many transition metals and their oxides, as well as main group elements [138–140].

8.2.1.3 Temperature Influence

It is known that the nanorod aspect ratio decreases with temperature increasing [141], i.e., at high nanoparticle synthesis temperatures, growth thermodynamic regime is preferred, which is reflected in the formation of isotropic particles (spherical or cubic), while at lower temperatures, a nonequilibrium kinetic regime promotes the formation of anisotropic particles [142]. CdS nanoparticles, obtained by $[\text{Cd}(\text{pip-dtc})_2\text{Py}]$ thermolysis at 190 °C had rod form with a length of 64.38 ± 4.62 nm and a width of 5.20 ± 0.98 nm with an aspect ratio of 12.38 (Fig. 8.8) [62]. At 230 °C nanorods had a size of 24.84 ± 4.42 nm in length and 6.58 ± 1.02 nm in width, whereas at 270 °C oval shape nanoparticles with a diameter of 16.8–23.3 nm along with rod shape nanoparticles are formed.

Nanoparticle synthesis temperature plays an important role in the structural-phase transformations. For example, for CdS nanoparticles it is demonstrated that the hexagonal phase is the predominant phase at high synthesis temperatures [143, 144]. During CdS nanoparticle preparation by thermolysis of $\text{Cd}(\text{pip-dtc})_2$ in castor oil at 190, 230, 270 and 300 °C hexagonal phase c reflexes (100), (002), (101), (110) (103) and (112) in the diffractograms was formed at all temperatures, while during the Cd $(\text{thq-dtc})_2$ thermolysis at 190 and 230 °C metastable cubic phase was observed, and thermodynamically stable hexagonal phase was observed at 270 and 300 °C [145].

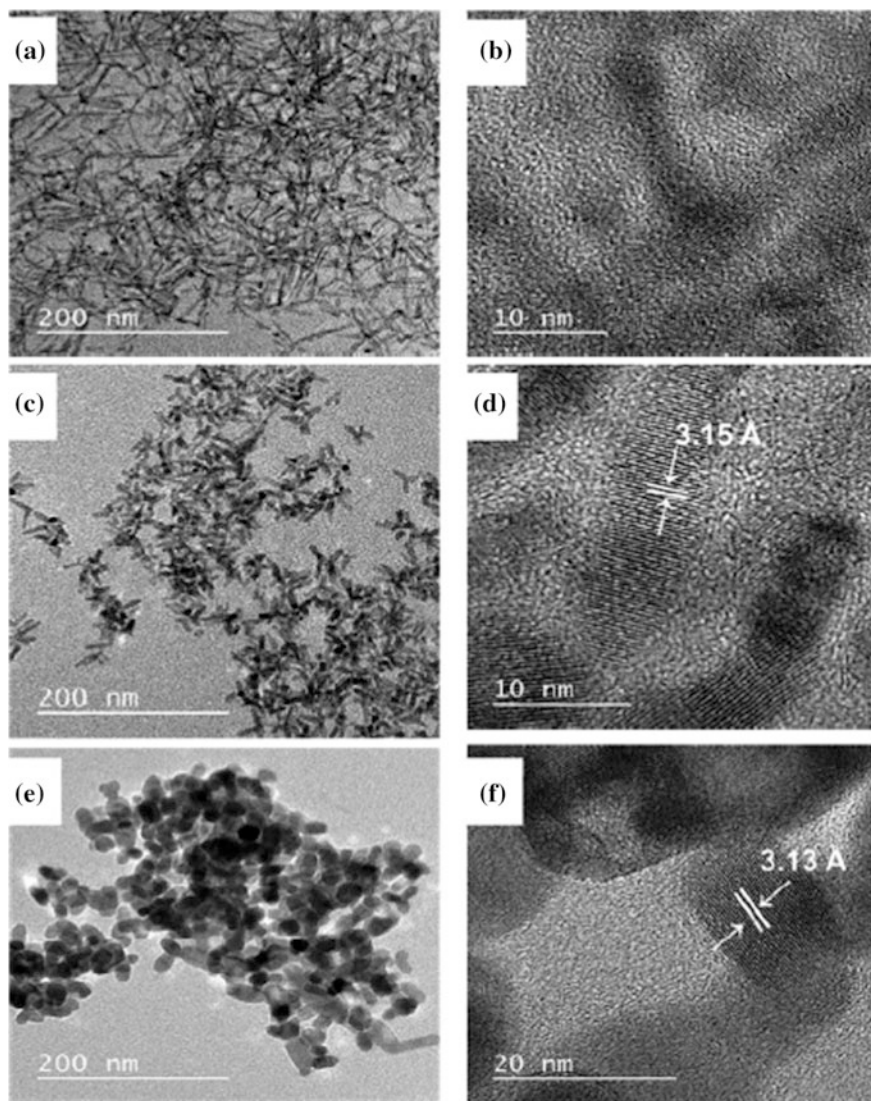


Fig. 8.8 Electron micrographs of CdS nanoparticles obtained by thermolysis of $[\text{Cd}(\text{pip-dtc})_2\text{Py}]$ at temperatures of 190 (a, b), 230 (c, d) and 270 °C (e, f)

In contrast, thermolysis of these complexes in the ricinoleic acid at all temperatures leads to the cubic phase formation. It should be noted that the occurrence of CdS metastable cubic phase also shows the demonstration of the quantum confinement effect, because the cubic phase is characterized only for CdS nanocrystal unlike the hexagonal form which occurs in both nanocrystalline and the bulk material [146]. The wide variation in morphology (Fig. 8.9) and the phase composition of thin films of iron sulfide from dithiocarbamate Fe(III) complexes is observed when the

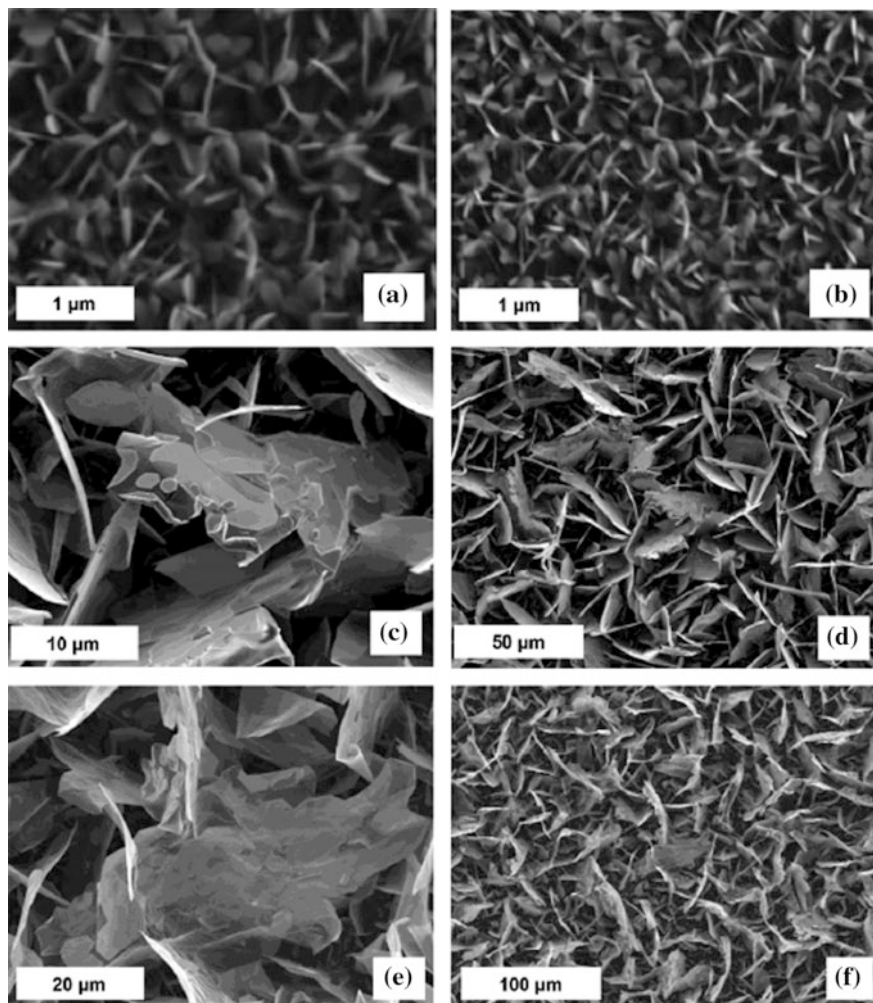


Fig. 8.9 SEM images of the iron sulfide thin films deposited at 350 °C (a, b), 400 °C (c, d) and 450 °C (e, f) using complex $\text{Fe}(\text{pip-dtc})_3$

conditions change during Aerosol Assisted Chemical vapor deposition (AACVD), e.g. temperature, the precursor nature, the solvent type (Table 8.1) [114].

Crystal packing defects, particle sizes, etc. can also act as determining factors [147]. For CdS hexagonal wurtzite structure is characterized by particles with a diameter >5 nm, while the nanoparticles with very small size (~ 3 nm) have a cubic sphalerite structure.

By varying the reaction conditions, it can be generally activated two mechanism of nanoparticle formation, i.e. with the dominance of the growth process and processes due to nucleation, when it can be temperature-dependent control of

Table 8.1 The morphology and phase composition of the iron sulfide thin films obtained at different reaction conditions

Precursor	Conditions	Morphology	Phase composition
Fe (pip-dtc) ₃	Toluene, 350–450 °C, 2 h	Leaf, flake, sheet	Hexagonal (Fe _{0.975} S), marcasite (FeS ₂)
	Chloroform, 350–450 °C, 30 min	Fiber	Hexagonal (Fe _{0.975} S), smythite (Fe ₃ S ₄)
	<i>tert</i> -Butyl thiol, 450 °C, 2 h	Flower, spherical-globular	Greigite (Fe ₃ S ₄)
Fe (thq-dtc) ₃	Toluene, 350–450 °C, 2 h	Leaf, flake, sheet	Pyrrhotite (Fe _{0.95} S _{1.05}), hexagonal (Fe _{0.975} S)
	Chloroform, 350–450 °C, 30 min	Fiber	Hexagonal (Fe _{0.975} S)
	<i>tert</i> -Butyl thiol, 450 °C, 2 h	Spherical and flake	Greigite (Fe ₃ S ₄)

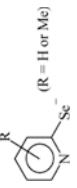
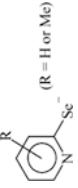
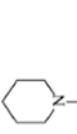
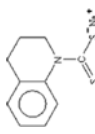
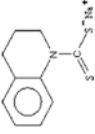
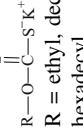
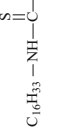
nanoparticle sizes. Such examples are numerous. CuS nanoparticles were obtained by Cu(II) butylaminodithiocarbamate thermolysis at two different temperatures in a typical TOP and HDA medium [148]. Nanoparticle dimensions were 3–7 nm and 21–38 nm at synthesis temperatures of 120 and 180 °C, respectively, and the product is also characterized by a narrow particle size distribution in the first case. The band gap exceeds that value for the bulk semiconductor and was 4.33 and 3.98 eV for the products obtained at 180 and 120 °C, respectively.

Thus, chalcogenide metal chelates are effective precursors for the preparation of the nanocomposites, stabilized against further aggregation by thermolysis products of complexes ligand shell (Table 8.2).

8.2.2 Controlled Thermolysis of Azomethine Transition Metal Chelates

To date, considerable experimental material on thermolysis of azomethine transition metal chelates has been prepared. Among the most typical examples we note the synthesis of cubic Co₃O₄ nanoparticles by thermolysis of chelate [Co^{II}{(μ-L)(μ-OAc)Co^{III}(NCS)}₂], where H₂L is salen type ligand 1,6-bis(2-hydroxyphenyl)-2,5-diazahexa-1,5-diene, as precursor [149]. It is important that thermolysis of the chelate at 600 °C in the presence of citric acid leads to the formation of Co₃O₄ nanoparticles with the average crystallite size of ~13 nm. In another example the thermolysis of praseodymium chelate ([PrL(NO₃)₂]NO₃, where L is N,N'-bis(2'-hydroxyacetophenonimine)-*o*-dipropylene triamine) was studied at different temperatures of 300–800 °C [150]. In this case, praseodymium oxide with small grain size, very uniform sphere-like shape and pure cubic phase is the main product of the thermolysis at 600 °C.

Table 8.2 Chalcogenide metal chelates as SSP of the nanostructured materials

SSP	Chelating ligand	Thermolysis conditions	Phase composition, nanoparticle shape and dimensions	References
[Sb{Se-C ₅ H ₃ (Me)N}] ₃ ·1.5H ₂ O		200 °C, HDA, CH ₂ Cl ₂ , hot injection; 400–450 °C, argon 375–500 °C (AACVD)	Sb ₂ Se ₃ , rods, width 40–60 nm, length 0.6–1.4 μm; thin film (Sb ₂ Se ₃ , nano-wires, 240–500 nm)	[65]
[Bi{Se-C ₅ H ₃ (Me)N}] ₃ ·0.5H ₂ O		235 °C, HDA, CH ₂ Cl ₂ , hot injection; 400–450 °C, argon 375–500 °C (AACVD)	Bi ₂ Se ₃ , flake, width 30 nm, length ~760 nm; thin film (Bi ₃ Se ₄ , boat/half hexagon—petals, sheets, hazy wool-like)	[65]
Cd(pip-dtc) ₂		350–450 °C (AACVD)	CdS, thin film, 57.37 nm (350 °C), 63.57 nm (400 °C), 72.97 nm (450 °C)	[61]
Cd(thq-dtc) ₂		350–450 °C (AACVD)	CdS, thin film, 160–220 nm, cubic to spherical	[61]
[Cd(thq-dtc) ₂ (phen)]		Diethylenetriamine, 199 °C, 2 min	CdS nanorods ca. 7 nm, length 50–75 nm	[57]
Metal alkyl xanthates M=Cd, Zn, Pb, Hg, Cu, Ni, Mn	 R = ethyl, decyl, hexadecyl	HDA, decylamine, trioctylamine, 120–140 °C	CdS, ZnS (4.5 nm), spherical, CdS rods (5 nm width, 20 nm length), CdS/ZnS, CuS, NiS, MnS (spherical, rods), PbS and HgS (r.t., decylamine)	[133]
Metal hexadecyldithiocarbamate M=Cd, Zn, Pb, Hg, Cu, Ni, Mn		HDA, 170–200 °C	CdS, ZnS (spherical), ZnS/CdS (70–170 °C)	[133]

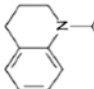
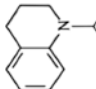
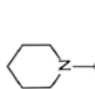
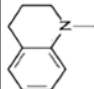
(continued)

Table 8.2 (continued)

SSP	Chelating ligand	Thermolysis conditions	Phase composition, nanoparticle shape and dimensions	References
Metal hexadecyltrithiocarbamate M=Cd, Zn, Pb, Hg, Cu, Ni, Mn		HDA, 180–200 °C	CdS (5 nm)	[133]
[Cd(pip-dtc)2Py]		HDA, TOP, 190 °C; thin films, chloroform, (AACVD, 350, 400, 450 °C)	CdS, rods, 64.38 ± 4.62 nm length, 5.20 ± 0.98 nm width (190 °C), 24.84 ± 4.42 nm length, 6.58 ± 1.02 nm breadth (230 °C), oval, 16.8–23.3 nm; CdS, thin film	[62]
Cd[S(L)]2, L = 2-(4,4- dimethyl-1,2-oxazolinyloxy) benzene]		TOP, TOPO, 280 °C	CdS, hexagonal phase, 200 nm	[129]
Cd[Se(L)]2, L = 2-(4,4- dimethyl-1,2-oxazolinyloxy) benzene]		TOP, TOPO, 280 °C	CdSe, hexagonal phase, 200 nm	[129]
Cd(pip-dtc)2		TOP, HDA, 180 °C	CdS, rods, bipods, tripods (19.11 ± 7.29 nm length, 3.64 ± 0.78 breadth)	[128]

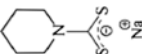
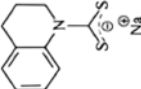
(continued)

Table 8.2 (continued)

SSP	Chelating ligand	Thermolysis conditions	Phase composition, nanoparticle shape and dimensions	References
Cd(thq-dtc) ₂		TOP, HDA, 180 °C	CdS, rods, bipods (21.61 ± 6.08 nm length, 4.55 ± 1.04 breadth)	[128]
Cd(pip-dtc) ₂		TOP/TOPO, 240 °C	CdS, spheres, 3.97 ± 0.69 nm, 4.33 ± 0.59 nm	[128]
Cd(thq-dtc) ₂		Castor oil, ricinoleic acid, 190–300 °C, N ₂ , 30 min–2 h	CdS (castor oil), spherical, short rods and oval, 15.53 ± 3.18 nm (230 °C), 15.6 ± 3.74 nm (270 °C), 17.96 ± 1.95 nm (300 °C); CdS (ricinoleic acid) 21.12 ± 3.57 nm (270 °C), 22.67 ± 3.58 nm (300 °C)	[139]
Cd(thq-dtc) ₂		Castor oil, ricinoleic acid, 190–300 °C, N ₂ , 30 min–2 h	CdS, oval rod, 13.36 ± 1.82 nm (270 °C), spherical 15.7 ± 1.73 nm (300 °C)	[139]
Cd(II) butyl amine dithiocarbamate	butyl amine dithiocarbamate sodium salt	TOP, HDA, 180–120 °C, 60 min, N ₂	CuS, spherical, 15.8 nm (180 °C), 6.61 nm (120 °C)	[150]

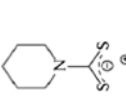
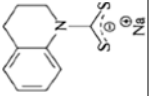
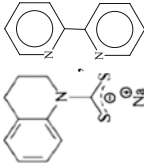
(continued)

Table 8.2 (continued)

SSP	Chelating ligand	Thermolysis conditions	Phase composition, nanoparticle shape and dimensions	References
Zn(Se ₂ CNEt ₂) ₂	diethyl/disenocarbamate diethyl ammonium salt	Pyrolysis GC-MS, 280 °C	Se _n , n ~ 1 ± 7, ZnSe	[123]
Cd(Se ₂ CNEt ₂) ₂	diethyl/disenocarbamate diethyl ammonium salt	Pyrolysis GC-MS, 280 °C	Se _n , n ~ 1 ± 7, CdSe	[123]
Zn(Se ₂ CNNMe ⁿ Hex) ₂ , bis [methyl(<i>n</i> -hexyl)-disenocarbamate]-zinc	methyl(<i>n</i> -hexyl)-disenocarbamate	Pyrolysis GC-MS, 280 °C	ZnSe	[123]
Cd(Se ₂ CNNMe ⁿ Hex) ₂	methyl(<i>n</i> -hexyl)-disenocarbamate	Pyrolysis GC-MS, 280 °C	CdSe	[123]
Fe(pip-dtc) ₃		Pyrolysis GC-MS, 280 °C AACVD, chloroform, toluene, 350–450 °C	Fe _{0.975} S, FeS ₂ (350, 400 °C), FeS, hexagonal-phase (450 °C); sheet-like (350 °C), nano-leaf/flake like (400, 450 °C)	[122]
Fe(thq-dtc) ₃		AACVD, chloroform, toluene, 350–450 °C	FeS, hexagonal (350, 400 °C), nanosheet-like; Fe _{0.95} S _{1.05} , hexagonal-pyrrhotite (450 °C)	[122]
[PdCl ₂ (PhS-CH ₂ CH ₂ CH ₂ -NH ₂)]	3-(phenylsulphanyl)propylamine	Oleylamine, oleic acid: octadecene (1:1), 195 °C	Pd ₄ S, nanoflowers, ~ 23–38 nm (oleylamine); nanospheres, 15–28 nm (oleic acid: octadecene)	[124]

(continued)

Table 8.2 (continued)

SSP	Chelating ligand	Thermolysis conditions	Phase composition, nanoparticle shape and dimensions	References
Zn(pip-dtc) ₂		HDA, TOP, TOPO, 180, 270 °C	ZnS, spherical to elongated), 4.74 ± 0.64 nm (180 °C), 6.43 ± 0.60 nm (270 °C)	[121]
Zn(thq-dtc) ₂		HDA, TOP, TOPO, 180, 270 °C	ZnS, spherical, 5.94 ± 0.25 nm (270 °C)	[121]
Zn(thq-dtc) ₂ (bpy)		Triethylenetetraamine, 299 °C, solvothermal method	ZnS nanosheets, 75–225 width, 90–375 nm length	[6]

Thermolysis of nickel salen chelate at temperature 700 K in the absence of any template or surfactant leads to uniform NiO particles [151].

Also, metal N,O-containing chelates can be used for obtaining doped nanoparticles. For example, the thermolysis of an unusual square pyramid Mn(III) chelate, $[\text{Mn}(\text{L})(\text{H}_2\text{L})]\text{PF}_6$, where L is (5,5'-dimethoxy-2,2'-(propane-1,2-diyl-bis(nitrilomethylidene))diphenolato), results in Mn-doped ZnO nanoparticles [152].

It should be noted the Ni(II) complexes $[\text{Ni}(\text{L})_2](\text{ClO}_4)_2$ and $[\text{Ni}(\text{L})_2(\text{NO}_3)_2]$, where L is the Schiff base 4,5,9,13,14-pentaaza-benzo[b]triphenylene, which were used for obtaining NiO nanoparticles by calcination at 500 °C [153]. Complexes of various Schiff bases and related ligands can also be precursors for nanoparticles of oxides of copper and other metals. Thus, a symmetric tetradentate Schiff base ligand, N,N'-bis(5-bromosalicylaldehyde)-1,3-phenylenediamine (L), and its Cu(II) and Co(II) chelates with general formula $\text{M}_2(\text{L})_2$, where M=Co or Cu, were used as precursors for corresponding metal oxide nanoparticles [154]. Preparation of single phases of CuO, CoO, and NiO nanoparticles using Cu(II), Co(II), and Ni(II) chelates $\{[\text{Cu}(\text{H}_2\text{L})(\text{H}_2\text{O})_2(\text{Cl})]\text{Cl}$, $[\text{Co}(\text{H}_2\text{L})(\text{H}_2\text{O})_3]\text{Cl}_2 \cdot 3\text{H}_2\text{O}$ and $[\text{Ni}(\text{H}_2\text{L})(\text{H}_2\text{O})_2]\text{Cl}_2 \cdot 6\text{H}_2\text{O}\}$, where H_2L is 2-[(5-*o*-chlorophenylazo-2-hydroxybenzylidene)amino]phenol Schiff base, as precursors by a solid-state thermolysis was carried out [155].

In recent years, special attentions is paid to the synthesis of new bi- and tridentate azomethine ligands with oxygen-, nitrogen-, sulfur-containing chelating fragments and their metal chelates [156–159]. The possibility of a wide variation of heteroligand environment in such chelates (Fig. 8.10), their high thermal and chemical stability, relatively simple synthetic schemes and the availability of the starting reagents allow considering such metal chelates as promising precursor for the preparation of metal-polymer nanocomposites in which the specific polymer (oligomer) shell is formed from ligand degradation products.

Thermolysis (370 and 600 °C) of metal chelates of this type in the condensed phase, apparently, is a multi-step process, the total scheme of which can be represented as follows (Scheme 8.4) [160].

The thermal behavior of azomethine metal chelates is defined as the metal nature, the composition and structure of framing functional ligands and the metal-ligand bond nature, and, in general, stability of the metal chelate.

8.2.2.1 Nickel(II) Chelates

Thermal characteristics of mononuclear nickel chelates **Ni1–Ni4** are shown in Table 8.3 [161]. Of interesting is thermal behavior of nickel chelate **Ni4**: up to 390 °C the weight increase is observed by 3.6%, due, apparently, to the oxidation process, then at 450 °C a dramatic weight drop proceeds up to 31%, than this process slows down, and at 800 °C the weight loss is 43%. The melting peak is recorded on the DSC at 365.2 °C. As can be seen from the obtained data, the thermal stability of nickel azomethine chelates depends on the ligand type. The melting point is maximum for **Ni4**, decomposition beginning temperature increases in the series of chelates **Ni3 < Ni2 < Ni1 < Ni4**, and weight loss at 800 °C is

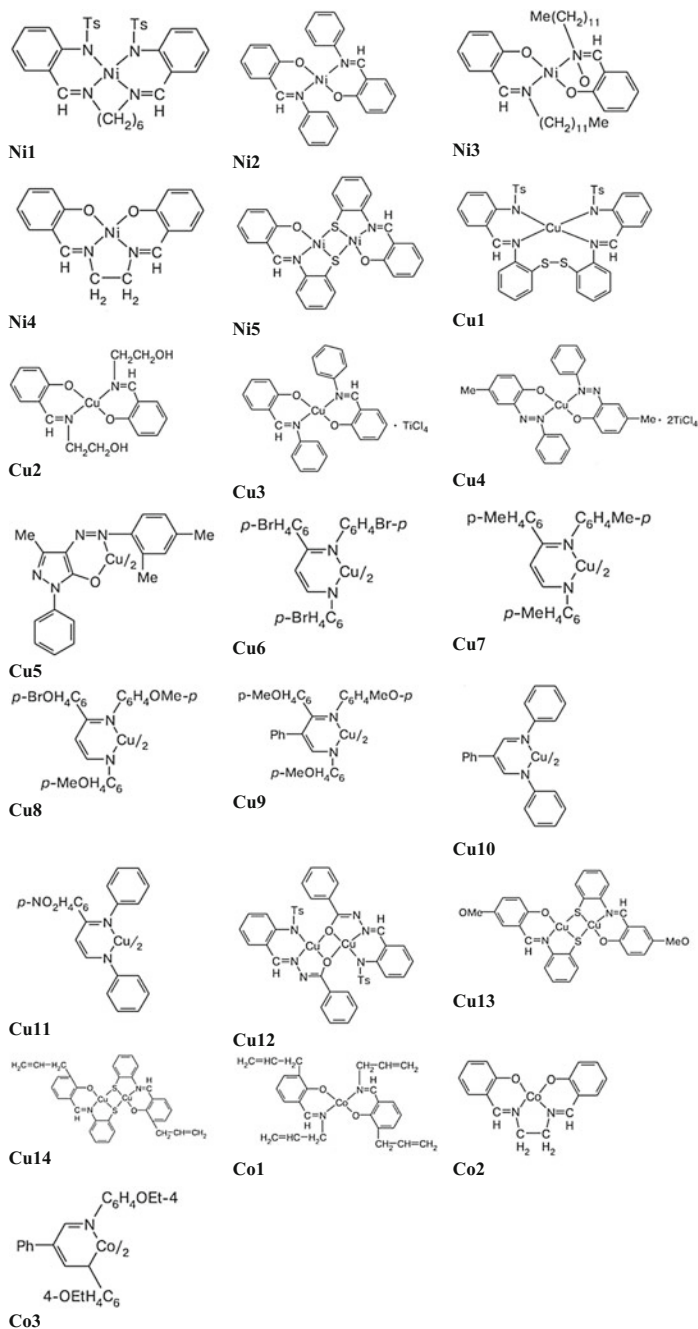
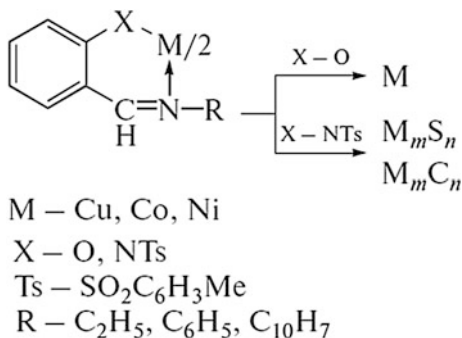


Fig. 8.10 Structures of azomethine metal chelates

Scheme 8.4 Thermolysis of azomethine metal chelates**Table 8.3** Thermal properties of azomethine chelates [157–159]

Chelate	Temperature (°C)				Weight loss in full decomposition (%)
	Melting	Decomposition onset	Decomposition at 50%	Decomposition end	
Ni1	— ^a	350	390	750	70.8
Ni2	— ^a	225	435	740	62.5
Ni3	92.8	320	390	550	79.9
Ni4	365.2	380	—	780	35.7
Cu1	225	270	—	760	40.4
Cu2	177	190	292	700	67.8
Cu3	110	325	—	680	45.8
Cu4	140	100	—	700	47.4
Cu5	245	260	422	660	60.2
Cu6	—	285	720	780	53.3
Cu7	—	265	780	790	50.1
Cu8	—	200	—	730	46.0
Cu9	286	200	402	620	68.9
Cu10	318.3	330	375	730	84.6
Cu11	—	210	—	740	37.0
Co1	138.1	323	—	560	48.8
Co2	351.9	355	—	730	35.2
Co3	191	220	—	700	42.7

^aPrior to the decomposition onset the melting is not observed

minimum for **Ni4** chelate. In other words, metal chelates of tetradentate azomethine ligands **Ni1** and **Ni4** are significantly more stable than metal chelates based on bidentate azomethine ligands, and introduction of allyl fragments in aldehyde and amine moieties leads to significant reduction in the melting point.

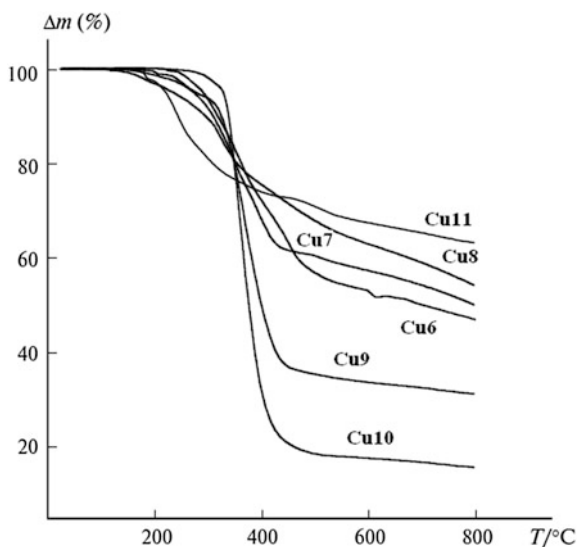
8.2.2.2 Copper(II) Chelates

As in the case of nickel chelates, the chelate **Cu1** based on tetradentate azomethine ligand has a higher melting point. Introduction of alcohol fragments in the amine moiety in **Cu2** chelate lowers the melting point, as well as introduction of alkyl substituents. The chelates **Cu3** and **Cu4** are less stable and already begin to melt at 110 and 140 °C, respectively (see Table 8.3). In the case of chelates **Cu6–Cu9** and **Cu11** introduction of Me- and OMe-groups in the phenyl ring lowers the melting point from 222 to 191 °C. For chelates **Cu9** and **Cu10** introduction of alkoxy (OMe) groups in the benzene rings of the amine fragments also causes a decrease in melting point compared with unsubstituted analogues. Except chelates **Cu9** and **Cu10**, copper complexes are more thermostable than nickel complexes: for them weight loss at 500 °C as determined by thermal analysis is not more than 50 wt% (Fig. 8.11) [158, 162].

8.2.2.3 Cobalt(II) Chelates

Cobalt chelate **Co1** is stable substance up to 200 °C, the weight loss occurs in two steps: up to 310 °C (21.8%), then the process slows down and the total weight loss as a result of thermolysis up to 800 °C is 48.8%. Melting peak according to DSC data corresponds to 138.1 °C with heat absorption of 50.67 J g⁻¹, and at 323.2 °C the exothermal process with heat of 258 J g⁻¹ is observed. Above 550 °C the chelate decomposes. Of the analyzed cobalt chelates **Co2** is most stable: its melting point is 351.9 °C, and the weight loss during thermolysis up to 800 °C is only 35.2% (see Table 8.3). As in the case of nickel chelates, the introduction of the allyl

Fig. 8.11 TGA data for azomethine copper(II) chelates



substituents compared with the aryl substituents lowers the melting point. Chelate **Co2** based on salen tetradentate ligand has a significantly higher melting point ($>300\text{ }^{\circ}\text{C}$) as compared with chelates of bidentate ligands.

8.2.2.4 Composition and Structure of Thermolysis Products of Azomethine Metal Chelates

Solid phase products of the thermolysis are matrix-stabilized metal nanoparticles which are homogeneously distributed in size and in the space of a matrix. We note that the chelating ligand nature and consequently formed stabilizing matrix on their basis has a significant influence on the sizes of obtained nanoparticles and the character of their size distribution, as exemplified by the thermolysis products of binuclear copper(II) chelates **Cu12** and **Cu13** (Fig. 8.12) [158]. The size of cobalt nanoparticles in the thermolysis product of **Co2** ($T = 600\text{ }^{\circ}\text{C}$), estimated by the Scherrer equation was $\sim 15\text{ nm}$.

For different metal chelates the formation of self-organized nanocomposites based on crystalline cobalt sulfide clusters Co_9S_8 (thermolysis at 593 K) and Co_6S_5 (thermolysis at 873 K), Ni_3S_2 and NiC , nanocrystalline copper with structure core-shell, where a nanocrystalline core of $2\text{--}3\text{ nm}$ particles collected in aggregates of $10\text{--}20\text{ nm}$ and even larger, and shell is formed from the ligand degradation products [157].

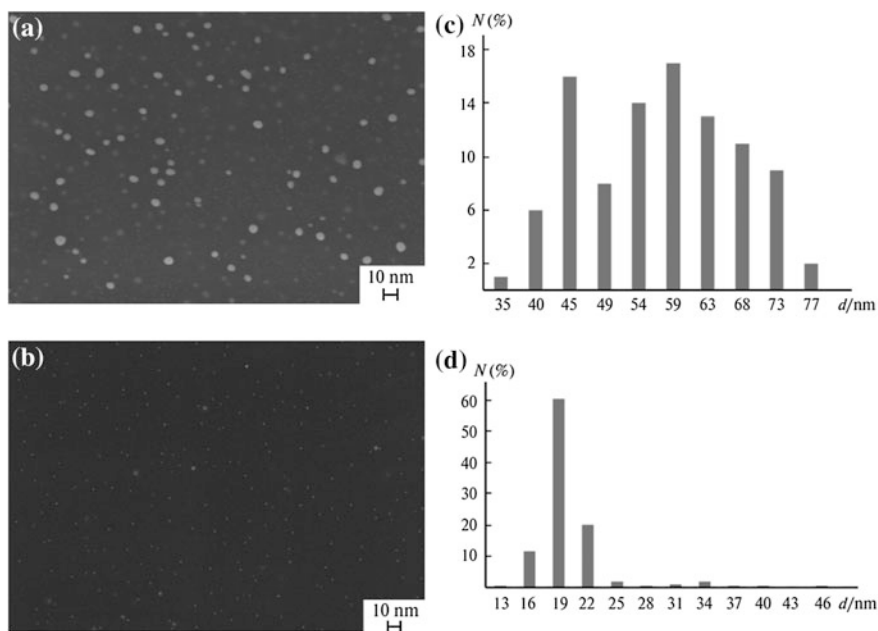
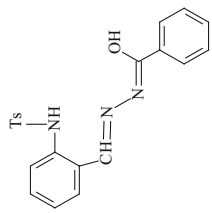
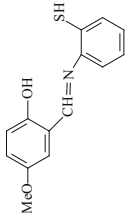
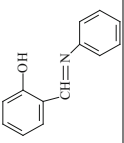
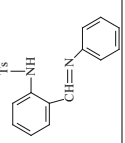


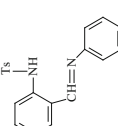
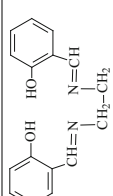
Fig. 8.12 SEM images (a, b) and histograms showing the size distribution of nanoparticles (c, d) for the thermolysis products ($600\text{ }^{\circ}\text{C}$) of Cu chelates Cu12 (a, c) and Cu13 (b, d)

Table 8.4 Azomethine metal chelates as SSP of the nanostructured materials

SSP	Chelating ligand	Thermolysis conditions	Phase composition, nanoparticle shape and sizes	References
Bis[(2-N-tosylaminobenzylidene)benzoylhydrazonato]dicopper(II)		Solid phase thermolysis, SGA, 600 °C	Cu, 40–70 nm	[160]
Bis[(2-hydroxy-5-methoxybenzylidene)-2'-mercaptophenyliminato] dicopper(II)		Solid phase thermolysis, SGA, 600 °C	Cu, 20 nm	[160]
Bis[(2-hydroxybenzylidene)phenyliminato]copper(II)		Solid phase thermolysis, SGA, 600 °C	Cu	[159]
Bis[(2-N-tosylaminobenzylidene)phenyliminato]cobalt(II)		Solid phase thermolysis, SGA, 320, 600 °C	Co ₉ S ₈ (320 °C); Co ₆ S ₅ (600 °C)	[159]

(continued)

Table 8.4 (continued)

SSP	Chelating ligand	Thermolysis conditions	Phase composition, nanoparticle shape and sizes	References
Bis[(2-N-tosylaminobenzylidene)phenyliminato]nickel(II)		Solid phase thermolysis, SGA, 600 °C	Ni ₃ S ₂ , NiC	[159]
N,N'-Bis[(2-hydroxybenzylidene)-1,2-diaminoethane]cobalt(II)		Solid phase thermolysis, SGA, 600 °C	Co, ~15 nm	[160]

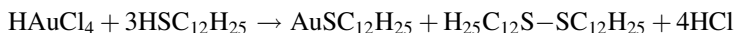
Thus, transition metal chelates based on Schiff bases are effective precursors for self-assembled nanocomposites stabilized against further aggregation by thermolysis products of chelate ligand shell. Thermolysis optimization of these chelates (Table 8.4), the possibility of the formation of alloys based on complexes with various metals, along with the identification of the thermolysis mechanism and detailed characteristic of the properties of emerging products will promote further research into the development of advanced nanocomposite materials.

8.2.3 Metal Chelate Thermolysis in Polymer Matrix

The incorporation of metal-containing precursors into a polymer matrix is a broad area of current research [8]. In this case there are two possibilities. The *ex situ* (in a second moment) process involves adding and mixing micro- or nanoparticles of the inorganic precursor to the finished polymer. At the same time, in the *in situ* method the initial nanoparticles are generated directly in the polymer matrix using, for example, polymeric metal chelates and their subsequent decomposition.

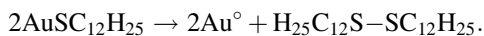
We emphasize the important fact connected with the processes of the thermolysis of the precursors with relatively bulky organic ligands. For example, under inert atmosphere, ruthenium-carbon composites with a ruthenium content of 20–32% (wt.) are formed from the ruthenium chelates $[\text{RuL}_3]\text{X}_2$, where L is bpy, phen; X is OH^- , Cl^- [163]. This is a result of a multi-stage destruction process of the organic ligand. At a temperature of 873 K intensive complex decomposition is completed with evolution of its fragments (pyridine and dipyriddy molecular ions). Further there is the destruction of the resulting condensed material to evolve light hydrocarbon fragments. The Ru-containing composites obtained at 873–973 K have high specific surface area of 424–477 $\text{m}^2 \text{g}^{-1}$, and ruthenium clusters are practically amorphous to X-rays. Superfine ($d \sim 1.5\text{--}2.0 \text{ nm}$) and relatively uniform size ruthenium particles in the Ru/C composite are in the form of planar Ru_6 hexagon associates. During thermolysis enveloping layers of turbostratic graphite-like carbon are formed by carbonization of organic ligand. In parallel-oriented turbostratic carbon layers with an interplanar distance of $\sim 0.34 \text{ nm}$ are tightly pressed to ruthenium particles, preventing them from sintering under the drastic pyrolysis conditions (973 K). Thus, the structure of the resulting composite can be represented as a set of spheres (coils), the center of which is a ruthenium nanoparticle («core»), and the outer shell is lined with layers of turbostratic carbon («shell»).

Gold(I) dodecylthiolate as a precursor for the formation of nano-sized particles in a PS matrix was prepared according to the scheme [164, 165]:



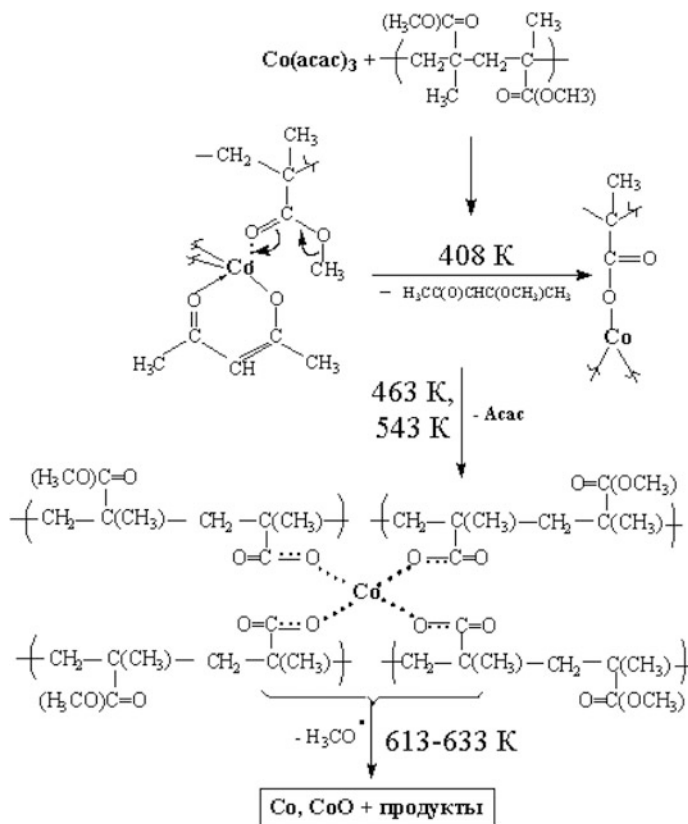
A thin (0.1–0.3 nm) transparent film was obtained by the addition of the precursor (5–10%) to the PS matrix (M_w is 230,000) with intensive sonication and solvation in acetone, and followed casting on a glass surface [165]. This film placed

between sheets of aluminum foil was subjected to short-term (40–105 s) thermolysis at 573 K. Gold nano-sized particles were formed according to the possible scheme:



However it is not ruled out the emergence of polynuclear complexes of the type $-(\text{Au}^{\text{I}}\text{SR}-)_n-$ with their further transformation to nanocrystals. As a result, polydisperse gold nanoparticles with a size of 1.8 nm (about 150 gold atoms), homogeneously distributed in the PS matrix were formed. Decomposition of Sb $(\text{SC}_{12}\text{H}_{25})_3$ in PS at 623 K results in the formation of Sb and Sb_2S_3 nanoclusters (15–30 nm) homogeneously distributed in the amorphous polymeric phase [166]. Thermolysis of metal dithiolates to form sulfide semiconductors in thin films was successfully carried out [167] under the action of laser radiation (or electron beam): the laser beam is defocused in a small beam diameter of 4 mm, which is concentrated a 2 kW power, and pulsing of 10–50 ms. Temperature in thin beam theoretically calculated from the parameters of the polymer and beam, and can be monitored. Thermolysis of thin films of the $\text{Pd}(\text{SC}_{12}\text{H}_{25})/\text{PS}$ is performed for 5 min at 443 K [168], but in air the formation of metal oxides in the polymeric matrix can occur (to prevent this process TOPO is used as the stabilizing antioxidant, for example, for CdS, ZnS, CdSe with size 2–4 nm, introduced ex situ [169]). Indeed, the thermolysis of the iron(II) mercaptide system $\text{Fe}(\text{SC}_{12}\text{H}_{25})_2/\text{PS}$ at 473 K for 2 min is accompanied by the formation of completely transparent light-brown film (almost complete light transmittance above 550 nm), in which nanoparticles with an average size of 10×50 nm are uniformly distributed [170]. Thermolysis of Pb (II) dithiocarbamate or xanthate in a PS matrix ($M_w \sim 280,000$) was carried out as a model system of the process of forming the polymer-nanoparticle hybrid layers in photovoltaic devices [171]. Chalcogenide complexes are most appropriate precursors for the preparation of such materials in situ. As noted earlier, they are quite stable compounds, do not decompose under the ordinary temperature conditions, stable in air and to moisture. As a rule, they are soluble in many organic solvents, and can thermally decompose at relatively low temperatures, i.e., thereby preventing undesirable degradation of the polymer matrix. By sufficiently technologically simple scheme consisting of spin coating of the polymer solution and the chelate precursor ($\text{Pb}(\text{S}_2\text{COBu})_2$, $\text{Pb}(\text{S}_2\text{COHex})_2$, $\text{Pb}(\text{S}_2\text{COOct})_2$, $\text{Pb}(\text{S}_2\text{CNBu}_2)_2$, $\text{Pb}(\text{S}_2\text{CNBu}_2)_2(\text{phen})$) on a substrate followed by heating the polymer film PbS nanoparticles in PS matrix were obtained. By varying the synthesis conditions, it is possible to obtain nanoparticles with different morphologies including PbS nanowires, which is of particular interest for photovoltaic applications. Similarly, by thermolysis in situ CdS nanoparticles in PVA matrix were synthesized using metal thiolate [172] or thiourea in aqueous Cd(II) solution [173] as a precursor.

The systems of $\text{M}(\text{acac})_n$ —polymer matrix are widespread. In this case, $\text{M}(\text{acac})_n$ thermolyzes to form nanoparticles and interacts with the matrix, initiating its destruction and depolymerization. In this regard, the thermal decomposition of $\text{Co}(\text{acac})_3$ —PMMA system is indicative (Scheme 8.5) [174, 175].



Scheme 8.5 Mechanism of the thermal destruction in the system of PMMA-Co(acac)₃

Table 8.5 Thermal stability of PMMA and its complexes with Mn(acac)₃ [175]

Polymer	The number of monomer units per Mn(acac) ₃ molecule	T _d , K	T _{max} , K
High-molecular-weight PMMA	See ^a	483	623
	50	403	638
	10	398	673
Low-molecular-weight PMMA	See ^a	493	633
	50	403	638
	10	403	673

^aNeat polymer

Thermolysis of Mn(acac)₃ in PMMA proceeds in a similar manner and the major process proceeds at higher temperatures than for pure PMMA (Table 8.5).

It should be noted that the thermolysis of $\text{Rh}(\text{acac})_3$ in the presence of polyols as reducing agents leads to the formation of rhodium nano-sized crystals with various shapes (for example, multipods, cubes, horns, cuboctedra) [176]. More promising approach to the production of such nano-sized particles (size 5 ± 15 nm) consists of one-stage reduction of the rhodium chelate $\text{Rh}(\text{acac})_3$ in the presence of butane-1,4-diol and PVp ($M_w = 55,000$) at temperatures of 240 ± 300 K [177]. This process results in triangular, pentagonal and hexagonal particles, capable to form Langmuir-Blodgett films on the silicon surface.

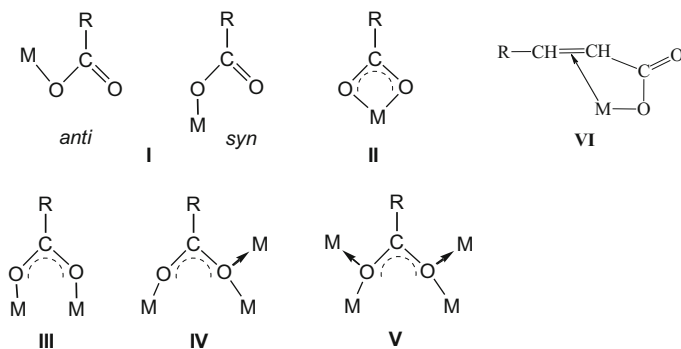
It is important that thermolysis of analyzed systems is multi-step process and is usually developing in two main mutually influencing directions: immediate decomposition of the precursor and inhibition of various transformations of a polymer chain (depolymerization, migration of double bonds, cross-linking, degradation, etc.). At the same time, formed nanoclusters may have a catalytic effect on carbonization and graphitization processes of polymers, in particular, the deep stages of decomposition of organic polymers, mechanisms which in most cases is not fully clear. It promotes the study of such interactions. Obvious is only trend: an increase of nanoparticle dispersion during thermal transformations contributes to an increase in the polar group content in the polymer [10].

8.3 The Conjugate Thermolysis—Nanoparticle and Polymer Matrix Formation Process

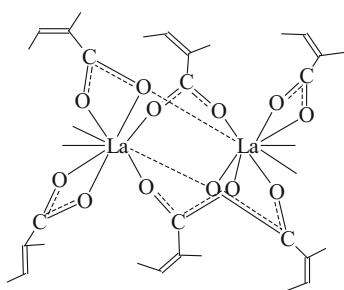
At present, different approaches for stabilizing nano-sized particle are developed [178]. Among them, the method of self-regulated stabilization based on simultaneous polymerization and thermolysis of metal-containing precursors or monomers is more promising.

Thermolysis of metal chelate monomers is poorly studied but intensively rapidly developing field of research, which may be the best embodiment of the idea of nanoparticle stabilization in situ. We consider this process an example of such interesting class of metal chelate monomers as metal carboxylates of unsaturated mono- and dicarboxylic acids [8, 11, 14, 15, 18, 179, 180]. Such compounds include acrylates (MAcr_n), methacrylates, maleates (MMal_n), itaconates, fumarates of alkali, alkaline earth, transition metals, their polysalts [13, 15]. This number can be added by acetylenecarboxylic acid salts [181–183].

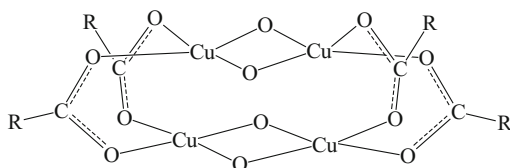
Metal carboxylates are a large group of metal complexes containing a carboxylate functional group with a different type of coordination with a metal atom, including by chelation type [11, 12]. In the most typical cases RCOO^- carboxylate group can be coordinated with the metal as a monodentate (I) anti- and syn-configuration, bidentate cyclic (chelating) (II), bidentate bridging (III), tridentate (IV), and the tetradentate ligand (V). Such a large variety of possible compositions and structures of metal carboxylates in the case of unsaturated analogs may be supplemented by the structural function of the multiple bonds, which, as known, is able to participate in coordination with a metal atom to form π -bond (VI):



In addition, chelating donor ligands such as, phen, bpy, mono-, di-, and tri-ethanolamine, and others are often contained in the composition of metal carboxylate complex. The formation of four-membered cycles during chelate addition of carboxyl group requires large strain in the valence angles of the metal atom. In the compounds of rare-earth elements such strain does not arise and the possibility of bidentate cyclic coordination increases. Probably, it is promoted by increasing the polarity of the metal-ligand bond, and high coordination numbers of the metal. For example, in the heteronuclear Cu_2La_2 - [184, 185] or CoCe - [186] methacrylate complexes the chelate groups are also on lanthanide center along with bridging groups. Moreover, in the carboxylates of this type the tridentate coordination of methacrylate groups is not uncommon, where one of the O atoms of the carboxyl group forms the bonds simultaneously with two metal atoms. In the isomorphous binuclear complexes of *trans*-2,3-dimethacrylates La or Gd $[\text{M}(\text{OOC}(\text{CH}_3)\text{C}(\text{CH}_3)\text{CH})_3(\text{phen})]_2$ metal atoms are connected by two bridging bidentate and two tridentate carboxylate groups [187]:



The character of the magnetic behavior of the complexes of $\text{Cu}(\text{II})$ (meth)acrylates, $[\text{Cu}(\text{CH}_2\text{CHCOO})_2\text{Cu}(\text{OH})_2]$ [188], and $[\text{Cu}(\text{CH}_2\text{C}(\text{CH}_3)\text{COO})_2\text{Cu}(\text{OH})_2]$ [189] is associated with their possible tetrameric structure:



Although synthesis of fine metal and (or) their oxides by thermal decomposition of organic acid salts in the solid phase, in particular, of formates, acetates, oxalates are widely used in practice [13], problems related to the ratio of the kinetic parameters of the solid phase transformation of this type of compounds and the dispersion level of their products, i.e. border of control capabilities of their dispersion, to date are relevant. Studies of thermal decomposition of some metal acrylates in thermal analysis regime in air and in an inert atmosphere [190, 191] give only a qualitative pattern of the transformations taking place during their thermolysis.

8.3.1 Thermolysis Kinetics of Metal Carboxylates

The most complete information on the effect of different factors on the kinetics, and the dispersion of the resulting products can be obtained under isothermal studies of thermolysis of the metal carboxylates in SGA. The thermolysis mechanism of metal carboxylates based on saturated carboxylic acids was most fully studied in a series of works [192–194]. In particular, thermal transformations of Fe(II), Fe(III), Ni(II), Cu(II), Pb(II) formates $M(\text{HCOO})_n$ and the oxalate $\text{Fe}_2(\text{C}_2\text{O}_4)_3 \cdot 5\text{H}_2\text{O}$ are temperature-separated sequential processes, involving dehydration with subsequent decomposition of the anhydrous carboxylate. Thermolysis proceeds successively in two macrostages to form metal carboxylates with a low metal oxidation state as intermediates bound, apparently with sufficiently low redox potentials of the $E^0[\text{Fe(III)/Fe(II)}] = +0.771 \text{ V}$ and $E^0[\text{Cu(II)/Cu(I)}] = +0.158 \text{ V}$ pairs. Thermolysis of Co(II) formate can be also conditionally divided into two stages: dehydration and a subsequent thermolysis. The first stage is studied in sufficient detail [195]. Thermolysis of the anhydrous product is accompanied by evolution of gaseous products H_2 , CO and CO_2 ; water vapor, evaporating also during dehydration stage, as well as CH_3OH , CH_3COOH , formic acid thermolysis products [196–198]. The topography of the thermolysis of anhydrous metal formates is characterized by the following features: both the crystals of the starting compounds and solid-state thermolysis products have a block structure with preservation of their habitus. The blocks are of sufficient porous and are «fastened» to a crystal by the polymer substance which is expected to be $-\text{[CH(R)-O]}_r-\text{[CH(COOH)-O]}_s-$, where $r \ll s$. It is expected that the polymer formation under the SGA conditions is

associated with catalytic thickening (polymerization) of the gaseous decomposition products CO_2 , H_2 , CO , H_2O , HCOOH under the action of formed catalytically active transition metal clusters.

It should be noted widespread thermolysis of oleate complexes dissolved in 1-octadecene [199–202]. Superparamagnetic iron oxide particles were prepared by thermolysis of iron acetylacetonate (at 538 K) in the presence of phenyl ether, oleylamine and 1,2-hexadecandiol [203] or anhydrous iron oleate (at 573 K) [201, 204].

1D Eu_2O_3 nanorods of 10–20 nm-thick with a 50–100 nm width, and a length ranging from hundreds nanometers to several micrometers are prepared by thermolysis of the complex $\text{Eu}(\text{L})\cdot 6\text{H}_2\text{O}$ obtained from an aqueous solution of europium nitrate and 1,3,5-benzenetricarboxylic acid (H_3L) [205–207]. Interestingly, during thermolysis below 873 K (two main stages of weight loss in TGA curves which are corresponded to elimination of water molecules at 383 K and elimination of the organic ligand at 742 K) 1D crystal thread of formed nanomaterial Eu_2O_3 is retained. Generally speaking, Eu_2O_3 was produced as nanoparticles of different shape: rods [208], nanowires [209], hollow spheres [210], and nanotubes [211]. Attention to such structures is due to their properties in the achievement of many physical and chemical parameters [212].

Thermal transformations were studied for a number of unsaturated metal carboxylates, in particular, d-element acrylates of copper(II) CuAcr_2 [213], cobalt(II) CoAcr_2 [214], nickel(II) NiAcr_2 [215, 216], polynuclear oxoacrylate Fe(III) FeAcr_3 [217], cocrystallizates FeAcr_3 and CoAcr_2 , FeAcr_3 and NiAcr_2 with atomic ratio of Fe:Co equal to 1:0.8 (FeCoAcr) and 2:1 (Fe_2CoAcr) [218], Fe:Ni = 2:1 (Fe_2NiAcr), Hf(IV) (meth)acrylate and fumarate derivatives [219, 220], maleates Co(II) (CoMal , $\text{Co}[\text{OOCCH}=\text{CHCOO}]\cdot 2\text{H}_2\text{O}$) [221] and Fe(III) (FeMal , $\text{Fe}_3\text{O}(\text{OH})[\text{OOCCH}=\text{CHCOOH}]_6\cdot 3\text{H}_2\text{O}$) [222], and for acrylamide complex of Co(II) nitrate (CoAAm) [223]. Thermolysis of the studied compounds is accompanied by gassing and weight loss of samples due to dehydration and subsequent thermal conversion of the dehydrated compounds. These processes occur sequentially in different temperature ranges.

8.3.2 Key Temperature-Separation Stages of Thermal Transformations of Metal Carboxylates

In general, the thermolysis study of metal carboxylates based on unsaturated acids in either the thermal analysis (TA), and SGA regimes revealed the general pattern of the nature of their transformation, consisting in a sequence of three main differing in temperature macrostages [14, 179, 180]: dehydration (desolvation) of the initial metal-containing monomer(s) (403–473 K); solid-state homo- or copolymerization of dehydrated metal-containing monomer(s) (473–573 K); decarboxylation of the resulting metallopolymer to a metal-containing phase and oxygen-free

polymer matrix at temperatures >523 K (in the case of copper carboxylates above 453 K), accompanied by intensive gassing.

8.3.2.1 Dehydration

At low thermolysis temperatures T_{therm} ($T_{\text{therm}} < 473$ K) dehydration of monomeric crystallohydrates occurs. According DTA-, TG-, DTG-research acrylates dehydration occurs at $T_{\text{therm}} = 353\text{--}487$ K (FeAcr_3), $413\text{--}453$ K (CoAcr_2), $373\text{--}473$ K (NiAcr_2), maleates at $393\text{--}433$ K (CoMal) and $373\text{--}433$ K (FeMal), for Co(II) acrylamide complex at $328\text{--}362$ K (Fig. 8.13).

A detailed study of the CoAcr_2 dehydration conditions under isothermal conditions at $T_{\text{therm}} = 303\text{--}433$ K indicates that it is reversible process. This is according to the IR spectroscopic studies. As a result of dehydration absorption bands associated with the modes of crystallization water $\nu(\text{O-H})$ $3000\text{--}3600$ cm^{-1} , $\rho_{\omega}(\text{O-H}) + \nu(\text{Co-OH}_2)$ 880 cm^{-1} disappear. Intensity of modes due $\delta(\text{O-H}) + \nu(\text{C=C})$ 1655 cm^{-1} , $\rho_{\omega}(\text{CH}_2) + \delta(\text{Co-OH}_2)$ 690 cm^{-1} , $\delta(\text{CH}_2) + \delta(\text{Co-OH}_2)$ 595 cm^{-1} simultaneously decreases. In some cases, there are two areas of evaporation. For example, during the CoAcr_2 dehydration in a completely isothermal conditions evaporation at $303\text{--}348$ K is limited by the evaporation of dehydrated water, $P_{\text{H}_2\text{O}}(T_{\text{therm}}) = 1.7 \times 10^7 \exp[-9200/RT]$ kPa, and the evaporation heat

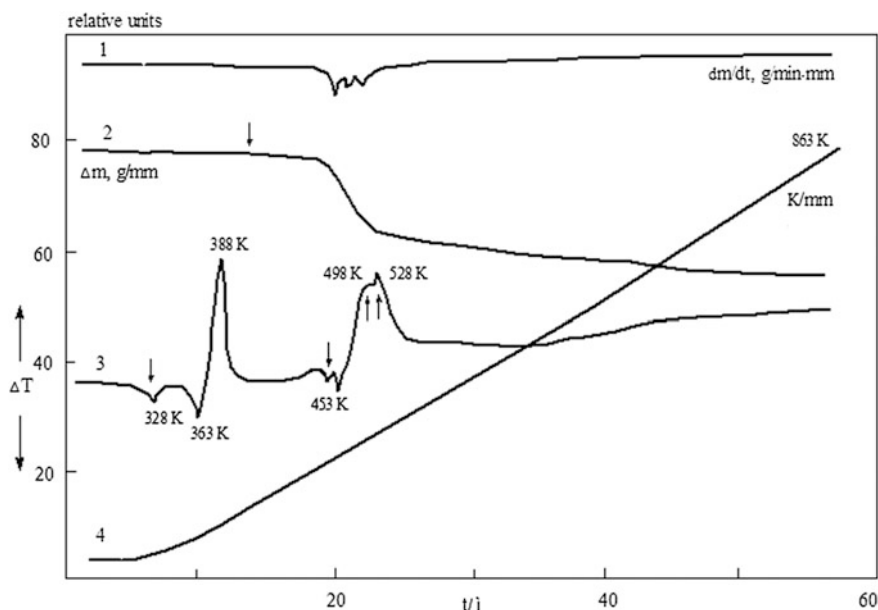


Fig. 8.13 Derivatograms of acrylamide complex Co(II) nitrate: 1—DTGA ($\text{dm/dt} \times 0.8$ $\text{g min}^{-1} \text{mm}^{-1}$), 2—TGA ($\Delta m \times 2.5 \times 10^3$ g mm^{-1}), 3—DTA ($\Delta T \times 0.88$ $\text{K min}^{-1} \text{mm}^{-1}$), 4—TA ($T \times 0.5$ K mm^{-1}) (heating rate 10 $^{\circ}\text{C min}^{-1}$, sample weight is 45.8×10^{-3} g)

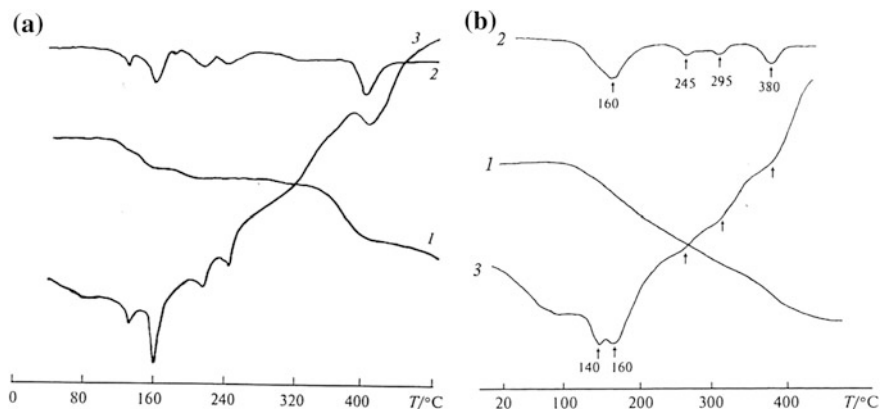


Fig. 8.14 Thermoanalytical curves of the thermolysis of maleinates Co(II) (a) and Fe(III) (b): 1—TGA, 2—DTGA, 3—DTA

$\Delta H_{\text{st}}(\text{H}_2\text{O}) = 38.5 \text{ kJ mol}^{-1}$ is close to the H_2O evaporation heat, $\Delta H_{\text{evap}}(\text{H}_2\text{O}) = 43.9 \text{ kJ mol}^{-1}$ [224]. Evaporation at $T_{\text{therm}} > 348 \text{ K}$ is described by dependent $P_{\text{H}_2\text{O}}(T_{\text{therm}}) = 2.7 \times 10^4 \exp[-4800/RT]$ kPa and is limited directly by dehydration, $\Delta H_{\text{evap}}(\text{H}_2\text{O}) = 20.1 \text{ kJ mol}^{-1}$. A similar dehydration process is observed in the case of thermolysis of Co(II) maleate (Fig. 8.14).

Endoeffects at 400 and 433 K are associated with two-step process of CoMal dehydration and are accompanied by weight loss, equals to 15.2 wt% (calc. 17.23%).

During dehydration in a vacuum the crystals of cobalt and zinc acetylenedicarboxylates ($\text{CoADC} \cdot 2\text{H}_2\text{O}$ and $\text{ZnADC} \cdot 2\text{H}_2\text{O}$) [180] are stable only up to a certain minimum content of the coordinated water, at which there is a sharp release of gaseous products of decomposition and formation of reactive moieties capable of initiating the solid phase metal monomer polymerization. With the help of quantum-chemical calculations (DFT) the dehydration energy of crystallohydrates $\text{CoADC} \cdot 2\text{H}_2\text{O}$ and $\text{ZnADC} \cdot 2\text{H}_2\text{O}$ is evaluated which is 150–200 kJ mol^{-1} [13]. Such a large quantity can lead to the mechanochemical activation of the decomposition of crystal and coordination structures $\text{CoADC} \cdot 2\text{H}_2\text{O}$ and $\text{ZnADC} \cdot 2\text{H}_2\text{O}$ during their dehydration.

8.3.2.2 Polymerization

The temperature increasing of the dehydrated monomer to $T_{\text{therm}} = 473\text{--}573 \text{ K}$ leads to a solid state polymerization. The transformation of the investigated monomers in the conditions of TA and SGA showed that in this temperature range a slight gas evolution is observed, along with a minor loss of sample weight ($\ll 10 \text{ wt}\%$). In the case of metal acrylates and maleates main contribution is made by CO_2 and vapor $\text{CH}_2=\text{CHCOOH}$ and $\text{HOOCCH}=\text{CHCOOH}$, condensed on the walls reactor at room

temperature, respectively. This is confirmed by IR and mass spectroscopy. Typical polymerization temperature ranges T_{polym} , according to the TA, are ~ 543 K (CoAcr₂), ~ 563 K (NiAcr₂), ~ 510 K (CuAcr₂), ~ 518 K (FeAcr₃), 488–518 K (CoMal), ~ 518 K (FeMal). During the polymerization there is a change in the IR absorption spectrum of the dehydrated monomer associated with decreasing band absorption intensity of the valence modes of the C=C bond and stretching absorption frequency of the valence modes of the C=O bond, leading to the emergence of a broadened absorption band in the region 1540–1560 cm^{-1} (Tables 8.6, 8.7 and 8.8). It is characteristic that regularly band (RB) with the $\Psi = 1.27$ ($\delta_{\text{C-H}} 830 \text{ cm}^{-1}$, $\nu_{\text{C-H}} 2930 \text{ cm}^{-1}$) appears during the thermal transformations of NiAcr₂ ($T_{\text{exp}} = 593$ K), at low degrees of gassing (about warm-up time), which disappears with increasing conversion and is not observed at $T_{\text{exp}} = 573$ K. The appearance of the RB indicates the proceeding polymerization process, which precedes the main gassing.

According to the TA analysis results during Fe(III) maleate thermolysis the sample weight loss Δm in DTA-effect region with maxima at 433 and 518 K is, respectively, 31.2 and 8.7 wt%. First endoeffect (sufficiently strong) is associated with a dehydration process (5.2% loss of three moles of water molecules), and, apparently, with partial elimination of three molecules of maleic acid (36.8% calc.). The second weak heat effect accompanied by weight loss of the sample is most likely due to the polymerization of desolvated monomer. Finally Δm in this area is about 40%.

8.3.2.3 Decarboxylation

At $T_{\text{therm}} > 523$ K (for CuAcr₂ $T_{\text{therm}} > 453$ K) thermopolymerized samples are subjected to intense gassing (basic gassing). Kinetics of the process under isothermal conditions and in a SGA studied [225] for CuAcr₂ ($<T_{\text{therm}}> = 363$ –513 K), CoAcr₂ (623–663 K), NiAcr₂ (573–633 K), FeAcr₃ (473–643 K), FeCoAcr (613–633 K), Fe₂CoAcr (613–633 K), Fe₂NiAcr (603–643 K), CoMal (613–643 K), FeMal (573–643 K).

The rate of gas evolution $W = d\eta/dt$ decreases monotonically with increasing conversion $\eta = \Delta\alpha_{\Sigma, t} / \Delta\alpha_{\Sigma, f}$, where $\Delta\alpha_{\Sigma, t} = \alpha_{\Sigma, t} - \alpha_{\Sigma, 0}$, $\Delta\alpha_{\Sigma, f} = \alpha_{\Sigma, f} - \alpha_{\Sigma, 0}$, $\alpha_{\Sigma, f}$, $\alpha_{\Sigma, t}$ and $\alpha_{\Sigma, 0}$, respectively, the final, current and initial moles of the separated gaseous products on 1 mol of the initial sample at room temperature. Kinetics of gassing $\eta(\tau)$ in general (up $\eta \leq 0.95$) satisfactorily approximated by the equation for the two parallel reactions:

$$\eta(\tau) = \eta_{1f}[1 - \exp(-k_1\tau)] + (1 - \eta_{1f})[1 - \exp(-k_2\tau)] \quad (8.1)$$

where $\tau = t - t_0$ (t_0 —the warm-up sample, $\eta_{1f} = \eta(\tau)|_{k_2t \rightarrow 0, k_1t \rightarrow \infty}$), k_1 , k_2 —effective rate constants. Parameters k_1 , k_2 , η_{1f} , $\Delta\alpha_{\Sigma, f}$ depend on T_{therm} :

Table 8.6 Values of vibration frequencies in the IR spectra of Cu(II) acrylate, its polymer and decomposition products [210]

CuAc ₂		Polyacrylate Cu(II)		CuAc ₂ decomposition product	
ν , cm ⁻¹	I _{rel}	ν , cm ⁻¹	I _{rel}	ν , cm ⁻¹	I _{rel}
3100	0.02	V _{as} C-H (=CH ₂)			
3045	0.10	V _{as} C-H (=CH-)			
3030 sh	0.02				
2950	0.03	V _s C-H (=CH ₂)	0.06	2975	0.10
2930	0.06	V _s C-H (=CH-)	0.10	2925	0.23
2900 sh	0.02		0.12	2915	0.175
2850	0.03		0.05	2850	0.27
2790	0.02				
2730	0.02				
1945	0.02				
1645	0.49	ν C-C (C=C)	0.08	1640	0.13
1580	1.00	V _{as} C-O (COO)	1.00	1560	1.00
1560 sh	0.44		0.51	1550 sh	1.00
1515	0.33	δ C-H (-CHCH ₂)	0.32	1515	0.57
1440	0.82		0.44	1415	1.00
1370	0.46	V _s C-O (COO)	0.26	1345	0.62
1275	0.34	ρ_t (CH ₂)	0.14	1275	0.24
			0.19	1240	
1065	0.27	ν C-C (=CH-C)	0.19	1075	0.58
995	0.41	π (-CHCH ₂)	0.13	980	0.32
975	0.46		0.19	940	0.47
915	0.09	π (-CHCH ₂)			
830	0.50	ρ_w (CH ₂)	0.20	815	0.53
695	0.48	ρ_t (CH ₂)	0.20	678	0.81

Note I_{rel} = D_v/D_v^{max} is relative intensity, D_v is absorption at ν frequency. Vibrations: ν stretching, δ bending, ρ_t twisting, ρ_w wagging, ρ_t rocking, π out-of-plane

Table 8.7 Values of vibration frequencies in the IR spectra of Fe₂CoAc and decomposition products [2.15]

Cocrystallizate Fe ₂ CoAc		Fe ₂ CoAc decomposition products							
ν/cm ⁻¹	I _{rel}	Assignment	Δm = 25.1%		Δm = 37.3%		Δm = 42.0%		Assignment
			ν/cm ⁻¹	I _{rel}	ν/cm ⁻¹	I _{rel}	ν/cm ⁻¹	I _{rel}	
3000–3600 br		ν(OH) (H ₂ O)							
3045		ν _{as} (CH)							
2960		ν _s (CH)	2930						
1630	0.74	ν(C=C), δ(OH)(H ₂ O)	1640	0.35	1680	0.46	1685	0.38	ν(C=C)
1575	1.00	ν _{as} (COO) (Fe cluster)	1555	1.00	1555	1.00	1565	1.00	ν _{as} (COO) (Fe cluster)
1540	0.80	ν _{as} (COO) (Co)	1540	0.99	1540	0.99	1550	1.07	ν _{as} (COO) (Co)
1525	0.77	ν _{as} (COO) (Fe cluster)	1520	0.92	1520	0.98	1520	0.99	ν _{as} (COO) (Fe cluster)
1505	0.485	ν _{as} (COO) (Co)	1505 sh	0.715	1498	0.89			ν _{as} (COO) (Co)
1490 sh	0.39	δ(CH)	1490	0.6					δ(CH)
1435	0.92	ν _s (COO) (Fe cluster)	1435	0.85	1440	1.02	1420	1.23	ν _s (COO) (Fe cluster), ν(OH ₂) (–CH ₂ –CHR–)
1420	0.92	ν _s (COO) (Co)	1415	0.85	1408	1.07			ν _s (COO) (Co), δ(OH ₂) (H ₂ C–CR–)
1360	0.82	ν _s (COO) (Fe cluster)	1400	0.97	1395	1.10	1400	1.20	ν _s (COO) (Fe cluster), δ(OH ₂) (CH ₂ =CR–)
1350	0.71		1315	0.57					ν _s (COO) (Co), δ(OH) (–CH ₂ –CHR–)
1270	0.44	ρ _t (CH ₂)	1280sh	0.51	1270 sh	0.665	1265	1.08	ρ _t (CH ₂) (CH ₂ –CH=CH–) trans
			1185	0.35	1160		1150	1.37	ν(C–C) (=CH–CHR–)

(continued)

Table 8.7 (continued)

Cocrystallize Fe ₂ CoAc		Fe ₂ CoAc decomposition products							
ν/cm ⁻¹	I _{rel}	Assignment	Δm = 25.1%		Δm = 37.3%		Δm = 42.0%		Assignment
			ν/cm ⁻¹	I _{rel}	ν/cm ⁻¹	I _{rel}	ν/cm ⁻¹	I _{rel}	
1120 br	0.10								
1068	0.32	ν(C-C)							
990	0.38	π(CH) (-CH=CH ₂)							
965	0.31	(-CH=CH ₂)							
910	0.07	ρ(OH) (H ₂ O), ν(M-OH ₂)	855	0.08	860	0.15	875	0.33	δ(CH) (-CH=CHR)
830	0.61	ρ _w (CH ₂)	835	0.09	830	0.10	830	0.20	ρ _w (CH) (-CH ₂ -CHR-)
728	0.12		775	0.07	755	0.11	750	1.11	
673	0.50	ρ _t (CH ₂), δ(M-OH ₂)	645 br	0.03					ρ _t (CH) (-CH ₂ -CR=CH-) _{cis} , δ(CH ₂)
598	0.11	δ(CH ₂), δ(M-OH ₂)	592	0.02					ρ _w (CH) (-CH=CHR)
545	0.07	δ(CH ₂), δ(M-OH ₂)							

Table 8.8 Values of vibration frequencies in the IR spectra of CoAcCr₂, its polymer and decomposition products [211]

CoAcCr ₂ ·H ₂ O		Polyacrylate Co(II)		CoAcCr ₂ dehydration products		CoAcCr ₂ decomposition products		
ν , cm ⁻¹	I _{rel}	Assignment	ν , cm ⁻¹	I _{rel}	Assignment	ν , cm ⁻¹	I _{rel}	Assignment
3000–3600 br	0.24	(3400 cm ⁻¹) ν O–H			(3400 cm ⁻¹) ν O–H			
3100	0.03	ν_{as} C–H (=CH ₂)	3100	0.04	ν_{as} C–H (=CH ₂)			
3050	0.03	ν_{as} C–H (=CH–)	3050	0.03	ν_{as} C–H (=CH–)			
3025	0.03	ν_s C–H (=CH ₂)						
2985	0.03							
2925	0.03		2930	0.15	ν_s C–H–CH ₂ –	2925	0.03	ν_s C–H (=CH ₂)
2850	0.02	ν_s C–H (=CH–)	2860	0.06	ν_s C–H (=CH–)	2860	0.03	ν_s C–H (=CH–)
1975	0.02	overtone (2 × 960)	1925	0.04	Overtone			2730
1655	0.63	ν (C=C), δ O–H (H ₂ O)	1655	0.92'	ν (C=C) _{conc}	1655	0.50	ν (C=C)
1595	1.00	ν_{as} C–O (COO)	1595	0.92	ν_{as} C–O (COO)	1580	0.90	ν_{as} C–O (COO)
1585	1.00		1575	1.00				1565
			1535 sh	0.66				1535 sh
1450	1.00	δ C–H (–CHCH ₂)	1450	0.92	δ C–H (–CHCH ₂)	1455	1.00	δ C–H (–CHCH ₂)
			1435 sh	0.79	CHCH ₂)			1415
1370	0.68	ν_s C–O (COO)	1375	0.68	ν_s C–O (COO)	1365	0.675	ν_s C–O (COO)
								1385
								0.51
								ν_s C–O (COO)

(continued)

Table 8.8 (continued)

CoAcCr ₂ :H ₂ O		Polyacrylate Co(II)			CoAcCr ₂ dehydration products			CoAcCr ₂ decomposition products			
ν , cm ⁻¹	I_{rel}	Assignment	ν , cm ⁻¹	I_{rel}	Assignment	ν , cm ⁻¹	I_{rel}	Assignment	ν , cm ⁻¹	I_{rel}	Assignment
1285	0.44	$\rho_t(\text{CH}_2)$	1285	0.49	$\rho_t(\text{CH}_2)$	1280	0.57	$\rho_t(\text{CH}_2)$	1260	0.39	$\rho_t(\text{CH}_2)$
1070	0.15	$\nu \text{ C}-\text{C} (= \text{CH}-\text{C})$	1060	0.14	$\nu \text{ C}-\text{C} (= \text{CH}-\text{C})_{conc}$	1070	0.10	$\nu \text{ C}-\text{C} (= \text{CH}-\text{C})$	1235	0.375	
995	0.31	$\pi(-\text{CHCH}_2)$	995	0.21	$\pi(-\text{CHCH}_2)$	990	0.31	$\pi(-\text{CHCH}_2)$	1130	0.06	
960	0.28		975	0.17		965	0.28		1080	0.05	$\nu \text{ C}-\text{C} (= \text{CH}-\text{C})$
880	0.05	$\rho\text{OH} (\text{H}_2\text{O}), \nu(\text{M}-\text{OH}_2)$							1010	0.14	$\pi(-\text{CHCH}_2)$
840	0.42	$\rho_w(\text{CH}_2)$	835	0.26	$\rho_w(\text{CH}_2)$	835	0.43	$\rho_w(\text{CH}_2)$	985	0.125	
685	0.24	$\rho_t(\text{CH}_2), \delta(\text{M}-\text{OH}_2)$	685	0.06	$\rho_t(\text{CH}_2)$	690	0.195	$\rho_t(\text{CH}_2)$			
590	0.06	$\delta(\text{CH}_2), \delta(\text{M}-\text{OH}_2)$				590	0.032	$\delta(\text{CH}_2)$			

$$\eta_{1f}, \Delta\alpha_{\Sigma, f} = A \exp[-E_{a, \text{eff}}/(RT_{\text{therm}})] \quad (8.2)$$

$$k_{\text{eff}} = k_{0, \text{eff}} \exp[-E_{a, \text{eff}}/(RT_{\text{term}})] \quad (8.3)$$

where A , $k_{0, \text{eff}}$ is pre-exponential factor, $E_{a, \text{eff}}$ is the effective activation energy.

The initial rate of gas evolution $W_{\tau=0} = W_0$ will

$$W_0 = \eta_{1f}k_1 + (1 - \eta_{1f})k_2 \quad (8.4)$$

Equations (8.1) and (8.4) describe the kinetics of the gassing NiAcAc₂, FeCoAcAc, Fe₂CoAcAc, Fe₂NiAcAc and FeMal (Fig. 8.15) [213, 215, 219].

At $k_2 \approx 0$, $\eta_{1f} \rightarrow 1$

$$\eta(\tau) \approx 1 - \exp(-k_1 \tau) \quad (8.5)$$

$$W_0 \approx k_1 \quad (8.6)$$

Equations (8.5) and (8.6) describe the kinetics of the gassing during thermal transformations of CoAcAc₂ and CoMal (Figs. 8.16 and 8.17).

In the case where $\tau \ll 1/k_2$, $k_1 \gg k_2$,

$$\eta(\tau) \approx \eta_{1f}[1 - \exp(-k_1 \tau)] + (1 - \eta_{1f})k_2 \tau \quad (8.7)$$

$$W_0 \approx \eta_{1f}k_1 \quad (8.8)$$

The dependence η of the time (t) during CuAcAc₂ thermolysis satisfactorily described by (8.7) (Fig. 8.18).

The kinetic parameters of gas evolution at thermal transformations of the studied compounds are presented in Table 8.9.

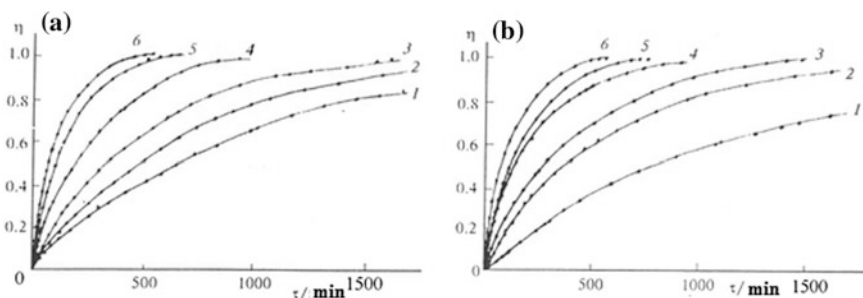


Fig. 8.15 The kinetics of accumulation of gaseous products at thermal transformation of cocrystallizates FeCoAcAc (a) and Fe₂CoAcAc (b). Curves are calculation of the (8.1), points are the experimental values: $T_{\text{exp}} = 613$ (1), 623 (2), 633 (3), 643, 653 (5), 663 K (6); $m_0/V = 1.80 (\pm 0.05) \times 10^{-3}$

Fig. 8.16 Kinetics of the thermal decomposition of CoAcr: **a** dependence $\eta(t)$ at various temperatures: 663 (1), 653 (2), 643 (3), 633 (4) 623 K (5); **b** the dependence $\lg k$ versus $1/T$

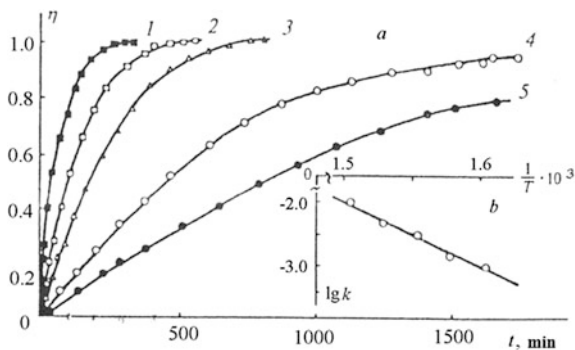


Fig. 8.17 Gas evolution kinetics $\eta(\tau)$ (a) and semilogarithmic lines ($\log(1 - \eta)$ vs. τ) (b) for the thermolysis of Co(II) maleate (CoMal) in SGA at 653 (1), 643 (2), 633 (3), 623 (4), and 613 K (5)

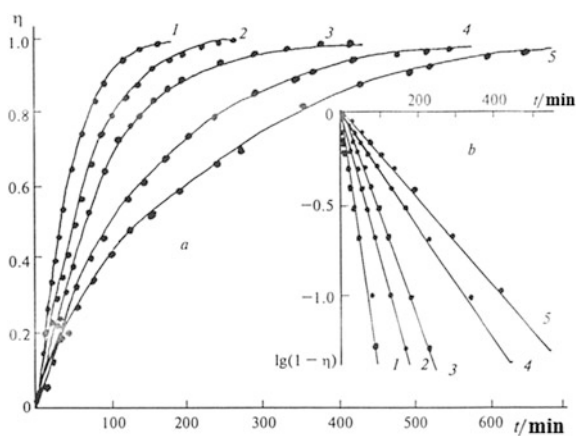


Fig. 8.18 Dependence $\eta(t)$ during the thermolysis of CuAcr₂: 1—463, 2—473, 3—483, 4—493, 5—503, 6—513 K; $m_0/v = 2.45 (\pm 0.1) \times 10^{-3}$

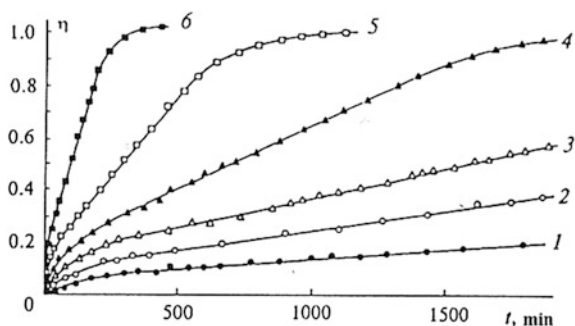


Table 8.9 Kinetic parameters of gassing during thermolysis of metal acrylates and maleates [181, 225]

Sample	$\eta_{16}, \Delta\alpha_{\Sigma, f} = A \exp[-E_{a,eff}/(RT_{therm})]$		k	$k_{eff} = k_{0,eff} \exp[-E_{a,eff}/(RT_{therm})]$		$W_0 = k_{0,eff} \exp[-E_{a,eff}/(RT_{therm})]$	
	η_{16}	$\Delta\alpha_{\Sigma, f}$		$E_{a,eff}$ (kJ mol ⁻¹)	$k_{0,eff}$ (s ⁻¹)	$E_{a,eff}$ (kJ mol ⁻¹)	$k_{0,eff}$ (s ⁻¹)
CuAcAc ₂	η_{16}	1.8×10^4	48.1	k_1	9.5×10^{11}	9.5×10^{11}	202.7
	$\Delta\alpha_{\Sigma, f}$	3.6	12.5	k_2	9.2×10^{11}	163.0	
CoAcAc ₂	η_{16}	1.0	0	k_1	3.0×10^{14}	3.0×10^{14}	238.3
	$\Delta\alpha_{\Sigma, f}$	1.55	0	k_2		0	
FeAcAc ₃ (473–573 K) (573–643 K)	η_{16}	1.0	0	k_1	4.2×10^{21}	4.2×10^{21}	246.5
	$\Delta\alpha_{\Sigma, f}$	1.6×10^2	25.5	k_2	0	0	127.5
	η_{16}	1.0	0	k_1	1.3×10^6	1.3×10^6	127.5
	$\Delta\alpha_{\Sigma, f}$	1.7×10^2	26.3	k_2	0	0	
NiAcAc ₂	η_{16}	2.6	4.6	k_1	1.7×10^{17}	1.7×10^{17}	242.4
	$\Delta\alpha_{\Sigma, f}$	1.4×10^{11}	125.4	k_2	7.5×10^8	156.7	156.7
FeCoAcAc	η_{16}	0.45 (663 K) – 0.65 (613 K)		k_1	2.3×10^{12}	2.3×10^{12}	207.0
	$\Delta\alpha_{\Sigma, f}$	5.25×10^2	31.3	k_2	6.0×10^6	138.0	
Fe ₂ CoAcAc	η_{16}	0.35 (663 K) – 0.50 (613 K)		k_1	2.6×10^{12}	2.6×10^{12}	205.0
	$\Delta\alpha_{\Sigma, f}$	1.5×10^2	25.1	k_2	6.6×10^5	125.5	
Fe ₂ NiAcAc	η_{16}	4.4×10^7	75.0	k_1	6.1×10^6	6.1×10^6	205.0
	$\Delta\alpha_{\Sigma, f}$	6.5×10^2	25.5	k_2	0.6×10^2	79.4	
CoMal	η_{16}	1.0	0	k_1	1.1×10^6	1.1×10^6	125.4
	$\Delta\alpha_{\Sigma, f}$	1.3×10^2	23.4	k_2	0	0	
FeMal	η_{16}	0.59×10^2	23.4	k_1	3.3×10^7	3.3×10^7	133.8
	$\Delta\alpha_{\Sigma, f}$	4.78 (573 K) – 7.40 (643 K)		k_2	1.0×10^7	110.8	

It should be noted that two gassing areas are observed at heating thermopolymerized FeAc₃ (Fig. 8.19) [225]: low temperature ($\langle T_{\text{therm}} \rangle = 473\text{--}573\text{ K}$) and high temperature ($\langle T_{\text{therm}} \rangle = 603\text{--}643\text{ K}$). Their gassing rate is well approximated by the (8.5–8.6), but with different values of k and $\Delta\alpha_{\Sigma, f}$ (see Table 8.9). It is possible that the difference in kinetic parameters of FeAc₃ thermolysis in low- and high-temperature areas, or in the case of FeCoAc, Fe₂CoAc, Fe₂NiAc difference in η_{1f} value level at a constant other kinetic parameters ($\Delta\alpha_{\Sigma, f}$, k_1 , k_2), is due to the presence of two parallel processes of gassing.

Using the values W_0 , studied metal acrylates can be arranged in series to reduce the reactivity of a gassing: $\text{Cu} \geq \text{Fe} > \text{Co} > \text{Ni}$. At that the values of effective activation energies of the initial rate of gas evolution in a SGA of CuAc₂ ($E_{a,\text{eff}} = 202.7\text{ kJ mol}^{-1}$), NiAc₂ ($E_{a,\text{eff}} = 246.6\text{ kJ mol}^{-1}$) shown in Table 8.9 are close to the calculated values of $E_{a,\text{eff}}$ for thermolysis in TA regime [190]: 211.1 and 244.1 kJ mol^{-1} . At the same time, $E_{a,\text{eff}} = 238.3\text{ kJ mol}^{-1}$ of initial rate of CoAc₂ thermolysis in SGA is above the corresponding value of $E_{a,\text{eff}} = 206.1\text{ kJ mol}^{-1}$ for thermal transformation in a TA conditions. Attention is drawn to the difference in gassing rate constants of cobalt acrylate and maleate thermolysis. The values of the activation parameters of FeMal are close to the values of the activation parameters of gassing rate constants of FeAc₃, FeCoAc, Fe₂CoAc, and Fe₂NiAc in this T_{therm} region.

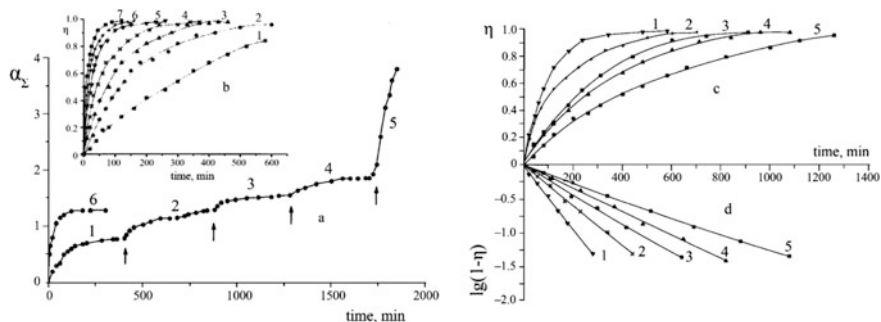


Fig. 8.19 **a** The kinetics of gas evolution from FeAc₃ at T_{exp} (°C): 1, 215; 2, 250; 3, 275; 4, 300; 5, 350; 6, 240. The moment of T_{exp} increasing is shown by pointer. **b** Dependence $\eta(T)$ on T_{exp} (°C): 1, 200; 2, 205; 3, 210; 4, 215; 5, 220; 6, 230; 7, 240 ($m_o/V = 6.7 \times 10^{-3}\text{ g cm}^3$ where m_o is start mass of sample). **c** The dependence $\eta(t)$ on $T_{\text{exp}} = 300\text{--}370\text{ °C}$: 1, 370; 2, 360; 3, 350; 4, 340; 5, 330 °C. **d** The semilogarithmic anamorphous of the dependence $\eta(t)$

8.3.3 The Composition of the Gaseous and Solid Thermolysis Products of Metal-Containing Monomers

8.3.3.1 The Gaseous and Condensed Products

The major gaseous product of the conversion of the investigated acrylates and maleates metals, their cocrystallizates is CO₂. This is confirmed by IR spectroscopy and mass spectrometry (MS) observations. CO (IR, MS), H₂ (MS), and condensed at T_{room} H₂O vapor (IR, MS) and ligands CH₂=CHCOOH (IR, MS), HOCOCH=CHCOOH (IR, MS), which are the products pyrolysis of the corresponding complexes, are evolved in a much smaller amount. The evolution of the main quantity of condensed product vapor is observed in the early stages of the gas evolution (during the warm-up sample $\alpha_{\Sigma,0}$) and is associated with dehydration and solid state polymerization processes, which are the previous main gassing. This is evidenced by a comparison of the amount of the evolved gaseous products and sample weight loss. Besides these gaseous products CH₄ (IR, MS) was detected in the case CoAcr₂ (trace) and NiAcr₂ (co-measurable with the amount of CO₂) (Table 8.10). C₂H₄ (IR, MS) is formed in the transformation products of CuAcr₂ in measurable quantities.

In the IR spectra of gaseous products that condense at 88 K (Fig. 8.20) there is a system of characteristic absorption bands in the regions 3600–3700, 2320–2340, 625–670 cm⁻¹ associated with CO₂ oscillations. Absorptions at frequencies 2990, 2930, 1750sh, 1725, 1630, 1370, 1350 cm⁻¹ related to oscillations $\nu(\text{C-H})$, $\nu(\text{C=O})$,

Table 8.10 The composition of the gaseous and condensable thermolysis products of metal-containing monomers [213, 214, 218, 221, 222]

Sample	Products (% of.)						
	Condensable at 88 K				Non-condensable at 88 K		
	CO ₂	C ₂ H ₄	Vapor CH ₂ =CHC(O)OH (HOC(O)CH=CHC(O)OH)	Vapor H ₂ O	H ₂	CO	CH ₄
CoAcr ₂	>90	–	+	+	56.8	34.0	9.2
CuAcr ₂	>90	5–6	+	+	19.4	77.6	3
NiAcr ₂	79		+	+	0.5	~0.5	18.5 (from α_{Σ}^{Σ})
FeAcr ₃	90–93	–	+	2.3	(2.7 from α_{Σ}^{Σ})	–	–
CoMal	90	–	+	+	2–2.5 from α_{Σ}^{Σ}	2–2.5 from α_{Σ}^{Σ}	–
FeMal	90	–	+	+	Trace	≤ 10 from α_{Σ}^{Σ} CO ₂	

Fig. 8.20 The IR absorption spectra of the gaseous products (1) and the product condensed on the walls of the reaction vessel (2) during the thermal transformations of CoAcr_2

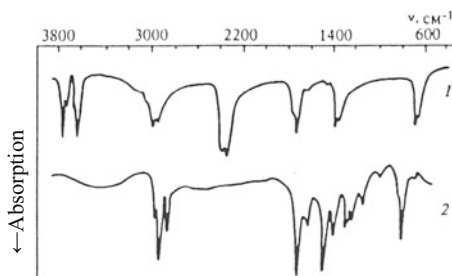
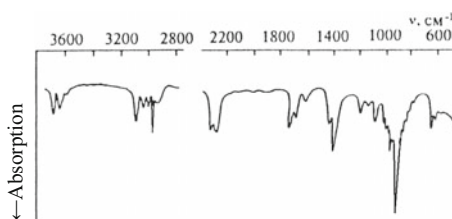


Fig. 8.21 The IR absorption spectra of the gaseous products of thermal transformations of CuAcr_2 , non-condensing at 88 K



$\nu(\text{C}=\text{C})$, $\delta(\text{C}-\text{H})$ are likely to be due to the presence of vapor $\text{CH}_2=\text{CHCOOH}$. In the case of CuAcr_2 in similar IR spectra there also are absorption bands characteristic C_2H_4 ($\nu(\text{CH})$ 3106, 3020, 3000, 2970 cm^{-1} ; $\nu(\text{C}=\text{C})$ 1625 cm^{-1} ; $\delta_{\text{as}}(\text{CH}_2)$ 1445 cm^{-1} ; $\delta_{\text{s}}(\text{CH}_2)$ 1380 cm^{-1} ; $\rho_{\text{w}}(\text{CH}_2)$ 950 cm^{-1} . In the IR spectra of the gaseous products which are not condensable at 88 K, there are absorption bands in the region 2140 and 2100 cm^{-1} associated with CO oscillations (Fig. 8.21) [213].

The level of total gassing at the transformation end ($\alpha_{\Sigma, f}$) is different for each of the studied acrylates and maleates, and increases with T_{therm} (see Table 8.9). At a constant value of T_{therm} , $\alpha_{\Sigma, f}$ increases with increasing content of Acr-ligands in the acrylate monomers. With increasing T_{therm} sample weight loss at the end of gas evolution also increases, but does not reach the values that can be expected from the decomposition of metal carboxylates to the metal or its oxide.

8.3.3.2 The Composition of the Solid-Phase Products

During the transformation of investigated metal-containing monomers with increasing $\alpha_{\Sigma, t}$ changes in the IR absorption spectra of solid thermolysis products are observed. They lie in the evolution of the relative intensity of the absorption bands I_{rel} and shift the absorption frequencies. Despite the inherent individuality of each of the studied compounds in the changes in the IR absorption spectrum, there are general patterns associated primarily with the mode system of $\text{C}=\text{C}$ and COO bonds:

- (i) At low gassing degrees, including FeAc_3 thermolysis at low temperatures, I_{rel} of modes $\nu(>\text{C}=\text{C}<)$, $\rho(\text{CH}_2)$, $\nu(=\text{C}-\text{C})$, $\pi(-\text{CH}=\text{CH}_2)$ falls and IR absorption spectrum becomes closest to the IR absorption spectrum of polyacrylate [226] and polymaleates [227, 228] of corresponding metal. This is evidenced by a comparison I_{rel} in the IR spectra of the thermolysis products and individual polyacrylate and polymaleate.
- (ii) Increasing the gassing degree leads to a drop I_{rel} of stretching $\nu(\text{C}(\text{O})-\text{O})$ and bending $\delta(\text{C}-\text{O})$ modes up to their complete disappearance. This indicates decomposition of carboxylate groups.
- (iii) Simultaneously with the fall I_{rel} of the $\text{C}(\text{O})\text{O}$ -mode, a shift of the absorption bands of the stretching $\nu(\text{C}-\text{H})$ modes in the high-frequency region is observed that indicates the reinforcement of $\text{C}-\text{H}$ bond. This is typical of $=\text{CH}$ -fragments.
- (iv) Absorption in the region $1630-1655 \text{ cm}^{-1}$ related to $\nu(\text{C}=\text{C}-)$ modes, shifted in high-frequency region $1685-1720 \text{ cm}^{-1}$ with decreasing I_{rel} . This may be due to the appearance of stretching modes in the conjugated $\text{C}=\text{C}$ -fragments of products.

In general, quantitative monitoring of evolution in the transformation of the IR absorption spectra of the solid thermolysis products of the studied carboxylates suggest the decarboxylation of metal-containing fragments and the appearance of conjugated $\text{C}=\text{C}$ bonds.

Electron microscopic study of the final thermolysis products of CoAc_2 , FeAc_3 , CoMal , Fe_2NiAc , FeCoAc , Fe_2CoAc showed that they are characterized by a morphologically close pattern: there are electron-dense particles dispersed in the

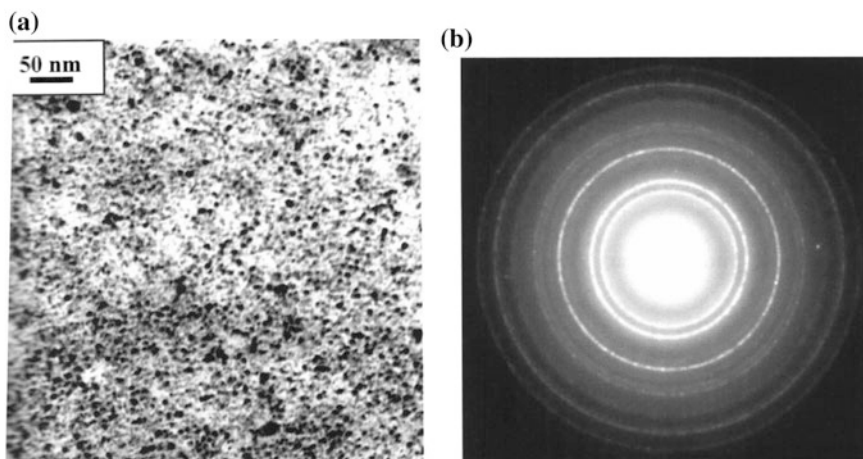


Fig. 8.22 TEM microstructure (a) and electron diffraction (b) of the thermolysis product of CoAc_2 at 643 K

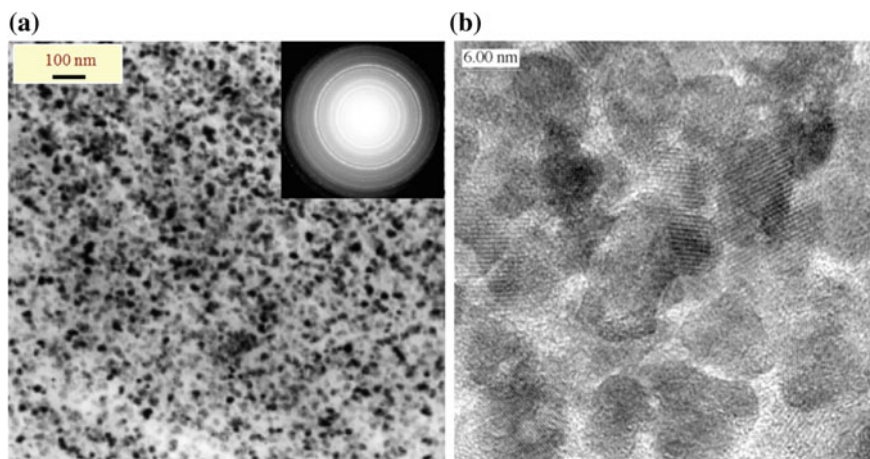


Fig. 8.23 Thermolysis product microstructure of Fe_2CoAcr at 643 K according to the TEM (a) and HRTEM (b)

Table 8.11 The average size of the spherical clusters in decarboxylated matrix

Sample	CoAcr_2	FeAcr_3	FeCoAcr	Fe_2CoAcr	Fe_2NiAcr	CoMal
$d_{\text{EM, av}}, \text{ nm}$	7	7–9	5–6	5–6	6–8	3–4

electron-less dense matrix. The particles are close to spherical in shape, have a narrow size distribution and are present both individually and in the form of aggregates of 3–10 particles (Figs. 8.22 and 8.23). The average particle diameter ($d_{\text{EM, av}}$) is shown in Table 8.11.

Nanoscale particles are sufficiently uniformly in the matrix with a mean particle centers distance from each other of 8–10 nm. In the case of CoMal , along with nano-sized spherical particles relatively large aggregates in the form of a cubic crystal habitus with dimensions of 10–20 nm are simultaneously observed. Assuming that the volume of the starting acrylate consumed to form a metal-containing particle MO_x (size d_{MO_x} and specific density ρ_{MO_x}) has as initial particle MAcr_n itself, spherical symmetry and a diameter d_{Acr} , the final product is a decarboxylated matrix $-(\text{CH}_2\text{CH}=\text{CHCH}_2)_n-$ with immobilized MO_x molecules in it and has an average density of $\bar{\rho}_{\text{prod}} \approx 0.5(\rho_{\text{MO}_x} + \rho_{\text{Acr}})$, where ρ_{Acr} is the density of the starting monomer ($\rho_{\text{Acr}} = 1.5 \text{ g cm}^{-3}$), we get the average distance d_{prod} between the centers of nano-sized particles:

$$d_{\text{prod}} = d_{\text{MO}_x} \xi^{1/3}$$

($\xi = \rho_{\text{MO}_x}(1 + n\mu_2/\mu_1)/\bar{\rho}_{\text{prod}}$, $\mu_1 = \mu_{\text{MO}_x}$ is molecular weight of MO_x , $\mu_2 = \mu_{\text{CH}_2\text{CH}}$, n is the number of Acr groups in the starting monomer per one atom M).

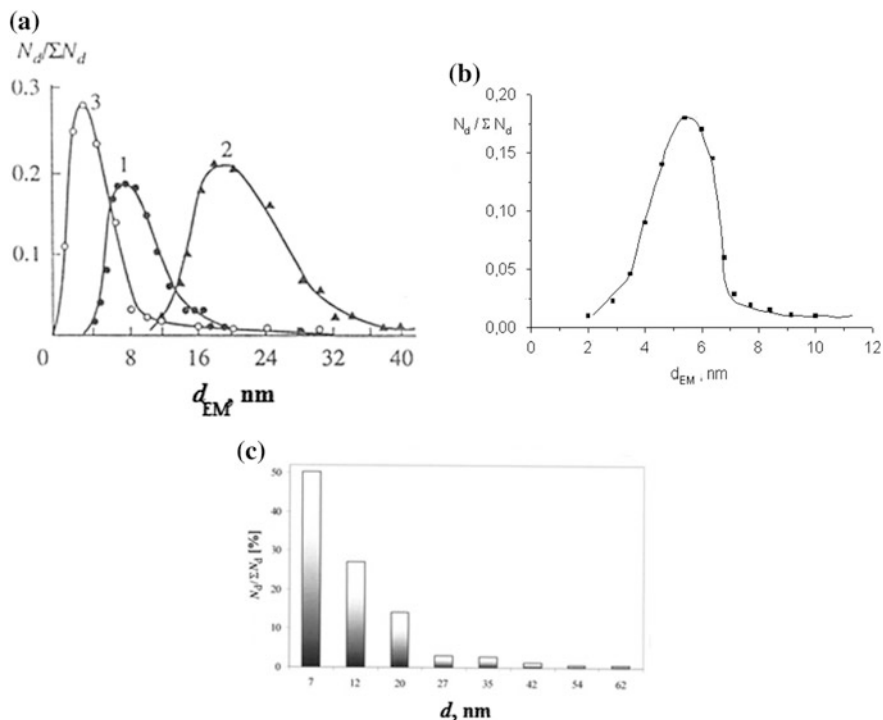


Fig. 8.24 The size distribution of metal-containing particles. Products of thermal transformation of metal carboxylates **a**: 1—FeAcr₃, 2—Fe(HCOO)₂·2H₂O, 3—CoMal, **b** cocrystallizate Fe₂CoAcr and **c** CoAcr₂

For $\rho_{MOx} = 5.2 \text{ g cm}^{-3}$ (specific density of Fe₃O₄ or Fe₂CoO₄), $\bar{\rho}_{prod} = 3.35 \text{ g cm}^{-3}$, $\mu_{MOx} = 78$, $\mu_{CH_2CH} = 27$, $n = 3$ we have $d_{prod} \cong 1.5 \bar{d}_{MOx}$. Thus for $\bar{d}_{MOx} = 5.0$ – 9.0 nm we have $\bar{d}_{prod} = 7.5$ – 13.5 nm , which is close to the observed distance between the particles in the decarboxylated matrix.

It should be noted that the average size of the particles formed during thermolysis of unsaturated metal carboxylates is lower than that observed for the products of thermal transformations of saturated metal carboxylates (Fig. 8.24) [229].

Thus, during the process of thermal transformations of metal carboxylates the material consisting of nanoscale metal particles stabilized in the matrix with a narrow size distribution is formed. The phase composition, morphology and structure of the formed nanocomposites are discussed in more detail below.

8.3.4 Kinetic Schemes and Thermal Transformation Reactions of Metal-Containing Monomers

Thermal transformations of metal-containing monomers are associated with the following three successive macrostages:

- (i) Dehydration of monomer crystallohydrates ($T_{\text{therm}} < 423$ K) with the simultaneous restructuring of the ligand environment, accompanied by the evolution of the carboxylate ligands (acrylic acid and maleic acid, respectively);
- (ii) Solid state polymerization of rebuilt dehydrated monomer ($T_{\text{therm}} \approx 453$ – 493 K);
- (iii) Decarboxylation of the resulting (co)polymer at high temperatures ($T_{\text{therm}} > 473$ K). The main gassing and sample weight loss during thermolysis is connected with the latter process.

Metal carboxylate thermal stability can be measured by the relative strength of the interatomic M–O and C–O bonds in its crystallochemical structure. The M–O and C–O bond lengths within the coordination polyhedron can vary significantly, which indicates their energy disparities. According to IR spectroscopy of dehydrated monomers (see Tables 8.5, 8.6 and 8.7), during dehydration the basic structure unit of metal-containing monomers is generally conserved. But in this case a denticity of certain portion of unsaturated ligands may change and like anhydrous carboxylates of unsaturated acids they are started simultaneously perform the role of a ligand, and a missing solvate function in the crystal structure. Increasing ligand denticity leads to distortion of the metal oxygen environment with a corresponding change in the M–O and C–O distances in the structure, and hence a change in their strength. In particular, the energy disparity of the M–OOCCH=CH₂ in FeAcr₃ indicates [230] dependence of the CH₂=CHCOO–ion fragmentation on the voltage of the accelerating field in the MS studies on fragmentation of [Fe₃O(CH₂=CHCOO)₆]⁺ ion. The mass spectrum at U = 400 V (Fig. 8.25) of the ions with m/z = 539, 468, 397 corresponds to the evolution of one, two or three Acr-groups, and an ion with m/z = 341 corresponds to the evolution of FeAcr₃ molecules from the [Fe₃O(CH₂=CHCOO)₆]⁺ molecular ion.

8.3.4.1 The Total Kinetic Scheme and the Decomposition Pathways of the Metal-Containing Monomers

With increasing the level of the thermal vibrations of the lattice of the dehydrated monomer (with increasing temperature) the break of the weakest M–O bonds is very likely to form a mono- or biradicals of the ligands: CH₂=CHCOO· in the case of acrylates and ·OOCCH=CHCOO· if maleates. Interaction of these radicals with the metal-containing maleate or acrylate moieties leads to the corresponding acids and the radical R· with H-depleted acrylate (maleate) group:

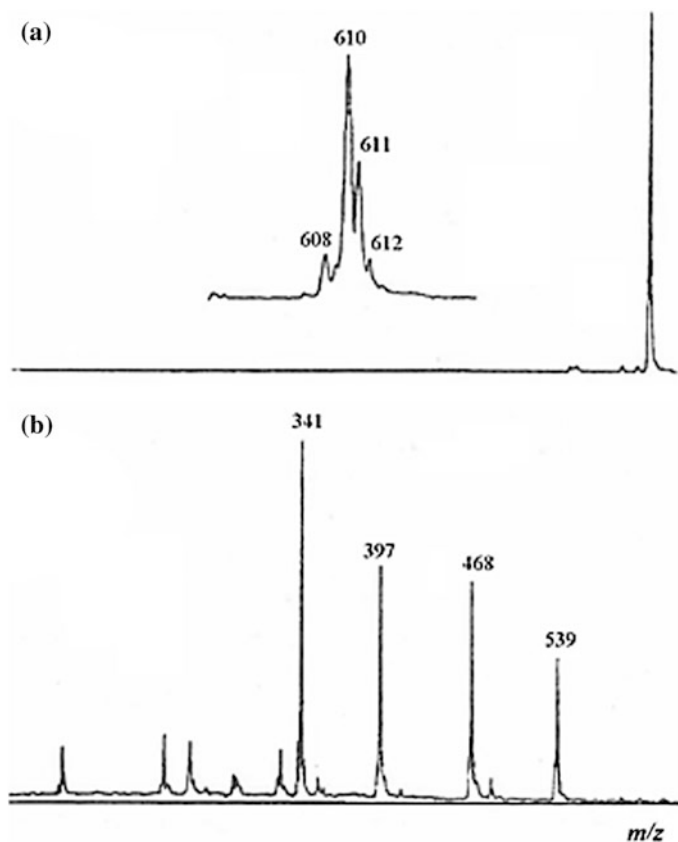
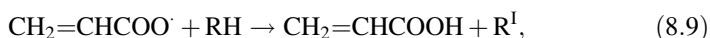
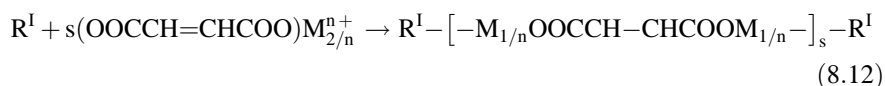
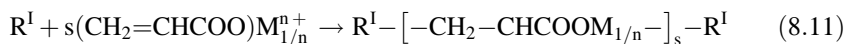


Fig. 8.25 Mass-spectra of positive ions extracted from the aqueous alcoholic solution of FeAc_3 at $U = 200$ V (a) and 400 V (b)

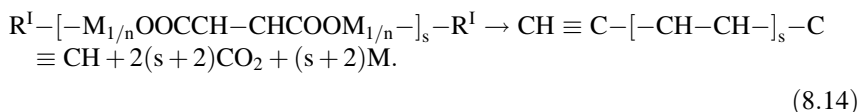
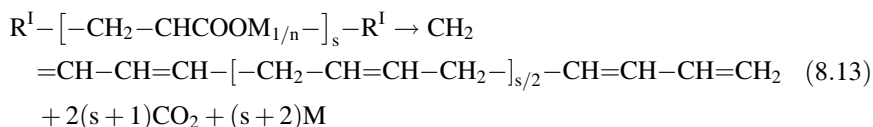


where $\text{RH} = (\text{CH}_2\text{CHCOO})\text{M}_{1/n}^{n+}$, $\text{R}^{\text{I}} = (\cdot\text{CHCHCOO})\text{M}_{1/n}^{n+}$ (in the case of acrylate); $\text{RH} = (\text{CHCOO})_2\text{M}_{2/n}^{n+}$, $\text{R}^{\text{I}} = (\cdot\text{CCOO})_2\text{M}_{1/n}^{n+}$ (in the case of maleate).

The resulting R^{I} radical involved in the growth and chain termination reaction to form a polymer of network or linear structure:

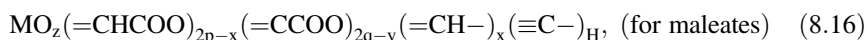
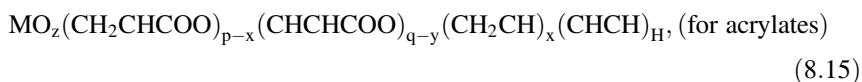


With increasing temperature, the metal-containing groups of the formed polymer undergo decarboxylation to form metal and (or) its oxide:

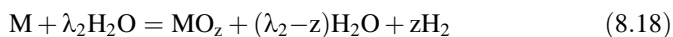
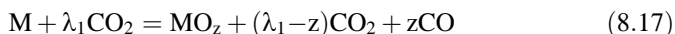


Additional thermopolymerization with participation of multiple bonds in decarboxylated products probably contributes to a cross-linked network structure, as indicated by the absence of reaction product solubility in organic solvents.

Thus, in general form solid product composition change during thermal transformation of metal acrylates and maleates can be expressed as fraction C–H–O-fragments.



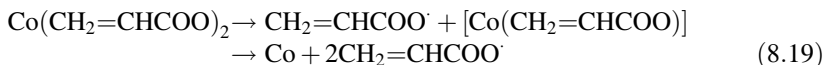
where $x = y = z = 0$ ($z \neq 0$ in the case of FeAcr₃ and FeMal), p and q are accordingly the number of intrachain and terminal H-depleted groups ($p + q = 1$). The most likely way of forming metal oxides is the oxidation reaction.



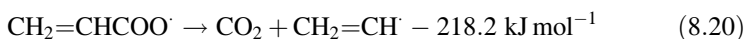
By solving the equations of mass balance using quantitative data on gassing, the sample weight loss, low temperature fractionation and mass spectral analysis of the CO₂, H₂ and CO gaseous products composition and yields of thermolysis product of the analyzed complexes were calculated [213, 214, 217, 221]. Consider this in more detail on the example of CoAcr₂.

8.3.4.2 Transformation Pathways of Cobalt Acrylate

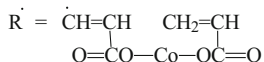
As mentioned above, as a result of dehydration (desolvation) the denticity of the portion of Acr-ligands changes, which results in disparity of M–O bonds. As a consequence the break of weak M–O bond occurs to form a radical CH₂=CHCOO·



The resulting radical $\text{CH}_2=\text{CHCOO}^\cdot$ can later be spent on the following channels:

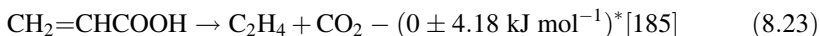
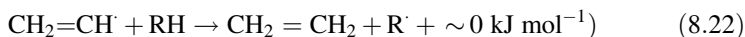


([#]Believed that $E(\text{CH}_2\text{CHCOO}-\text{H}) (\text{g}) = 461.5 \text{ kJ mol}^{-1}$.)

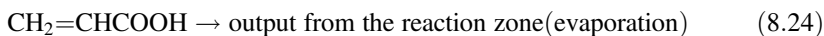


where

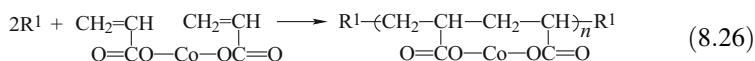
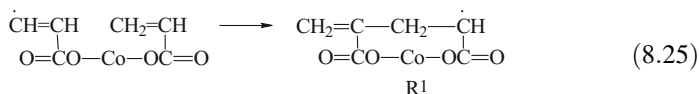
and further



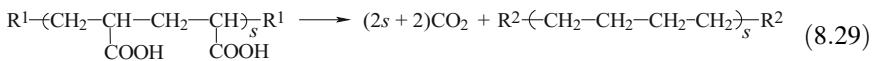
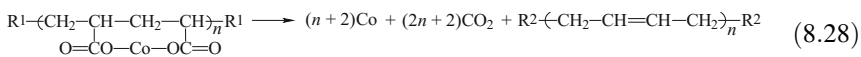
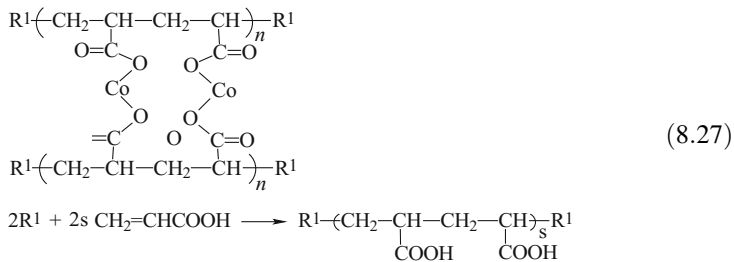
(*Estimates of the thermal effects were carried out for the gas-phase reaction. At that the following data and assumptions are used: $E(\text{CH}_2\text{CHCOO}-\text{H}) (\text{g}) \approx E(\text{MeC}(\text{O})\text{O}-\text{H}) = 461.5 \text{ kJ mol}^{-1}$, $\Delta H_f^\circ(\text{CH}_2\text{CHCOOH}) (\text{l}) = -384.6 \text{ kJ mol}^{-1}$, $\Delta H_{\text{ev}}(\text{CH}_2\text{CHCOOH}) (\text{l}) = 545.6 \text{ kJ mol}^{-1}$. Then $\Delta H_f^\circ(\text{CH}_2\text{CHCOOH}) (\text{g}) = 96.2 \text{ kJ mol}^{-1}$, $\Delta H_f^\circ(\text{CH}_2\text{CH}) (\text{g}) \approx 271.7 \text{ kJ mol}^{-1}$, $\Delta H_f^\circ(\text{C}_2\text{H}_4) (\text{g}) = 52.3 \text{ kJ mol}^{-1}$, $\Delta H_f^\circ(\text{CO}_2) (\text{g}) = -393 \text{ kJ mol}^{-1}$.)



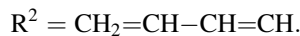
Since C_2H_4 in the gaseous decomposition products of CoAcr_2 (see Table 8.9) is not detected, it can be assumed that in the investigated temperature decomposition range of CoAcr_2 disappearance of the radical $\text{CH}_2=\text{CHCOO}^\cdot$ occurs mainly on the reactions (8.21) and (8.24). The radical formed by the reaction (8.21) can participate in a polymerization of a monomeric carboxylate, and AA [(8.26) and (8.27)], followed by decarboxylation of COOH and $\text{Co}(\text{CO}_2)_2$ fragments of polymer product. It is also likely that these processes are preceded by intramolecular opening of the double bond in R.



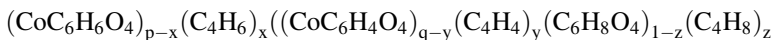
It is assumed that it is possible both linear and network structure of the formed polymer:



where

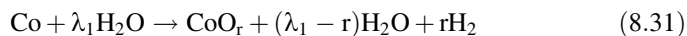
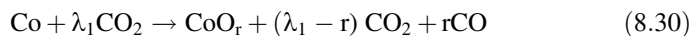


After transformation, the polymeric product (PPr) may have the following composition:



However, with regard to CoAc₂ decomposition that occurs at 623–653 K, it is difficult to expect that $\left(\text{CH}_2-\underset{\text{COOH}}{\text{CH}}\right)$ groups may be present in the PPr, as the latter is eliminated quantity of CO₂ already at 473–488 K [231].

In the non-condensable at 88 K gaseous decomposition products, as already noted, the main components are H₂ and CO, whose appearance is most likely due to the oxidation processes of the resulting metal by H₂O and CO₂ vapor:



Based on the gassing and sample weight loss data as a result of CoAc₂ transformations the following system of equations is compiled relating the values α_i of degradation products:

$$\begin{aligned}
&6\alpha_{\text{C}_6\text{H}_8\text{O}_4} + 4\alpha_{\text{C}_4\text{H}_8} + 6\alpha_{\text{CoC}_6\text{H}_6\text{O}_4} + 4\alpha_{\text{C}_4\text{H}_6} + 6\alpha_{\text{CoC}_6\text{H}_4\text{O}_4} + 4\alpha_{\text{C}_4\text{H}_4} \\
&= 6 - \alpha_{\text{CO}_2} - \alpha_{\text{CO}} - 3\alpha_{\text{C}_3\text{H}_4\text{O}_2} \\
&4\alpha_{\text{C}_6\text{H}_8\text{O}_4} + 4\alpha_{\text{C}_4\text{H}_8} + 3\alpha_{\text{CoC}_6\text{H}_6\text{O}_4} + 3\alpha_{\text{C}_4\text{H}_6} + 2\alpha_{\text{CoC}_6\text{H}_4\text{O}_4} + 2\alpha_{\text{C}_4\text{H}_4} \\
&= 4 - \alpha_{\text{H}_2} - \alpha_{\text{H}_2\text{O}} - 2\alpha_{\text{C}_3\text{H}_4\text{O}_2} \\
&4\alpha_{\text{C}_6\text{H}_8\text{O}_4} + 4\alpha_{\text{CoC}_6\text{H}_6\text{O}_4} + 4\alpha_{\text{CoC}_6\text{H}_4\text{O}_4} = 5 - 2\alpha_{\text{CO}_2} - \alpha_{\text{CO}} - 2\alpha_{\text{C}_3\text{H}_4\text{O}_2} - \alpha_{\text{H}_2\text{O}} - r\alpha_{\text{CoO}_r} \\
&\alpha_{\text{CoO}_r} + \alpha_{\text{CoC}_6\text{H}_6\text{O}_4} + \alpha_{\text{CoC}_6\text{H}_4\text{O}_4} = 1 \\
&\alpha_{\text{H}_2} + \alpha_{\text{CO}} = p = r\alpha_{\text{CoO}_r}, \quad \alpha_{\text{H}_2}/\alpha_{\text{CO}} = \beta \\
&\alpha_{\text{H}_2} + \alpha_{\text{H}_2\text{O}} = 1, \quad \alpha_{\text{CO}} + 1.64\alpha_{\text{C}_3\text{H}_4\text{O}_2} = \alpha
\end{aligned}
\tag{8.32}$$

Here $\alpha_{\text{CO}_2}, \alpha_{\text{H}_2} + \alpha_{\text{CO}} = p$, $\alpha = 1/44(\Delta m/n_0 - 18 + 16p) - \alpha_{\text{CO}_2}$ is the experimentally determined values (Δm is sample weight loss; n_0 is number of moles of (8.18) in the sample before the experiment).

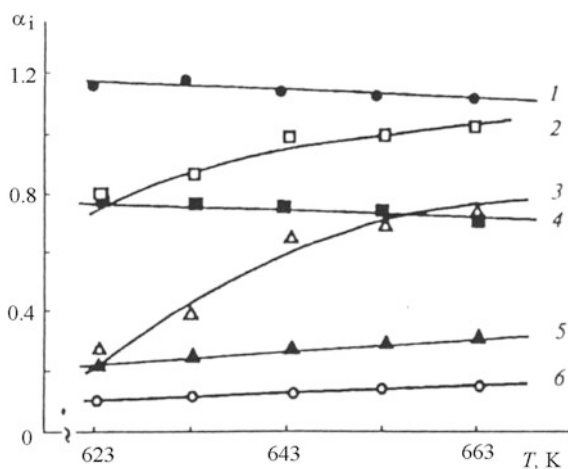
Assuming that $\alpha_{\text{C}_6\text{H}_8\text{O}_4} = 0$, $\beta = 2$ (according to mass spectrometric determination) the transformation products yield was calculated and various variants for the PPR were analyzed. Experimental data satisfies the polymer composition $(\text{CoC}_6\text{H}_6\text{O}_4)_{p-x}(\text{C}_4\text{H}_6)_x(\text{C}_4\text{H}_4)_y$.

At higher temperatures (Fig. 8.26) values $\alpha_{\text{CO}_2}, \alpha_{\text{H}_2\text{O}}$ are somewhat reduced and $\alpha_{\text{CO}}, \alpha_{\text{H}_2}, \alpha_{\text{C}_3\text{H}_4\text{O}_2}$ and α_{CoO_r} increase, and $\alpha_{\text{C}_3\text{H}_4\text{O}_2}$ increases strongly enough:

$$\alpha_{\text{C}_3\text{H}_4\text{O}_2} = 2.5 \cdot 10^8 \exp[-100/(RT)].$$

The ratio of $[\text{O}]:[\text{Co}] = r$ does not depend on T_{therm} and is equal 0.43 ± 0.03 , which corresponds to a mixture of a metal and its oxide ($\text{Co} + \lambda\text{CoO}$), where λ is 0.75, 0.20, 0.16 for CoO , Co_2O_3 , and Co_3O_4 , respectively.

Fig. 8.26 Product yield at the decomposition end of CoAcr_2 : 1— α_{CO_2} ; 2— α_{CoO_r} ; 3— $\alpha_{\text{CH}_2\text{CHCOOH}}$; 4— $\alpha_{\text{H}_2\text{O}}$; 5— α_{H_2} ; 6— α_{CO}



The main CO₂ source during CoAc₂ decomposition apparently are decarboxylation processes, while additional reactions associated with the appearance of C₂H₄ and CO₂ [reactions (8.20) and (8.23)] occur in the CuAc₂ decomposition.

Absence of PAA fragments in PPr indicates that the resulting AA out of the reaction zone is faster than the time to start polymerization. The presence in PPr composition of C₄H₄ fragments that arise by decarboxylation of CoC₆H₆O₄ fragments apparently, as in the case of other tested carboxylates indicates a low thermal stability of the metal carboxylate units. Ratio of CoC₆H₆O₄, C₄H₆ and C₄H₄ fragments in PPr depends on T_{therm} (Table 8.12).

It is noteworthy that with increasing T_{therm}:

- The total yield of PPr ($\alpha_{\text{III}} = \alpha_{\text{CoC}_6\text{H}_6\text{O}_4} + \alpha_{\text{C}_4\text{H}_6} + \alpha_{\text{C}_4\text{H}_4}$) falls $\alpha_{\text{PPr}} = 1.9 \cdot 10^{-3} \exp[34/(RT)]$;
- The yield $\alpha_{\text{CoC}_6\text{H}_6\text{O}_4}$, $\alpha_{\text{C}_4\text{H}_6}$ decreases and $\alpha_{\text{C}_4\text{H}_4}$ increases;
- The ratio $\omega = p/y$ decreases and $\alpha_{\text{C}_4\text{H}_6}/\alpha_{\text{CoC}_6\text{H}_6\text{O}_4} = \gamma$ increases

$$\omega = 4.7 \times 10^{-16} \exp[192/(RT)]$$

$$\gamma = 7.1 \times 10^{19} \exp[-238/(RT)]$$

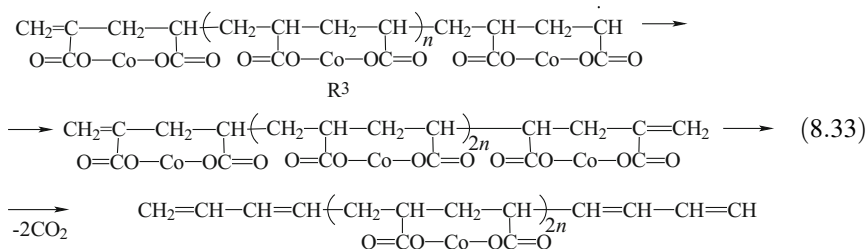
Given that the CoC₆H₄O₄ fragments (after C₄H₄ decarboxylation) short polymer chains, ω fall may indicate a reduction in the length of the Co-polyacrylate chains in PPr with increasing T_{therm}. While CoC₆H₄O₄ fragments decarboxylate at T_{therm} < 623 K CoC₆H₆O₄ fragments at 623 K is still quite stable (their proportion is ~30%), but even at 663 K, they are practically absent in PPr (<4%). Match the effective activation energy of the rate constants of gassing and the activation parameter of the temperature dependence $\gamma(T)$ ($E_a = 238.3 \text{ kJ mol}^{-1}$) indicates that the decarboxylation reaction of polyacrylate fragments (CoC₆H₄O₄) is the rate-limiting stage in gassing process.

Table 8.12 The composition of PPr (CoC₆H₆O₄)_{p-x}(C₄H₆)_x(C₄H₄)_y at various T_{therm}

PPr composition	623 K	633 K	643 K	653 K	663 K
$\alpha_{\text{CoC}_6\text{H}_6\text{O}_4} = p - x$	0.22 (0.26)	0.16 (0.20)	0.03 (0.04)	0.02 (0.03)	0.01 (0.02)
$\alpha_{\text{C}_4\text{H}_6} = x$	0.51 (0.59)	0.45 (0.56)	0.31 (0.46)	0.28 (0.46)	0.26 (0.41)
$\alpha_{\text{C}_4\text{H}_4} = y$	0.13 (0.15)	0.19 (0.24)	0.33 (0.49)	0.31 (0.51)	0.36 (0.57)
$\alpha_{\text{CoC}_6\text{H}_6\text{O}_4} + \alpha_{\text{C}_4\text{H}_6} = p$	0.73 (0.85)	0.61 (0.76)	0.34 (0.50)	0.30 (0.49)	0.27 (0.43)
$\alpha_{\text{CoC}_6\text{H}_6\text{O}_4} + \alpha_{\text{C}_4\text{H}_6} + \alpha_{\text{C}_4\text{H}_4}$	0.86	0.80	0.67	0.61	0.63
$\alpha_{\text{C}_4\text{H}_6}/\alpha_{\text{CoC}_6\text{H}_6\text{O}_4} = \gamma$	2.32	2.81	10.3	14.0	26.0

Note In parenthesis is given the proportion of fragment in the overall composition of the PPr

As part of the proposed transformation scheme appearance of $(C_2H_2)_2$ (or C_4H_4) fragments is possible only through polymer radicals R^3 recombination, formed from R^1 radical to form PPr and subsequent decarboxylation.



Assuming that the formed radicals R^3 are highly reactive, it can make the assumption that during the CoAcr_2 transformation the kinetic equilibrium concentration of growing radicals are installed in the reaction zone, and the number of recombining radicals R^3 at the transformation end is close to the number of formed AA. As a result, the value of ω is the ratio of the growth rate of the polymer radical (W_p) to the PPr formation rate (R^3 recombination rate). Therefore, $W_p \approx W_{\text{PPr}} \approx k_{\text{PPr}}\omega[R^3]^2 \approx k_{\text{PPr}}\omega\alpha_{\text{CH}_2\text{CHCOOH}}^2 = 0.26 \times 10^2 \exp[-8/(RT)] \cdot k_{\text{PPr}}$, where k_{PPr} is rate constant of radical R^3 recombination. AA yield is equal to the ratio of the AA formation rate and CoAcr_2 spending rate:

$$\alpha_{\text{CH}_2\text{CHCOOH}} = \frac{W_{\text{CH}_2\text{CHCOOH}}}{W_0 + W_{\text{CH}_2\text{CHCOOH}} + W_p} \approx \frac{W_0}{W_0 + W_p}, \quad (8.34)$$

where W_0 is the rate of radical $\text{CH}_2=\text{CHCOO}^\cdot$ formation.

Assuming $W_p \gg W_0$, we get

$$\alpha_{\text{CH}_2\text{CHCOOH}} - \frac{W_p}{W_0} \text{ и } W_0 \approx \alpha_{\text{CH}_2\text{CHCOOH}} \quad W_p \approx 6.5 \times 10^9 \exp[-109/(RT)] \cdot k_{\text{PPr}} = 6.5 \times 10^9 \exp[-(E_a + 109)/(RT)] \cdot k_{\text{PPr}}^0.$$

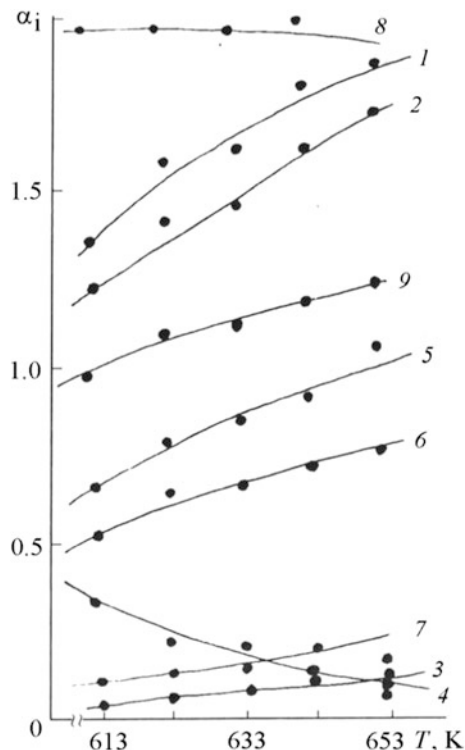
The effective activation energy of radical $\text{CH}_2=\text{CHCOO}^\cdot$ formation $E_a \geq 109.0 \text{ kJ mol}^{-1}$. Thus, by increasing T_{therm} the proportion of monomer molecules CoAcr_2 , directly exposed to thermal decomposition increases with the part of them which is involved in the polymerization process. Composition of PPr and its evolution at higher temperatures indicate that the terminal metal carboxylate groups are considerably more subjected to decarboxylation than $\text{CoC}_6\text{H}_6\text{O}_4$ fragments.

Similar product yields depending at the gassing end at different T_{therm} and during the transformation is observed in the case and other carboxylates (Figs. 8.27 and 8.28) [221, 222].

Analysis of experimental data and calculation results show the following:

- (i) Polymerization and accordingly $\text{CH}_2=\text{CHCOOH}$ and $\text{HOOCCH}=\text{CHCOOH}$ formation proceed significantly at lower temperatures than the characteristic

Fig. 8.27 The dependence of the product yield at the transformation end of CoMal from at $T_{\text{therm}}(\text{m}_0/\text{V}) \cdot 10^3 = 2.04 \text{ g cm}^{-3}$:
 1— $\alpha \sum f$, 2— $\alpha \text{CO}_2 f$, 3— $\alpha \text{H}_2 f$, $\alpha \text{CO} f$, 4— α
 ($=\text{CHCOO}$) $_2 f$, 5— 10α
 ($=\text{CHCOOH}$) $_2 f \approx 10\alpha$
 ($\equiv\text{C}-$) $_2 f$, 6— $\alpha(=\text{CH}-)_2 f$,
 7— $\alpha \text{CoO} f$, 8— $\alpha \text{H}_2 \text{O} f$,
 9— $(\Delta m/\pi O) \cdot 10^{-2}$



of main gassing. In the latter case, most of the condensable at T_{room} products appears in the early stages of transformation (warm-up period in the sample).

- (ii) The formation of radicals ($\text{CH}_2=\text{CHCOO}^\cdot$, $^\cdot\text{OCOCH}=\text{CHCOO}$) resulting in polymerization initiation depends on the thermal stability of the M—O bond in desolvated monomer. For example, studies of thermolysis of cocrystalizates FeCoAcr and Fe_2CoAcr showed that the main role in initiating the copolymerization process play radicals $\text{CH}_2=\text{CHCOO}^\cdot$, formed from Fe-containing cluster monomer, which is less thermally stable than the Co-containing monomer. In this system at high T_{therm} the elimination of two $\text{CH}_2=\text{CHCOO}$ -radicals per dehydrated $[\text{Fe}_3\text{O}(\text{CH}_2=\text{CHCOO})_6](\text{OH})$ molecule is possible.
- (iii) Decarboxylation is key reaction in the gassing process. Thus metal carboxylate H-depleted end groups are significantly more susceptible to decarboxylation than the corresponding intrachain ones. This is consistent with the concept of increased energy saturation of the end groups of long-chain polymers [232]. Thus, during CuAcr_2 , CoAcr_2 , CoMal thermolysis decomposition of end metal carboxylate groups already takes place during the warm-up tested sample and the decarboxylation degree of intrachain metal carboxylate groups at the gassing end depends on the temperature and only at high T_{therm} elimination of CO_2 is achieved almost completely. The pattern is

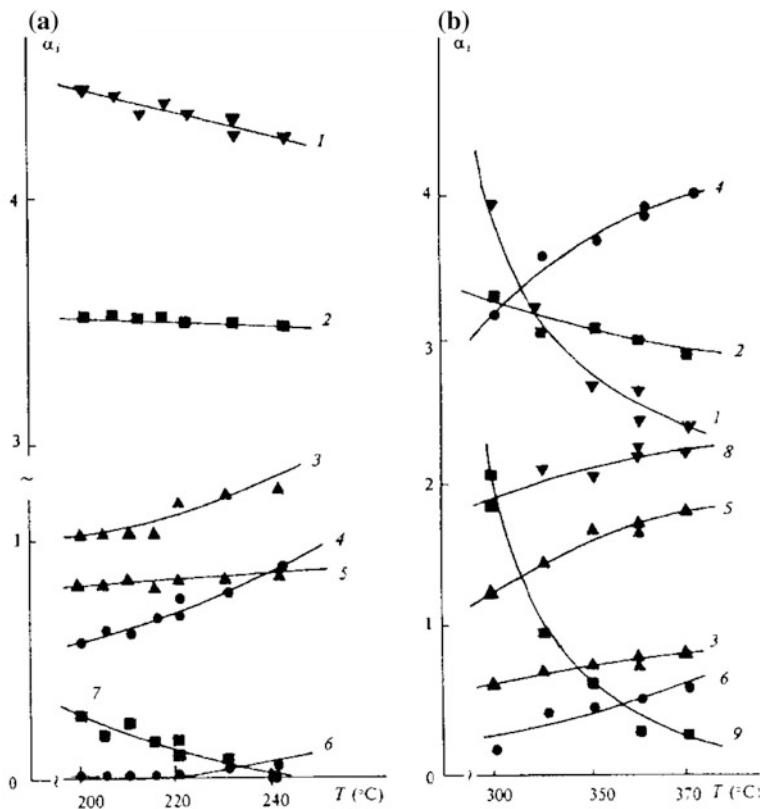


Fig. 8.28 The yield of the products of FeAcAc decomposition at 200–240 °C (a) and 330–370 °C (b): $\alpha\text{CH}_2=\text{CH} + \alpha\text{CH}_2\text{CH}$ (1); $\alpha\text{H}_2\text{O}$ (2); $2z(a)$, $z(b)$ (3); αCO_2 (4); $\alpha\text{CH}_2=\text{CHCOOH} = \alpha\text{CHCHCOO} + \alpha\text{CHCH}$ (5); αH_2 (6); $\alpha\text{CH}_2\text{CH}$ (8); $\alpha\text{CH}_2\text{CHCOO}$ (9)

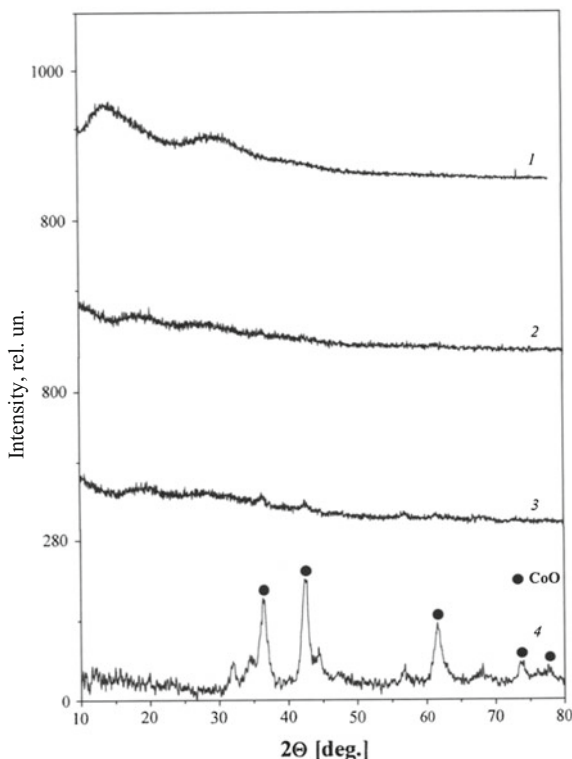
very significant for FeAcAc thermolysis. The decomposition of the terminal carboxylate groups is a major contributor to gassing at low temperatures (see Fig. 8.28a) on the background of the thermal stability of the respective intrachain groups that decompose at high temperatures (see Fig. 8.28b).

- (iv) In the copolymers based on FeCoAcAc and Fe₂CoAcAc, unlike enhanced thermal stability of CoAcAc₂ compared to FeAcAc₃ intrachain and terminal Co-containing carboxylate fragments are thermally less stable than the corresponding Fe-containing ones to elimination of CH₂=CHCOO-radical.
- (v) The ratio γ equals to amount of metal carboxylate groups in the polymer chain, including decarboxylated groups, to the number of terminal groups at the gassing end [$\gamma = (\alpha_{\text{CH}_2\text{CHCOO}} + \alpha_{\text{CH}_2\text{CH}})/(\alpha_{\text{CHCHCOO}} + \alpha_{\text{CHCH}})$ for acrylates, and $\gamma = (\alpha_{(=\text{CHCOO})_2} + \alpha_{(=\text{CH})_2})/(\alpha_{(=\text{CCOO})_2} + \alpha_{(=\text{C})_2})$ for malates] reduced with increasing T_{therm} . Thus, the γ value level is in the range 5.75 (473 K) ÷ 5.0 (513 K), and 2.64 (603 K) ÷ 1.4 (643) for FeAcAc₃,

- respectively, in the high temperature and low temperature areas; 12.9 (613 K) \div 9.2 (653 K) for CoMal. In the case of Fe–Co-cocrystallizates under the same $T_{\text{therm}} = 613\text{--}663\text{ K}$ the γ value level is slightly higher values than FeAc₃ and CoAc₂, and $\gamma = 7.7 \div 5.0$ (FeCoAc); $5.5 \div 3.8$ (Fe₂CoAc). Value 2γ can characterize the effective length of the formed polymer chain, and its variation with increasing T_{therm} indicates a change in ratio of elimination rate and reaction zone of thermoinitiated radical ($\text{CH}_2=\text{CHC}(\text{O})\text{O}\cdot$, $\cdot\text{OC}(\text{O})\text{CH}=\text{CHC}(\text{O})\text{O}\cdot$) and radical polymerization rate. Most strongly it manifests itself at the thermal transformation of CuAc₂ and CoAc₂, for which γ decrease is also observed with the growth of T_{therm} . However for CoAc₂ at $T_{\text{therm}} > 643\text{ K}$, and for CuAc₂ over the studied T_{therm} range value of $\gamma < 1$. This is probably due to the high concentration of the radicals initiating polymerization in the transformation zone, in particular, with the competition of polymerization initiation process and radical recombination with subsequent decarboxylation of recombination products.
- (vi) The composition of the metal-containing phase in solid transformation products of metal carboxylates at the gassing end depends on T_{therm} . With increasing temperature, the proportion of metal oxide phase increases, which is associated with an increase in the oxidation rate of the reactions (8.17) and (8.18), and is accompanied by an increase in the yield of CO and H₂. In the case of CuAc₂ a Cu formed at low temperatures, but at $T_{\text{therm}} > 503\text{ K}$ copper oxides ($z \leq 0.05$) appear. After CoAc₂ thermolysis value z is equal to 0.43 ± 0.03 , which corresponds to the composition $0.25\text{Co} + 0.75\text{CoO}$ (Fig. 8.29). The proportion of the oxide phase in CoMal at the thermolysis end is less than 15.0 mol% of the total metal content in the starting compound. During FeAc₃ thermolysis metal-containing products are a mixture of Fe + FeO_z: at T_{therm} over the entire range in the high-temperature region (see Fig. 8.28) $0 < z < 1$. Assuming $\text{FeO}_z \equiv \text{Fe}_3\text{O}_4$ $\alpha_{\text{Fe}_3\text{O}_4}$ value is close to the values of the Fe atom content in the Fe₃O₄ (Fig. 8.30) determined by measuring the specific magnetization of solid phase products. The z value in MO_z in thermolysis products of FeCoAc and Fe₂CoAc (where $M = \text{Fe}_{1-a}\text{Co}_a$) also increases with T_{therm} . At the same time the ferrite yield $\alpha_{\text{CoFe}_2\text{O}_4} < 1$, which is below the maximum expected for FeCoAc and Fe₂CoAc (Fig. 8.31). At that CoFe₂O₄ formation occurs only in the final stages of the thermal transformation during the decarboxylation of Fe-containing carboxylate groups, as evidenced by the dynamics of change in the magnetic characteristics of solid-state products: strong increase of χ_{σ} , σ_s , H_C due to the appearance CoFe₂O₄ phase at the thermolysis.

Thus, thermolysis of unsaturated metal carboxylates and the study of the properties of the products points to the first example of combining nanoparticle synthesis with simultaneous their stabilization by the resulting decarboxylated matrix of controlled thickness («one-pot» process).

Fig. 8.29 X-ray diffraction patterns of CoAc_2 (1) and the thermolysis products at 643 K and different depths conversion: $\Delta m = 17.5\%$ (2) 26.2% (3) 48.6% (4)



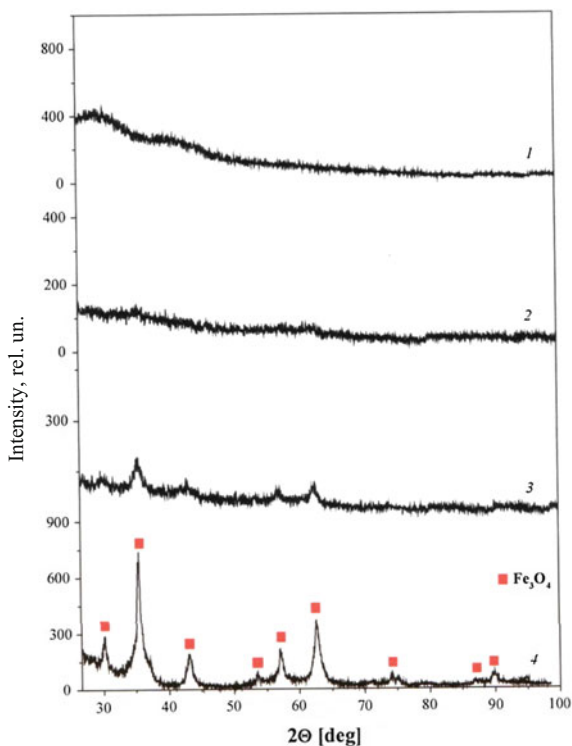
8.4 Thermolysis of Polymeric Metal Chelates

Recently polymeric metal chelates have become widely used as templates for a variety of nanomaterials [16, 233]. Unlike other templates they produce monodisperse nanoparticles of high quality, while maintaining the porosity and morphology of the template precursor. Especially PMC widely used for the preparation of metal, metal oxide and carbon nanomaterials.

Thermolytic transformations of polymeric metal chelates are very diverse [234–243]. In particular, thermolysis of polymeric copper chelates based on polyacrylamidoxime fibers [244] proceeds through the three temperatures separated stages: at 398–603 K (14.3% mass loss), 603–715 K (10.8%), and 715–965 K (68.6%). The main weight loss occurs at the final transformation stage, which is somewhat lower than in the case of the original polymer. Apparently, the copper ions have a catalytic effect on the polymer degradation, which rate increases with increasing copper ion content.

In the case of matrices having «active» to the complexing groups by reacting MX_n [9] ($\text{M}=\text{Cu}(\text{II}), \text{Ni}(\text{II}), \text{Co}(\text{II}), \text{Zn}(\text{II}), \text{Mn}(\text{II}), \text{VO}(\text{II}), \text{UO}(\text{II}), \text{Zr}(\text{IV}), \text{Ti}(\text{IV}))$) with the amino, hydroxyamino- and hydroxyl-groups, corresponding complexes are

Fig. 8.30 X-ray diffraction patterns of FeAc_3 (1) and the thermolysis products at 663 K and different depths conversion: $\Delta m = 27.4\%$ (2) 33.3% (3) 55.5% (4)



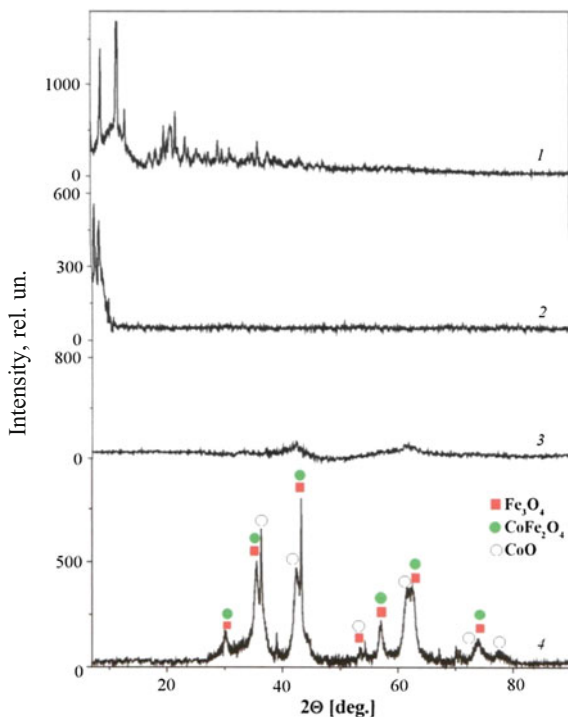
formed. The thermal stability of metal chelates falls in the number of $\text{Ni} > \text{Zn} > \text{Mn} > \text{Co} > \text{Cu} > \text{Ti} > \text{UO} > \text{Zr} > \text{VO}$, and the original polymers have the highest thermal stability. This is also the case for a number of diaminoalkane copolymers with Schiff base of 5,5'-methylene-bis(3-bromosalicylaldehyde) [245, 246].

Thermal behavior (473–1073 K) of polymeric Cu(II) and Co(II) chelates with poly (N-phenylmaleimide-co-AA) was studied by varying the comonomer ratio and different methods of metal binding [247]. Increasing N-phenylmaleimide units in copolymer chain increases the macrocomplex T_g and thermal stability, however, this increase is not as significant as one might expect (optimally from 623 to 646 K, and for some of the copolymer compositions even decreasing to 488 K).

Of interest is kinetic regularities of thermolysis of polymeric Co(II) , Ni(II) and Cu(II) chelates based on oligo-2-[(4-bromophenylimino)methyl]phenol (OBPIMP) [248]. Thermodynamic and kinetic parameters of the decomposition of such systems, calculated by Coats-Redfern equation presented in Table 8.13. The values of the apparent activation energy of thermal decomposition of oligomer metal complexes vary among $\text{OBPIMP-Cu} > \text{OBPIMP-Ni} > \text{OBPIMP-Co}$.

As a typical example, we note the strategy of using MOF thermolysis for the preparation of metal and metal oxides nano-sized particles, such as Cu/CuO , $\text{Co/Co}_3\text{O}_4$, ZnO , Mn_2O_3 , MgO and CdS/CdO [233]. According to this strategy, during

Fig. 8.31 X-ray diffraction patterns of Fe_2CoAcr (1) and the thermolysis products at 643 K and different depths conversion: $\Delta m = 25.1\%$ (2) 37.3% (3) 42.0% (4)



thermolysis in N_2 metals with a reduction potential of -0.27 V or higher contained in MOFs always form pure metal nano-sized particles, whereas metals with a reduction potential lower than -0.27 V form metal oxide nano-sized particles (Fig. 8.32). It is important that there is a relationship between the size of the formed nanoparticle and the distance between the SBU inside the MOF precursors. Besides, the crystallinity of the carbon matrix was also influenced by the thermolysis conditions (N_2 and air).

8.4.1 Synthesis of Carbon Materials

Interest in various forms and allotropic modifications of carbon is very wide from use as adsorbents [249], carriers for catalysts [250] and drug delivery [251] to the electrode materials [252]. The highly porous carbon materials may be prepared by various methods, including physical and chemical activation of the carbon, polymer aerogels carbonization and templating methods using zeolites and mesoporous silica [253–256]. Often, however, obtained mesoporous carbon materials are characterized

Table 8.13 Thermodynamic and kinetic parameters of thermal decomposition of OBPIIMP-chelates

Compound	Stage ^a	n	E _a (kJ mol ⁻¹)	ln A (c ⁻¹)	ΔS* (kJ mol ⁻¹)	ΔH* (kJ mol ⁻¹)	ΔG* (kJ mol ⁻¹)
OBPIIMP	I (180–308 °C)	0.9	96.31	19.53	-87.52	91.76	139.6
	I (202–317 °C)	0.2	39.84	5.81	-201.6	35.31	145.0
OBPIIMP-Co	II (353–724 °C)	0.9	31.34	0.693	-248.4	23.75	250.3
	I (229–353 °C)	0.5	100.2	18.16	-99.75	95.29	155.2
OBPIIMP-Cu	II (353–724 °C)	1.0	65.36	6.33	-201.3	57.96	235.5
	I (257–383 °C)	0.8	62.04	6.48	-197.3	56.76	181.9
OBPIIMP-Ni	II (383–626 °C)	0.4	48.81	6.82	-195.7	42.65	187.5

^aI and II are the temperature regions of initial and 50% weight loss

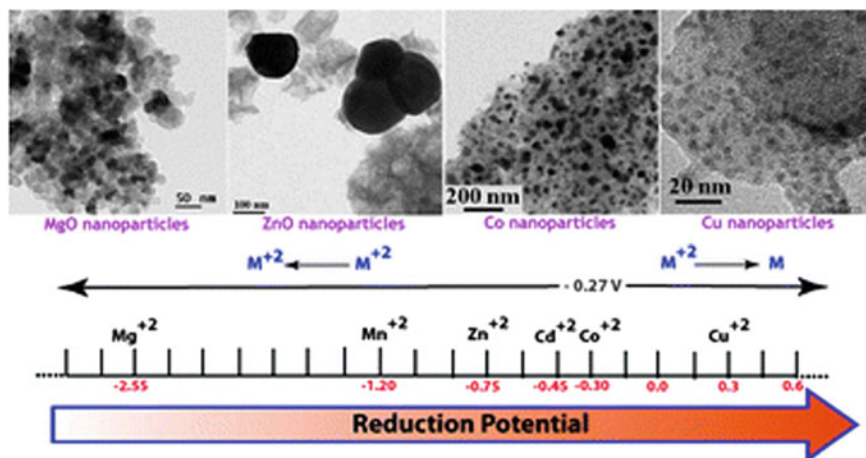


Fig. 8.32 Relation between the formed nanoparticle size and reduction potential

by a broad polydispersity to micron-sized particle and their fuzzy shape. Such materials have certain restrictions on the use, for example, in biomedical applications.

The direct thermal transformation of PMC, in particular MOFs or CPs, is an effective method for producing carbon materials, the hallmarks of which, as was first shown in [257] are ultra-developed specific surface area, ultra-high volume and controlled pore structure. This method was used for the preparation of porous carbons with special morphologies (for example, cube and polyhedron etc.) [258–260], and their pore structures may be easily varied depending on the as-formed metal or metal oxide nano-sized particles. However, using thermolysis of MOFs and CPs for the preparation of nanocomposites is restrained by their high cost [258, 261].

Carbon materials can be prepared by a «direct carbonization» of PMC without additional introduction of other carbon precursors [262–264], or in the presence of a carbon precursor such as furfuryl alcohol [257, 265, 266], a phenolic resin, carbon tetrachloride or ethylene diamine [267]. Zn- or Al-based MOFs are used most widely as a template MOFs. The synthetic protocol using additional carbon precursor includes its impregnation and subsequent polymerization within the MOFs micropores. During thermal carbonization porous carbon network formation and MOFs decomposition takes place simultaneously, i.e. MOFs is also the sacrificial template and secondary carbon precursor. The carbonization product is thoroughly washed with acid solution to remove metal nanoparticles, or a metal is evaporated and thus removed from the reaction system during the processes that are conducted at higher temperatures (up 1000 °C).

As an example, we consider MOF-5, which has 3D interconnected channel system with 18 Å cavities [268]. During the carbonization process at a temperature

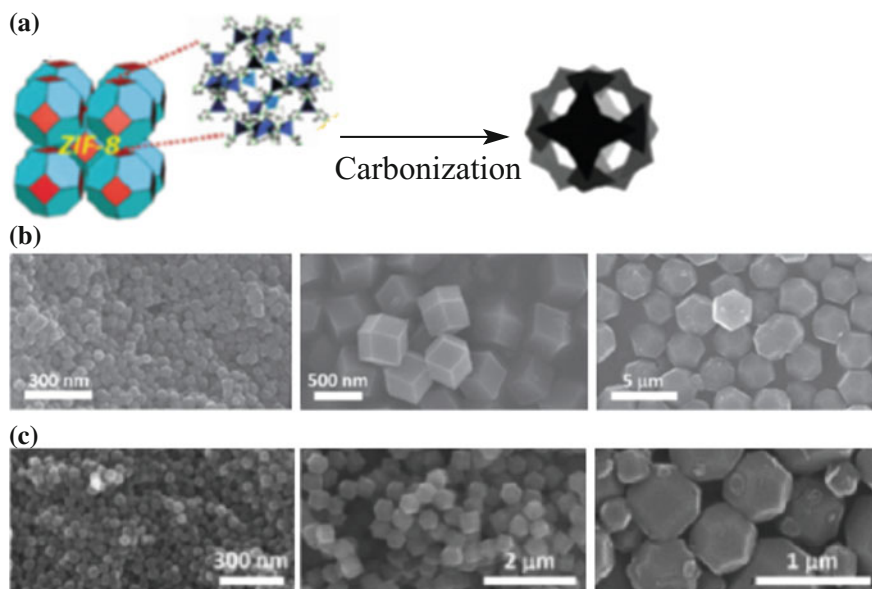


Fig. 8.33 **a** Synthesis scheme of nanoporous carbon by the direct carbonization of ZIF-8 precursor; **b** SEM micrographs of ZIF-8 crystals of various sizes; **c** SEM micrograph of nanoporous carbon of various sizes, obtained by the direct carbonization of ZIF-8

of 1000 °C under an argon stream MOF-5 is decomposed to form nanoporous carbon with a specific surface area and pore volume $2872 \text{ m}^2 \text{ g}^{-1}$ and $2.06 \text{ cm}^3 \text{ g}^{-1}$ [257]. Imidazole-based MOF ZIF-8 is zeolite-like pore structure [269]. Its crystals with different particle sizes directly carbonized at 800 °C in a one-pot process to form a nanoporous carbon [270, 271], which retains the morphology of the initial precursor (Fig. 8.33), and the adsorption-desorption N_2 isotherms of the obtained material are isotherms character typical for microporous materials (Table 8.14) [264].

Interestingly, for the ZIF-8 carbonization products obtained at the temperature range 600–1000 °C unlike nanoporous carbon-based Al-PCP [262] and MOF-5 [272] the formation of meso- and macropores are not observed (Table 8.15) [263], which, apparently, due to the structural features of the original templates.

3D framework structure of aluminum naphthalenedicarboxylate (Al-PCP) contains two types of square shaped pores, in particular, large and small channels with dimensions $7.7 \times 7.7 \text{ \AA}^2$ and $3.0 \times 3.0 \text{ \AA}^2$, respectively (Fig. 8.34) [273]. Apparently, such a structure of the coordination template in direct carbonization conditions at 800 °C promotes the formation of nanoporous carbon with extremely high surface area ($5500 \text{ m}^2 \text{ g}^{-1}$) (Fig. 8.35). But during carbonization over 900 °C specific surface area decreases up to $200 \text{ m}^2 \text{ g}^{-1}$ due to the structure collapse caused by the product graphitization. In such cases additional sources of carbon

Table 8.14 The surface area and pore volume for the initial ZIF-8 template and produced nanoporous carbon [264]

Sample	Average particle size (nm)	Surface area ($\text{m}^2 \text{g}^{-1}$)	Pore volume (cc g^{-1})
Small-size ZIF-8	50	1530	1.3
Middle-size ZIF-8	300	1570	0.9
Large-size ZIF-8	2000	1960	1.2
Small-size carbon	50	1160	1.2
Middle-size carbon	300	1390	0.8
Large-size carbon	2000	1610	1.1

Table 8.15 Surface are and pore size of carbon materials obtained by direct carbonization of ZIF-8 [263]

Sample ^a	Surface area ($\text{m}^2 \text{g}^{-1}$)		Total pore volume ($\text{cm}^3 \text{g}^{-1}$)	Micropore volume ($\text{cm}^3 \text{g}^{-1}$)		Pore diameter (\AA)
	BET method	Langmuir method		t-Plot method	NL-DFT method	
Z-600	24	28	0.05	–	–	–
Z-700	520	580	0.27	0.19	0.19	10.6
Z-800	720	810	0.37	0.26	0.26	10.6
Z-900	1075	1215	0.57	0.38	0.39	10.2, 11.7
Z-1000	1110	1250	0.62	0.39	0.40	11.7, 12.7

^aThe numbers at Z denote the carbonization temperature NL-DFT is the nonlocal density functional theory

require to preserve the porous structure in the system, such as the use of a typical carbon precursor, for example, furfuryl alcohol [274].

As can be seen, the carbonization temperature of MOFs templates complex influences the characteristics of the resulting carbon material. As noted above, MOF-5 is characterized by mesoporous structure. Curves character of adsorption-desorption isotherms indicates the presence of macropores along with a low content of micropores (Fig. 8.36) [199].

Nanoporous carbon obtained at 530 °C ($3040 \text{ m}^2 \text{g}^{-1}$) has the largest surface area, and with a further increase in temperature from 650 to 800 °C specific surface area decreased from 1521 to $1141 \text{ m}^2 \text{g}^{-1}$. But if the carbonization temperature exceeds 900–1000 °C an increase the specific surface area from 1647 to $2524 \text{ m}^2 \text{g}^{-1}$ is again observed, which may be due to evaporation of Zn vapor at temperatures above 800 °C.

Al-DTPA microfibers were used as cost-effective precursors (Fig. 8.37) to prepare nitrogen-doped carbon microfibers (NCF) [275]. In particular, thermal transformation and acid-leaching of Al-DTPA leads to the well-defined NCFs. It is important to underline that the microfiber morphology of Al-DTPA persists in the

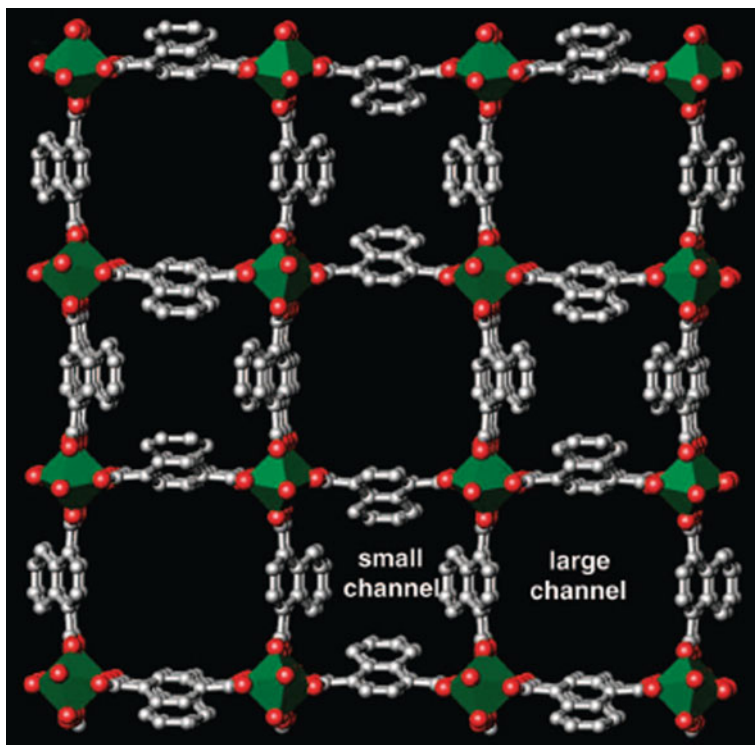


Fig. 8.34 Crystal structure of coordination polymer Al-PCP

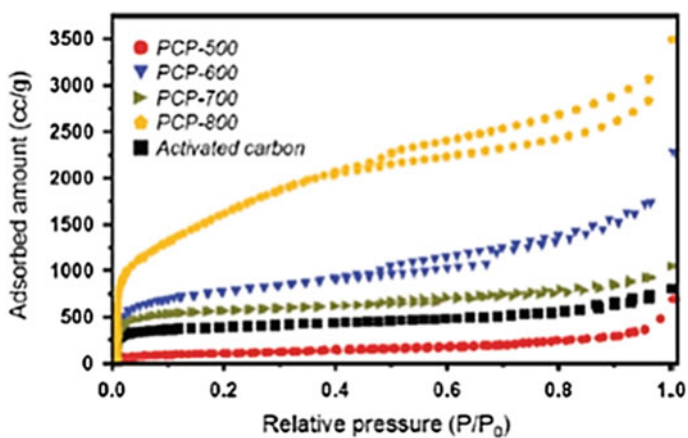


Fig. 8.35 The adsorption-desorption N_2 isotherms for carbonization products of coordination polymer Al-PCP at different temperatures

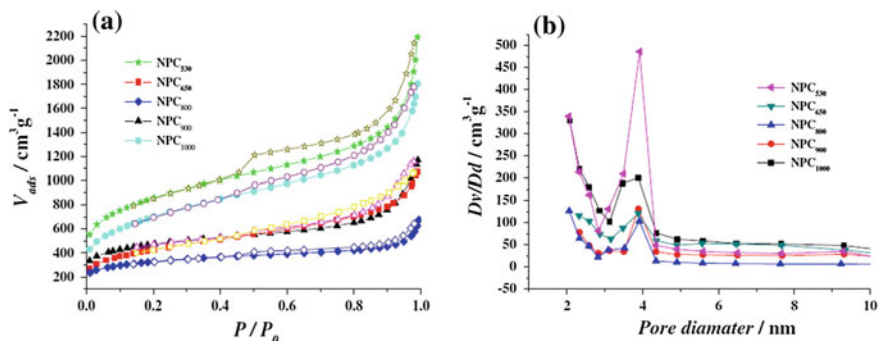
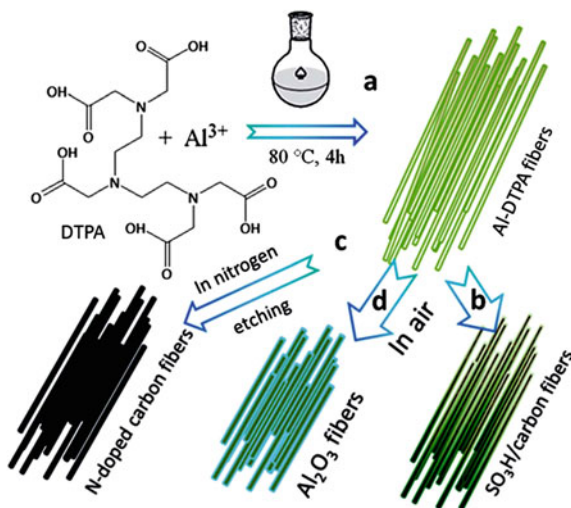


Fig. 8.36 The nitrogen adsorption-desorption isotherms (a) and pore size distribution (b) of carbonation products for MOF-5 obtained at various temperatures

Table 8.16 Textual data of NCFs obtained at 750, 900 and 1000 °C

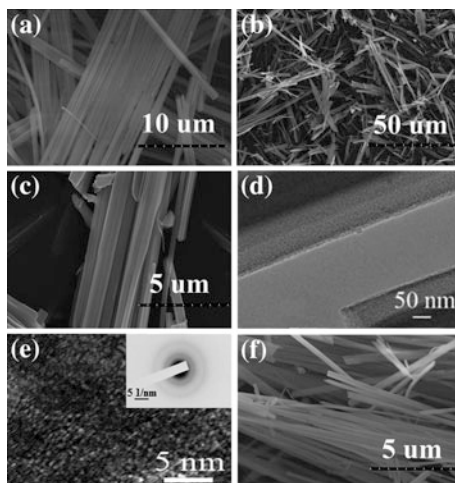
Samples	S_{BET} ($\text{cm}^2 \text{g}^{-1}$)	S_{meso} ($\text{cm}^3 \text{g}^{-1}$)	S_{micro} ($\text{cm}^3 \text{g}^{-1}$)	V_{total} ($\text{cm}^3 \text{g}^{-1}$)	$V_{\text{micro}}^{\text{T}}$ ($\text{cm}^3 \text{g}^{-1}$)
750	604	84	520	0.39	0.28
900	933	108	825	0.58	0.43
1000	1072	67	1005	0.65	0.55

Fig. 8.37 Schematic illustration of the formation process of the nanoporous N-doped carbon microfibrils and solid acids microfibrils



resulting carbon materials (Fig. 8.38b–e). The typical NCFs prepared at 900 °C (NCF-900) have the diameters of ~ 500 nm and lengths of about 50 mm (Fig. 8.38b–d). It should be noted that some graphitization regions are observed in

Fig. 8.38 a SEM images of Al-DTPA microfibers; b, c SEM images of NCF-900; d, e TEM images of NCF-900. Inset is the corresponding selected area electron diffraction pattern of NCF-900; f SEM images of γ -Al₂O₃ obtained by heating Al-DTPA at 800 °C in air



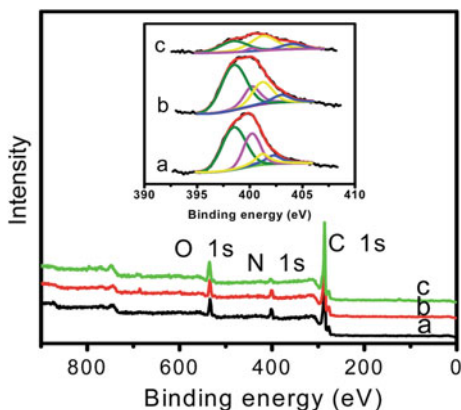
the high-resolution TEM image of NCF-900 (Fig. 8.38e). Increasing thermolysis temperature leads to a slight increase in the graphitization degree of carbon microfibers (Fig. 8.38e inset). Moreover, considerable interconnected pores are homogeneously distributed in the whole microfibers (Fig. 8.38d). The pore size distribution curves exhibited the mesopores with sizes of 2–30 nm. The total BET surface area of NCF-750, -900, and -1000 are equal to 604, 933 and 1072 m² g⁻¹, respectively (Table 8.16). Thus, the NCFs with nanoporous structure, uniform fiber morphology, and appropriate degree of graphitization were successfully obtained by thermolysis of Al-DTPA.

It should be noted that Al-DTPA microfibers can be also used as the precursors of γ -Al₂O₃ microfibers. After thermolysis of Al-DTPA in air at 800 °C, the well-defined microfiber morphology in γ -Al₂O₃ was observed in SEM images (Fig. 8.38f). As compared to Al-DTPA microfibers, there is decreasing the diameter (350 nm) and length (50 mm) (Fig. 8.38a). The prepared γ -Al₂O₃ has a smaller BET surface area (50 m² g⁻¹) and pore size distribution in the range of 2–15 nm.

It should be noted high contents of doped nitrogen atoms in the resulted NCFs. The N peaks at 398.3, 400.3, 401.2, and 403.6 eV in the deconvoluted N 1s XPS spectra (Fig. 8.39) corresponds to pyridinic, pyrrolic, graphitic and oxidized type of nitrogen atoms, respectively (Fig. 8.39 inset). Dominant nitrogen types in NCF-900 are the pyridinic- and graphitic-like nitrogen atoms.

Thus, various types of porous carbon materials may be prepared in a simple manner, based on the MOF structures as template molecules and a carbon source. Due to the high thermal stability, the nanoporous structure and the possibility to penetrate into the pores of small molecules with their subsequent participation in different «ship-in-bottle» reactions, MOFs can be considered as rigid templates similar to the mesoporous silica gel and zeolites [276–278]. Given the wide variety of MOFs of different compositions and morphology the carbon materials can be produced with controlled pore texture and surface area. Moreover, the synthetic

Fig. 8.39 The XPS survey spectra and the deconvoluted N 1s XPS spectra (inset) of NCF-750 (a), NCF-900 (b) and NCF-1000 (c)



strategy based on MOFs allows to produce various carbon materials with catalytic [279], magnetic [280], energy storage and improved mechanical properties [281], including carbon nitrides [282].

Advantages of MOFs templates can be realized very efficiently in the production of various composite carbon materials, for example, type M/MO@C (Fig. 8.40). The general approach of the synthesis is based on the fact that the 1st stage of polymerization is carried out in MOFs carbon precursor (Fig. 8.40a), then a M@C nanocomposite is formed by thermolysis (Fig. 8.40b), and finally post-thermal treatment is carried out to convert the metal to metal oxide nanoparticles (Fig. 8.40c). The porosity of the carbon matrix and M/MO nanoparticle sizes are controlled in stages. According to the similar scheme Cu@C, Cu₂O@C or CuO@C nanocomposites from MOF HKUST-1 [283] with maintaining the octahedral morphology of the starting MOF and Zn@C, ZnO@C based on MOF-5 [284] were obtained. In the resulting material the functional nanoparticles are interconnected by nanoporous carbon matrix, the diffusion properties of which are very attractive for use of such materials as electrode materials or in heterogeneous catalysis.

It should be noted the obtaining a porous cobalt oxide-carbon hybrid by carbonizing in an inert atmosphere and subsequently air-calcining nanocrystals of ZIF-67 [285]. It is important that the synthesized carbon composite material can act as an efficient electrochemical water oxidation catalyst.

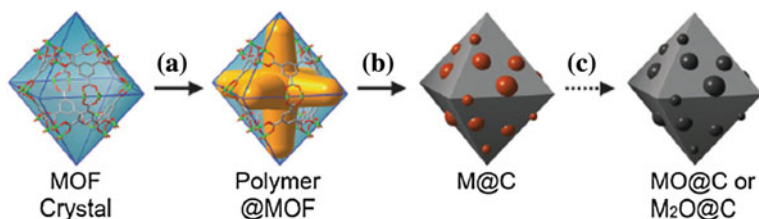


Fig. 8.40 Scheme of the transformation of MOFs in M/MO@C composite

8.4.2 The Preparation of Metal Oxide Materials

Methods for producing metal oxide nanocomposites from PMC are well developed and described in the literature (see recent review [16]). The basis of these methods is generally a single-stage solid-phase thermolysis of the precursor source, and, in general, quite comfortable, well-reproducible and easily scalable process. The methodology was used in the synthesis of nanoparticles of various metal oxides, for example, PbO [286–288], ZnO [151, 289, 290], Fe₂O₃ [291–294], Co₃O₄ [295–298], CdO [16], CuO/Cu₂O [299, 300], Ti₂O₃ [301] etc. We consider some of the most common examples.

Thus, [Pb₂(2,9-dimethyl-phen)₂(μ-N₃)₂(μ-ClO₄)₂]_n [302] and [Cd(2,9-dimethyl-phen)(TTA)₂]_n [303] were used for PbO and CdO nanoparticles preparation, respectively. Thermal decomposition of the 3D CP [Pb(phen)(1-N₃)(1-NO₃)]_n containing an azide-anion ligand gave PbO nanoparticles [304].

ZnO nanomaterials with desired morphologies have been obtained by thermal decomposition of appropriate CPs and MOF precursors [16, 53, 289, 290, 305, 306]. For example, calcination of infinite rectangular-tubular helices [ZnCl₂L] and [ZnBr₂L] (L is bis(3-pyridyl)cyclotetramethylenesilane) at 500 °C gives uniform hexagonal tubular spire crystals of 1.2 × 1.2 × 4.0 μm³ dimensions and spheres, respectively [307]. SEM images of the products of [MX₂L] thermolysis at 500 °C

Fig. 8.41 SEM images of thermal decomposition residue of [ZnCl₂L] (a) and [ZnBr₂L] (b) calcined at 500 °C for 2 h

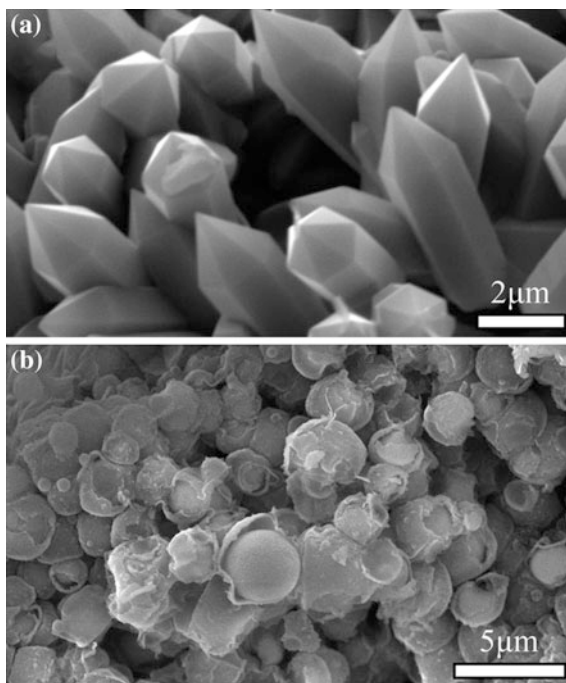


(Fig. 8.41) show that the compounds ultimately change to zinc(II) oxide crystals. For $[\text{ZnCl}_2\text{L}]_n$, calcination at 500 °C leads to the growth of each ZnO single crystal.

The Zn(II) oxide and Cd(II) oxide nanoparticles were prepared by thermolysis of Zn(II) and Cd(II) CPs, $[\text{Zn}(\text{L})_2(\text{N}_3)_2]_n$, $[\text{Zn}(\text{L})_2(\text{SCN})_2]_n$, $[\text{Cd}(\text{L})_2(\text{N}_3)_2]_n$ and $[\text{Cd}(\text{L})_2(\text{SCN})_2]_n$, where L is 2-aminomethylpyridine [308]. SEM images exhibit the average size of prepared ZnO and CdO nanoparticles of 60–70 nm. We also note the preparation of ZnO nano-sized particles using Zn-isophthalate [309] and CdO nanowires from Cd-terephthalate complexes [310].

The calcinations of nanoparticles of a 3D Cd(II) compound, $[\text{Cd}(\text{L})_2(\text{H}_2\text{O})_2]_n$ (L⁻ is 1H-1,2,4-triazole-3-carboxylate), at 650 °C under air yielded CdO nanoparticles [311].

A series of lead-containing polymeric complexes have been applied for PbO nanoparticle formation. PbO nanoparticles serve as catalyst [312] for multicomponent organic synthesis reactions, for instance Paal-Knorr reaction and oxidative coupling of methane, due to the significant catalytic property with operational simplicity, high reactivity, environmental friendliness, reduction of reaction times, and reusability of PbO nanoparticles [313]. In this respect, a CP of lead(II) nitrate complexes with bridging trans-1,2-bis(4-pyridyl) ethene (L) ligand, $[\text{Pb}(\mu\text{-NO}_3)_2(\text{L})(\text{MeOH})]_n$, was used [314] to prepare PbO nanoparticles using two different methods. Nano-structured PbI_2 and PbO were synthesized from Pb(II) metal-organic polymer, $[\text{Pb}(\mu\text{-L})(\mu\text{-I})_2]_n$, where L is pyrazine, by calcination with argon and air, respectively [315]. Different N-heterocyclic ligands with carboxyl or carboxamide groups have also been used. Thus, after calcination of nanobelts of a lead (II) CP, $[\text{Pb}(\text{L})_2]_n$, HL = 3-pyridinecarboxylic acid, at 400 °C, pure phase nano-sized lead(II) oxide was produced [316].

The nanostructure of 1D copper CP, $[\text{Cu}(\text{HL})\text{NO}_3]_n$ (H_2L is [2-[1-(2-hydroxypropylimino)ethyl] phenol]), was used as precursor to obtain single phase CuO nano-sized particles by thermolysis [317]. According to the SEM images the diameters of the prepared products were equal to 40 nm (Fig. 8.42).

Calcinations of the nano-sized copper(II) polymeric compound, $[\text{Cu}(\text{L})(\text{H}_2\text{O})_2]_n$ [L = 2,6-pyridinedicarboxylate], at 500 °C under air yielded CuO nanoparticles [318]. Oriented growth of single crystalline Cu(111) flake was reached by the thermolysis of a 1D chain-like hybrid CP $[(\text{CuBr})_2(\text{bpy})]_n$ (Fig. 8.43) [319].

After calcining, the cerium-based CPs micro/nanostructures such as nanoparticles, nanorods, and microflowers based on three isomers of benzenedicarboxylic acid at high temperature, ceria with retained morphologies were achieved [320].

Thermolysis of the porous CPs with nanorod morphology based on a catechol-substituted Pp [*meso*-tetrakis(3,4-dihydroxyphenyl)-Pp] led to carboniferous materials containing metal oxide nanoparticles with large surface areas (up to 800 m² g⁻¹) [321].

A porous indium(III) MOF, $[\text{In}_2(\text{OH})_2(\text{L})]_n \cdot 2n\text{H}_2\text{O}$ (MIL-60, L = 1,2,4,5-benzene tetracarboxylate), was used for obtaining In₂O₃ nanoparticles by thermolysis of MIL-60 at 450 °C under air [322].

The advantages of these PMC precursors are simplicity of processing and long-range ordering that allow the synthesis of metal oxides with various morphologies.

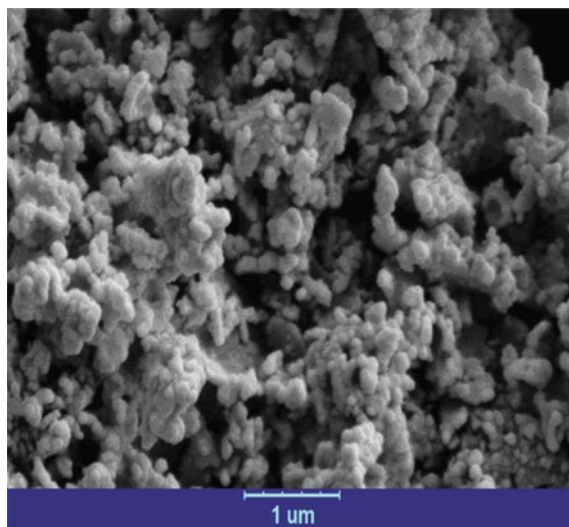


Fig. 8.42 SEM images of CuO nanoparticles prepared by direct calcination of Cu(II) CP

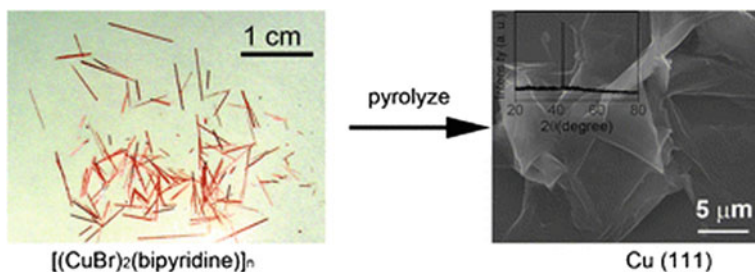


Fig. 8.43 The preparation of Cu(111) flake by pyrolysis of $[(\text{CuBr})_2(\text{bpy})]_n$ under N_2 at $750\text{ }^\circ\text{C}$

Phase composition and properties of the resulting metal oxide nanocomposites depend on the crystal structure and morphology of the starting PMC precursor, its particle size, and the synthesis conditions (the influence of the temperature, environment, the nature of the surfactant and etc.).

8.4.2.1 Influence of the Original Morphology and Particle Size of Polymeric Metal Chelates

Size and morphology of the produced nanomaterials are highly dependent on the type and morphology of the PMC precursor [16, 323–325]. Thus, hollow and non-hollow In_2O_3 particles with different morphologies may be selectively obtained

from the PMC according to their chemical composition and porosity. Hexagonal rod microparticles of the CPP-1 based on 1,4-benzenedicarboxylate and indium(III) ions during the calcination at 550 °C also form hexagonal polycrystalline particles (consisting of ~20 nm crystallites) of In_2O_3 in the form of rods whose size is about 35% less than the original precursor [326]. A similar character of morphology transformation during thermolysis is shown in another example of a coordination polymer (CPP-2) composed of In(III) and 2,6-bis[(4-carboxyanilino) carbonyl]pyridine with the particles in the form of hexagons (Fig. 8.44). As indicated, depending on the precursor decomposition mechanism the hollow and non-hollow particles of In_2O_3 can be obtained, on the basis of the CPs with hollow and non-hollow structure of the particles, respectively.

The nanorod morphology is characteristic of the thermolysis products of CP with $[\text{Zn}(4,4'\text{-bipy})\text{Cl}_2]_n$ block [327], while during the decomposition of MOF with $[\text{Zn}(\text{ox})(4,4'\text{-bipy})]_n$ block (where ox is oxalate) ZnO nanostructure formed in a radially spaced nanoneedles (Fig. 8.45), i.e. different framework structure of the initial CPs influences the final morphology of the formed ZnO nanostructures. Intermediates in forming ZnO nanorods are rod-shaped nanoparticles while intermediates of needle-like ZnO nanostructures are spherically agglomerated nanoparticles.

Porous $\gamma\text{-Fe}_2\text{O}_3$ nanoparticles were prepared via a solid-state transformation process of a mesoporous iron(III) carboxylate crystal, MIL-100(Fe) [328]. The N_2 adsorption-desorption analysis also demonstrates the mesoporous character of the derived $\gamma\text{-Fe}_2\text{O}_3$ material, with type IV N_2 isotherm at 77 K. This material has a relatively large specific surface area $123.5 \text{ m}^2 \text{ g}^{-1}$, which is presumed to be benefited from the two-step calcination of the template MIL-100(Fe). On the other hand, the pore size distribution reveals that most of the pores are focused on 10 nm, indicating the mesopores are effectively formed for the $\gamma\text{-Fe}_2\text{O}_3$.

Of interest is using MOF thermolysis to develop the porous iron oxides [257, 295, 329–333]. As an example, we note the fabrication of spindle-like mesoporous $\alpha\text{-Fe}_2\text{O}_3$ using MOF MIL-88(Fe) as template [294]. The prepared spindle-like mesoporous $\alpha\text{-Fe}_2\text{O}_3$ was composed of clustered Fe_2O_3 nanoparticles with size of <20 nm. In another example a facile synthesis of porous Fe_2O_3 nanocubes by simultaneous oxidative decomposition of Prussian blue nanocubes was demonstrated [334, 335]. The derived porous Fe_2O_3 nanocubes are composed of very fine Fe_2O_3 nanoparticles with size of several nanometers. It is important that MOFs show distinct advantages due to their well-ordered crystalline structure, high porosity, large surface area, and tunable pore size, in comparison with other templates.

It should be noted that during the MOF pyrolysis it can also be prepared metal oxide nanostructure consisting of the same primary particles, but with a different secondary and tertiary architecture thus modulating the macroscopic structure of the initial CP. For example, two types of Co_3O_4 nanomaterials with plate-like and rod-like morphology of the nanoparticles, based on the Co-containing plate-shaped $[\text{Co}_3(\text{L})_3(\text{DMF})_4]_n$, p-MOF) and rod-shaped $([\text{Co}(\text{L})(\text{DMSO})]_n$, r-MOF) coordination polymers, consisting of the same composite units (Co^{2+} and 1,4-benzenedicarboxylate (L)) (Fig. 8.46), were prepared through pseudomorphic transformation

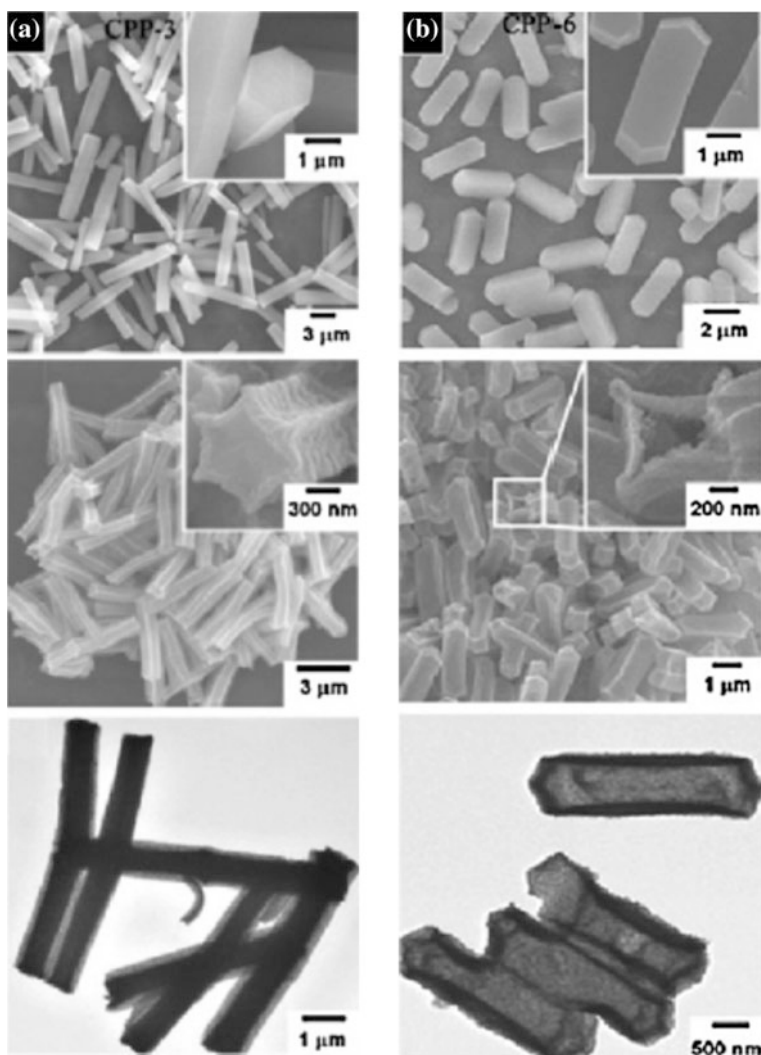


Fig. 8.44 a SEM images of (a-top) hexagonal rod-shaped precursor CPP-1, b (b-top) elongated hexagon-shaped precursor CPP-2. SEM (middle) and TEM (bottom) images of (a) non-hollow hexagonal rod-shaped In_2O_3 , (b) hollow elongated hexagon-shaped In_2O_3

[335]. ZnO nano-sized materials were prepared by thermolysis of the host and the apohost framework of $[\text{Zn}_2(\text{L})_2(\text{dabco})]\cdot 4\text{DMF}\cdot 0.5\text{H}_2\text{O}$ with the same L ligand [336]. However, ZnO microrods composed of ZnO nanoparticles were prepared by the thermolysis of fully desolvated framework of this compound. It was concluded that the role of guest DMF in obtaining ZnO nano-sized particles from the solvated

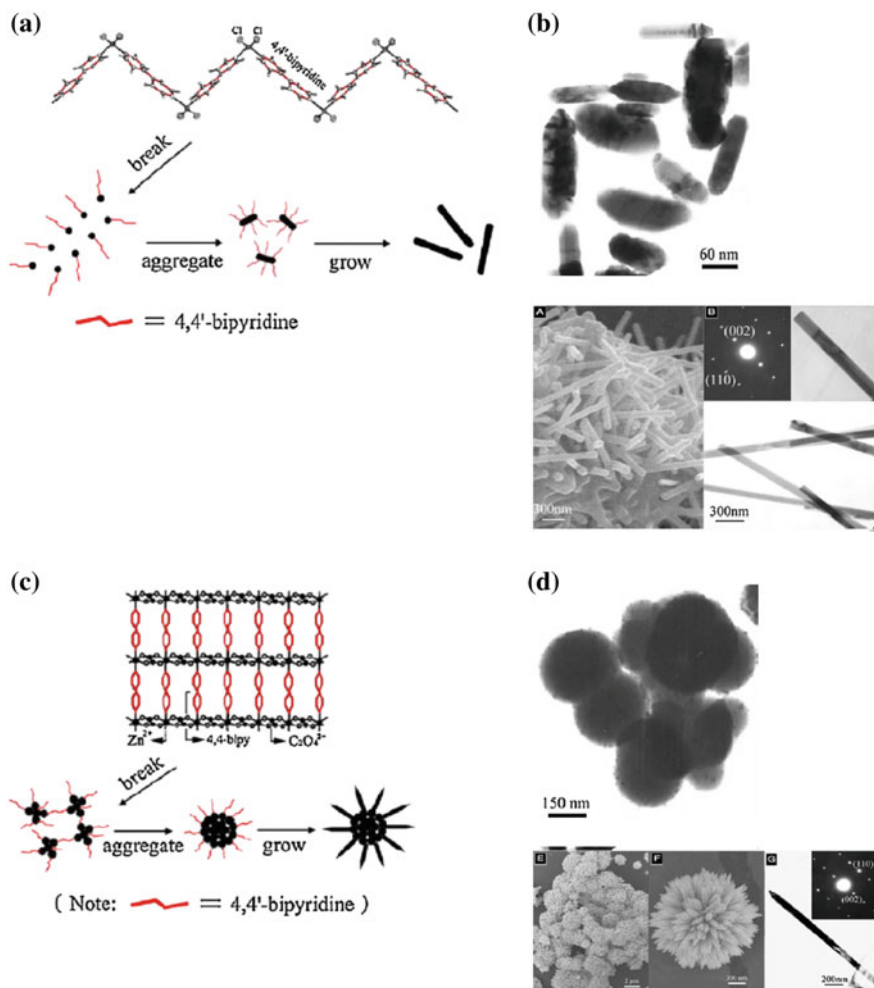


Fig. 8.45 Scheme of formation of ZnO nanorods and nanoneedles during thermolysis of $[Zn(4,4'-bipy)Cl_2]_n$ (a) and $[Zn(ox)(4,4'-bipy)]_n$ (c) and TEM (top) and SEM (bottom) micrographs of intermediate (top) and final decomposition products (bottom) of CPs $[Zn(4,4'-bipy)Cl_2]_n$ (b) and $[Zn(ox)(4,4'-bipy)]_n$ (d)

complex is similar to the role of polymer stabilizers in the formation of nano-sized particles.

Thermolysis of nano plates of two Cd(II)-based MOFs, $[Cd_2(L)_2(L')_2]_n \cdot (DMF)_x$ (TMU-8) and $[Cd(L)(4,4'-bipy)]_n \cdot (DMF)_y$ (TMU-9) where H_2L is V-shaped flexible dicarboxylate ligand 4,4'-oxybis(benzoic acid) and the L' is N-donor ligand 1,4-bis(4-pyridyl)-2,3-diaza-1,3-butadiene, leads to CdO nano-sized particles (Fig. 8.47) [337]. SEM images of the products exhibit the formation of aggregation of CdO nano-sized particle in the range of 60–160 nm. Particle sizes of CdO prepared by

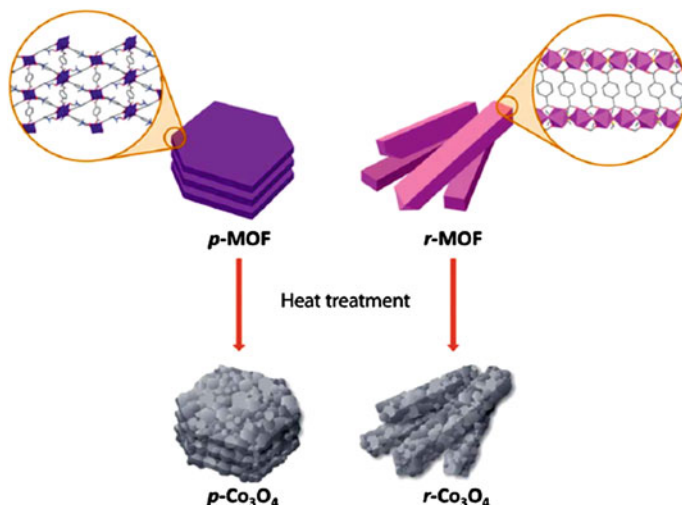


Fig. 8.46 Scheme of pseudomorphic conversion of Co-based MOFs

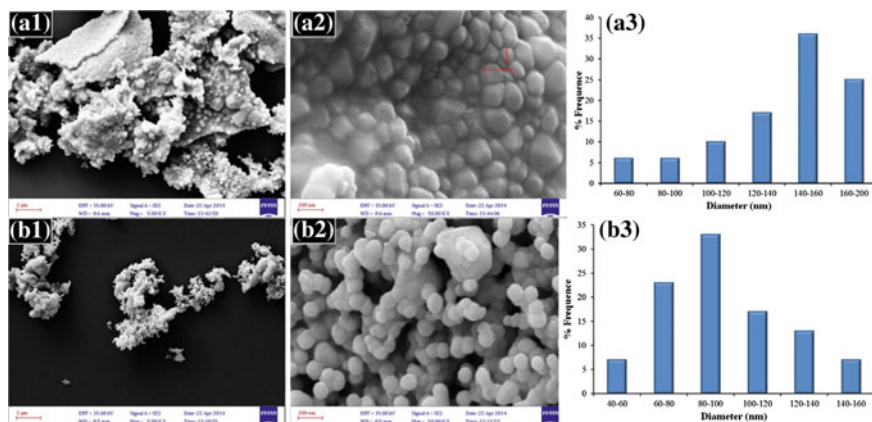


Fig. 8.47 FE-SEM images and the corresponding particle size distribution histogram of CdO nanoparticles prepared by thermolysis of **a** TMU-8 and **b** TMU-9 at 550 °C

thermolysis of TMU-9 are smaller than those prepared from calcination of TMU-8 that is associated with the influence of the structures of these two MOFs on the final morphologies of CdO particles [16].

The 1D CP, $[\text{Zn}(4,4'\text{-bpy})(\text{H}_2\text{O})_4](\text{L})\cdot 4\text{H}_2\text{O}$ (H_2L is acylenedicarboxylic acid), and 3D MOF, $\text{Zn}(\text{L})_2(\text{L}')_2$ (L' is triethylamine) were applied as precursors for the synthesis of ZnO nanocrystals via direct thermal decomposition [338]. Interestingly, changing the precursor from 1D CP to 3D MOF changes the morphology from nanorods to nanoparticles. In particular, the SEM images (Fig. 8.48) exhibited

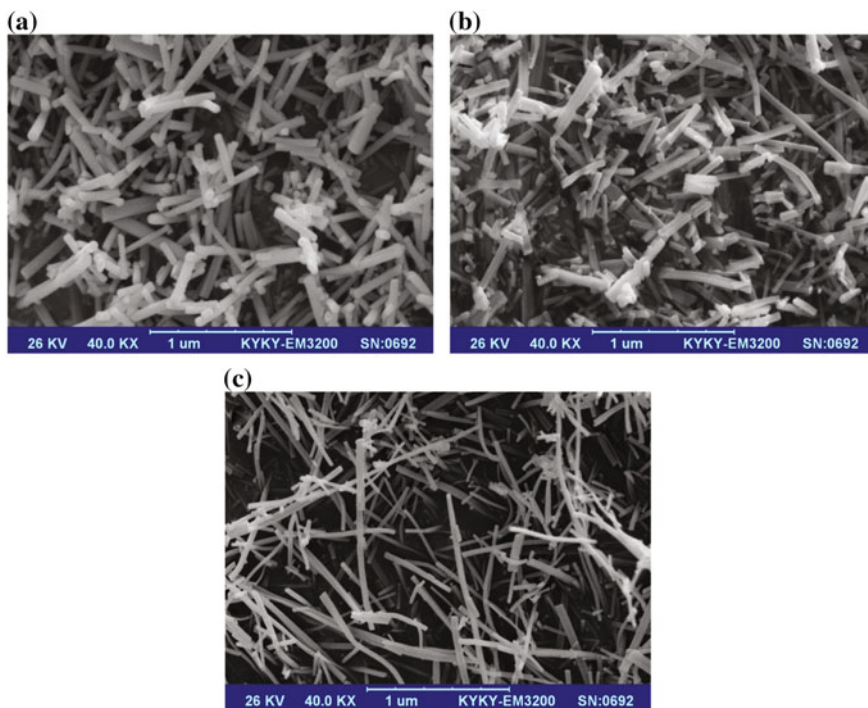


Fig. 8.48 The SEM images of ZnO nanorods obtained by annealing CP at **a** 400 **b** 500 and **c** 600 °C

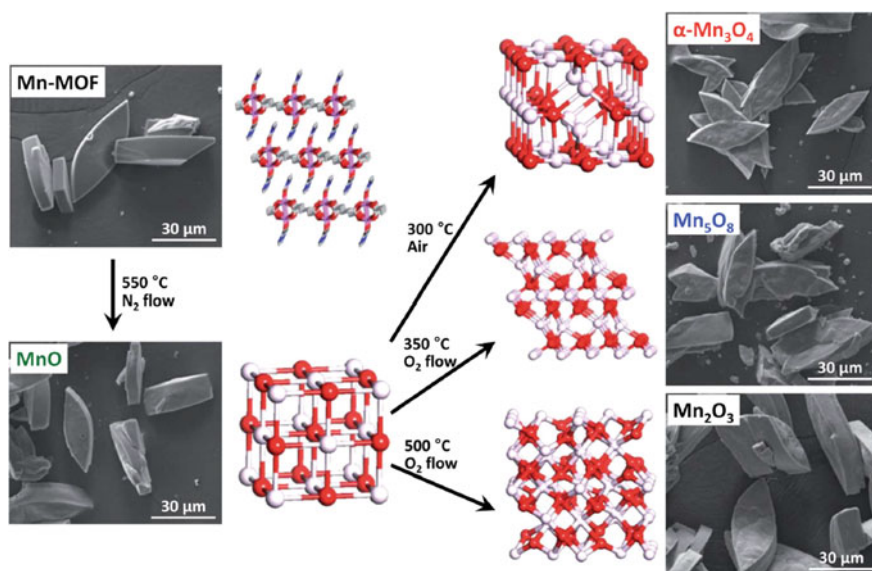


Fig. 8.49 SEM micrographs and diagram of structural transformations of $[\text{Mn}_2(\text{L})(\text{DMA})_2]_n$ in manganese oxides during thermolysis

nanorods with 30–60 nm in diameter and a few micrometers in length. Inspection of the images reveals that calcination of the first CP at 600 °C resulted in the formation of more uniform rods with longer length (Fig. 8.49c). Moreover, the results show that thermolysis temperature can influence the length of ZnO nanorods obtained from the first CP.

The thermolysis of the Zn(II) CPs $(\text{NH}_4)_n[\text{Zn}(\text{HL})\text{Cl}_2]_n$, $[\text{Zn}(\text{L})(\text{H}_2\text{O})_2]_n$, $[\text{Zn}(\text{HL})_2]_n \cdot 4n\text{H}_2\text{O}$ (H_2L = iminodiacetic acid) was used for the preparation of zinc oxide [339]. In particular, the product based on first polymer has the shape of a regular hexagonal pyramid with the mean diameter and length of ZnO crystal of 2.6 and 4.6 nm respectively, and the aspect (length/width) ratio of 1.8:1. The regular granular crystallites of ZnO having diameters of 25–202 nm were prepared from second and third polymers. Thus, the structure of the initial CPs has a substantial effect on the shape and size of formed ZnO nanomaterials [340, 341].

Thermolysis of the bulk powder and nano-sized Ni(II) MOF with cubic building blocks and 1D open channels, i.e. $\{[\text{Ni}_6(\text{Ni}_8\text{L}_{12})(\text{H}_2\text{O})_{20}(\text{H}_2\text{O})_4](\text{CH}_3\text{CN})(\text{H}_2\text{O})_{18.5}\}_\infty$ (H_3L = 4,5-imidazoledicarboxylic acid), at 700 °C under air yielded NiO nanoparticles, which size and morphology depends on the particle size of the initial compound [342].

The crystalline and nano-structures of two Pb(II) CPs, $[\text{Pb}_2(\text{L})_4(\text{MeOH})]_n$ (L = 2-pyrazinecarboxylic acid) and $[\text{Pb}(\text{L}')_2]_n$ (L' = 2-quinolinecarboxylic acid), were thermalized to prepare PbO nanoparticles with various morphology and size [343].

It should be noted that N,S-containing ligands were used not only to prepare metal sulfide nanoparticles, as expected, but also metal oxides, more thermodynamically stable in air. Thus, a ZnO nanostructure was prepared by thermolysis of nanoparticles of a Zn(II) CP, $[\text{Zn}(\text{L})(\text{CH}_3\text{COO})_2]_n$ (L = 2,2'-diamino-5,5'-dimethyl-4,4'-bithiazole), at 500 °C under air [344].

Saving macroscopic MOFs structure during their thermal transformation may serve as a promising strategy in the design of nanomaterials with predetermined properties and morphology.

8.4.2.2 Influence of Temperature

Temperature is an important parameter controlling the phase composition and morphology of the resulting nanostructures. Thus, controlled thermolysis of $[\text{Mn}_2(\text{L})(\text{DMA})_2]_n$ (L is *meso*-butane-1,2,3,4-tetracarboxylate, DMA is N,N-dimethylacetamide) [345] and $\text{Mn}_2(\text{L}')$ (L' is 2,5-dihydroxyterephthalate) [346] by varying the temperature and the atmosphere leads to the formation of a series of nanoporous manganese oxides with different degrees of oxidation: MnO, Mn_3O_4 , Mn_5O_8 , and Mn_2O and preserving the original morphology of the starting precursor (Fig. 8.49). Besides, varying the thermolysis temperature (300–7000 °C) of $\text{Mn}_2(\text{L}')$ [346] leads to reduction of lattice defects, increasing the crystallinity degree of the thermolysis products. At the same time, the crystal surface becomes uneven and a plurality of voids appears with temperature increasing. The prepared MnO_x are characterized by type IV adsorption isotherms, indicating their mesoporous structure. It should be noted that in this way rare low-valence oxides MnO and

metastable phases of Mn_5O_8 with nanoporous architecture can be obtained, i.e. MOF thermal transformation can significantly enrich the composition, structure and functional properties of the resulting nanoporous metal oxide materials [347].

Similar patterns are characteristic of thermal transformations of MIL-100(Fe) [348]. The average size of nanorods Fe_2O_3 , obtained at temperatures of 350, 550 and 750 °C is 50, 150 and 200 nm, respectively. Character of adsorption-desorption isotherms in this case is consistent with the general trend of the formation of the mesoporous structure of metal oxide nanocomposites obtained by MOF thermolysis. As a rule, surface area, pore volume, and pore size decreases with increasing thermolysis temperature, which also is in agreement with the fact that the thermally controlled crystal growth reduces the porosity with increasing process temperature.

The thermal decomposition of Prussian blue $\text{Fe}_4[\text{Fe}(\text{CN})_6]_3$ [291] at 350 and 450 °C leads to β - and cubic spinel γ - Fe_2O_3 hematite polymorphic modifications, respectively. At the same time, calcining $\text{Fe}_4[\text{Fe}(\text{CN})_6]_3$ at 250 °C results in the formation of spongy Fe_2O_3 with developed specific surface area 200–400 $\text{m}^2 \text{g}^{-1}$ depending on the particle size of the starting precursor. Structural changes during MOFs calcination process reflected in the evolution of nanoparticle morphology from spherical form to nanorods when changing the reaction temperature, for example, that is characteristic of ZnO nanoparticles produced by thermolysis of MOF based on $\text{Zn}(4-[(1\text{H-imidazol-4-yl)methylamino}]benzoate)$ [349]. In this case MOF was used as precursor as well as sacrificial template to synthesize hexagonal ZnO nanomaterials by calcination in air.

Thermolysis temperatures of two silver(I) CPs, $[\text{Ag}(\text{HQ})(\text{Q})]_n$ and $\{[\text{Ag}(\text{HQ})_2]\text{NO}_3\}_n$, has effect on the formation of silver nanomaterials [350]. In particular, increasing temperature leads to increase of agglomeration of silver nanoparticles.

Calcination of sinusoidal CP $[\text{Ag}(\text{L})](\text{ClO}_4)$, where L is a diethylbis(4-pyridyl) silane, at 400 °C gives circle morphology with evolving burned organics. At the same time, at 600 °C, network circles involving of a silver(0)/silver chloride (chlorargyrite)/silicon(IV) oxide composite with a micro-sized convexo-concave surface are formed [351]. However, thermolysis of $[\text{Ag}(\text{L})](\text{BF}_4)$ crystals at 600 °C gives silver(0) nanocomposites without silicon(IV) oxide.

It should be noted the zinc(II) oxide nanoparticles prepared by thermolysis of $[\text{Zn}(\text{L})_2(\text{H}_2\text{O})_4]_n$, $[\text{Zn}(\text{L}')_2(\text{H}_2\text{O})_2]_n$ and $[\text{Zn}(\text{H}_2\text{O})_6] \cdot (\text{L}'')_2$, where L is nicotinic acid N-oxide, L' is picolinic acid N-oxide and L'' is isonicotinic acid N-oxide, at two temperatures (200 and 600 °C) using two methods (with surfactant and without surfactant) [352]. Analysis of the SEM images of the prepared ZnO nanoparticles exhibits that small and spherical ZnO nanoparticles were prepared by thermolysis of compounds at 200 °C using surfactant (oleic acid).

Also, spongy CuO (average diameter from 10 to 20 μm) was synthesized [353] by thermolysis of $\text{Cu}_3(\text{L})_2$ (L = benzene-1,3,5-tricarboxylate). The product consisted of nanosheets with average edge length of 80–200 nm and thickness of about 30 nm.

8.4.2.3 Influence of Surfactants

It should be noted using surfactants in the synthesis of nanomaterials to change the morphology and particle size. For example, polymeric Zn(II) chelates were used for the preparation of nano-sized materials in the presence of surfactants [354–358].

Iron(III) oxide nanoparticles were prepared by thermolysis of a Fe(II) 1D CP, $[\text{Fe}(\text{L})_2](\text{SCN})_2 \cdot \text{MeOH}$, where L is 4'-(4-pyridyl)-tpy, in oleic acid (surfactant) [359]. Pure phase ZnO nanoparticles with various morphologies and sizes were synthesized by thermolysis of zinc(II) CPs, $[\text{Zn}(\text{L})(\text{OAc})]\text{ClO}_4$, $[\text{Zn}(\text{L})\text{I}_2]$, and $[\text{Zn}(\text{L})_2](\text{ClO}_4)_2(\text{H}_2\text{O})_{2.9}$ based on the same ligand L [360].

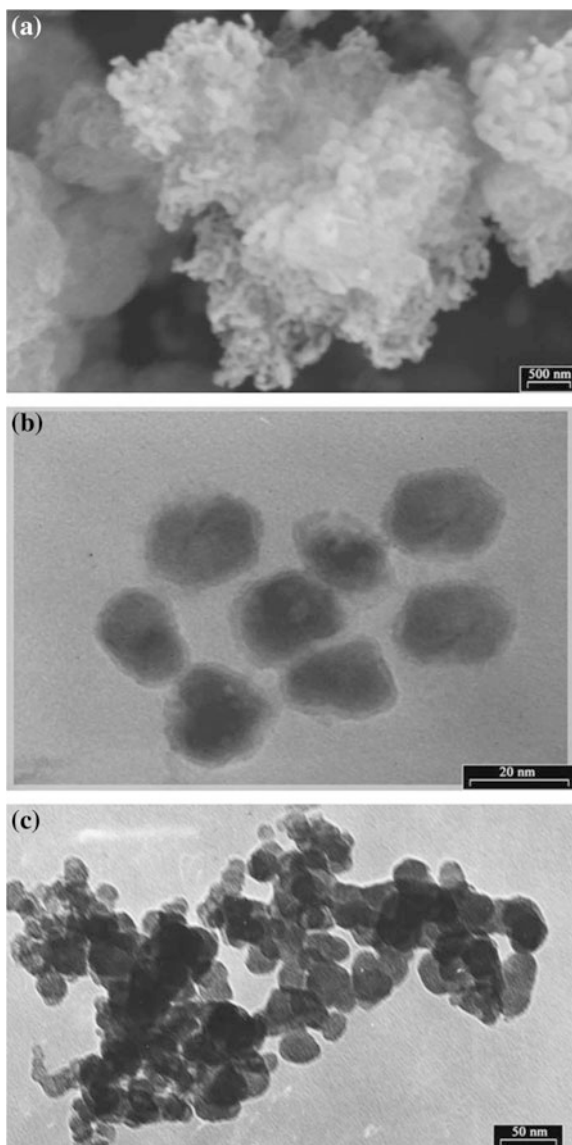
Of interest is the synthesis of PbO nanoparticles (~ 30 nm) by thermolysis of a Pb(II) complex, $\{[\text{Pb}_2(\text{L})_2(\text{NO}_3)_4] \cdot \text{MeOH}\}_n$, where L is N,N',N''-tris(pyrid-3-ylmethyl)-1,3,5-benzenetricarboxamide, at 180 °C with oleic acid as a surfactant [361].

$[\text{Co}(\text{L})(\text{H}_2\text{O})]_n$ polymer, where H_2L is phthalic acid, was used for the preparation of Co_3O_4 in the presence of oleic acid and triphenylphosphine [92]. The organic surfactants (oleic acid and triphenylphosphine) allow to preparing nanomaterials with narrow size distributions, size control and crystallinity of individual nanocrystals. The TEM image (Fig. 8.50a, b) shows that the particles with particle size about 20–30 nm are not fully spherical, however, each nanoparticle is separated from its neighbors by the organic surfactant shell. The comparison of the nanoparticles obtained in the presence of oleic acid and triphenylphosphine (Fig. 8.50b) and in the presence of oleic acid without triphenylphosphine (Fig. 8.50c) indicates that the nanoparticles prepared in first case are smaller without any agglomeration.

The thermolysis of Pb(II) 2D CPs, $[\text{Pb}_2(\mu_2\text{-L})_2(\text{NO}_3)_4]_n$, where L is 1,6-bis(2-pyridyl)-2,5-diaza-1,5-hexadiene, in oleic acid as a surfactant led to PbO particles about 60 nm [362]. We note also PbO nanoparticles (~ 25 nm) obtained by thermolysis of plate-shaped nanostructures of a 1D lead(II) CP involving the $\text{Pb}_2(\mu\text{-I})_2$ fragment, $[\text{Pb}(\text{L})\text{I}_2]_n$ (L = neocuproine or 2,9-dimethyl-phen), with oleic acid as a surfactant [363].

The ZnO nanoparticles were synthesized by thermolysis of nano-compound $[\text{Zn}(5,5'\text{-di-tert-butyl-bpy})\text{Cl}_2]_n$ and similar compound, $[\text{Zn}(5,5'\text{-dimethyl-bpy})\text{Cl}_2]_n$, using two methods (with and without surfactant) [364]. The average size of ZnO nanoparticles is equal to 78 and 50 nm for these compounds, respectively. The ZnO nano-sized particles were also prepared by thermolysis of 1D CP, $\{[\text{Zn}(\mu\text{-L})(\text{L})_2(\text{H}_2\text{O})_2](\text{ClO}_4)_2 \cdot \text{L}\}_n$, where L is 1,4-bis(3-pyridyl)-2,3-diaza-1,3-butadiene, at 400 °C under air atmosphere as well as in oleic acid at 200 °C [365]. The diameter of the prepared product is equal to 40 nm (Fig. 8.51).

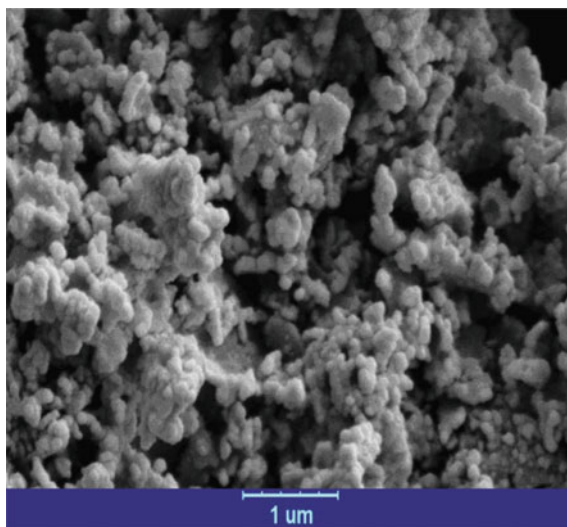
Fig. 8.50 **a** SEM, **b** TEM images of Co_3O_4 nanoparticles obtained in the presence of OA and TPP and **c** TEM image of Co_3O_4 nanoparticles obtained in the presence of OA without TPP



8.4.3 Polymer Derived Non-oxide Nanocomposites

At present, using different targeted silicon-based preceramic polymers [366], such as polysiloxane, polycarbosilane and polysilazane as precursors for polymer-derived ceramics (PDCs) [367, 368] has become widespread [369–374].

Fig. 8.51 SEM images of ZnO nanoparticles prepared by direct calcination of $\{[\text{Zn}(\mu\text{-L})(\text{L})_2(\text{H}_2\text{O})_2](\text{ClO}_4)_2 \cdot \text{L}\}_n$



Controlled thermolysis of silicon-based preceramic polymers allows to preparing nano-sized ceramics, which structure is determined by the spatial organization of precursors, ways of their processing and thermolysis parameters. In particular, silicon-based preceramic polymers are subjected to different transformations depending on the temperature (Fig. 8.52) [368]. These transformations include polymerization, shaping, cross-linking, pyrolysis and annealing.

It should be noted that the preparation of PDCs is a relatively new technology possessing a number of advantages over the classical production [375]. Using metal chelates for modification of the polymer allows to producing new ceramic materials with high purity and homogenous distribution of the elements at relatively lower temperatures (1000 °C).

As an example, we consider the chemical modification of commercially available polysilazane (HTT1800) by an aminopyridinato Ni(II) chelate based on (4-methylpyridin-2-yl) trimethylsilanylamine for the production of nanoporous silicon

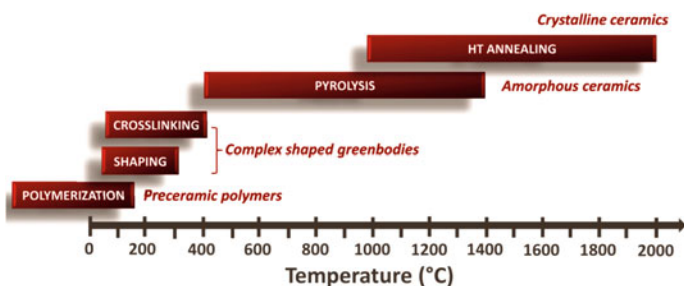


Fig. 8.52 Polymer-to-ceramic transformation of preceramic polymers

oxycarbo-nitride ceramics contained Ni nano-sized particles [376]. It is important that amido complexes involve the same elements (Si, C and N atoms), which are in the precursor polymer, thus avoiding the inclusion of other elements into the ceramic nanomaterials. The Ni-polysilazane precursors are superparamagnetic indicating formation of nickel nano-sized particles ($\sim 2\text{--}3$ nm). The thermolysis of polysilazane precursors modified by aminopyridinato nickel chelate at 700°C leads to nanoporous ceramic composites with a BET surface area of $215\text{ m}^2\text{ g}^{-1}$, a micropore surface area of $205\text{ m}^2\text{ g}^{-1}$, and a micropore volume of $0.113\text{ cm}^3\text{ g}^{-1}$.

Analogous microporous nanomaterials with specific surface area $\approx 400\text{ m}^2\text{ g}^{-1}$ including nickel nano-sized particles were prepared by using various and controlled Si:Ni ratios in THF [377]. The amido nickel complex catalyzed the cross-linking of HTT1800 by hydrosilylation at room temperature. The formation of nickel nano-sized particles and micropores occurs by thermolysis at 600°C according to an agreed mechanism.

Of interest is Ni-containing SiC ceramics prepared via the self-assembly of allylhydridopolycarbosilane-*b*-PE [378]. It is important that the added aminopyridinato nickel chelate also catalyzed the cross-linking the allylhydridopolycarbosilane block.

During modification of the HTT1800 by the aminopyridinato copper complexes the metal transfer from the chelate to the polymer occurs (Fig. 8.53) [379]. The ^1H and ^{13}C NMR studies of the reaction confirm the transfer of the metal to the nitrogen donor atoms of the polymer (Fig. 8.54). The thermolysis at 1000°C of a metal modified polymer cross-linked with use of dicumylperoxide results in copper-containing SiCN (Cu@SiCN). It is important that the size of the Cu particles in Cu@SiCN depends on the content of copper chelate (Fig. 8.55).

Unusual behavior was observed for palladium aminopyridinates which produce intermetallic nano-sized particles. In particular, an aminopyridinato palladium chelate allows to simultaneous modification of the polyorganosilazane and its cross-linking [380]. It is important that the ceramic yield was even higher than that for the pure polyorganosilazane. Besides, the amount of the added palladium chelate increases their population density but does not affect the particle size (Fig. 8.56).

Of interest is the modification of HTT1800 by aminopyridinato metal chelates (M=Fe, Co, Pt, Cu, Ag, Au) along with the addition of the sacrificial filler (PE), which allows to generating both porosity (Fig. 8.57) and MWCNT (Figs. 8.57c and 8.58) [381]. It should be noted that cobalt and iron are more effective in the production of MWCNT than the other metals.

8.4.4 Mixed-Oxide Nanocomposites

Heterometallic chelates are of interest for preparation of functional oxide materials (e.g., metal-oxide ceramics). The main advantages of using heterometallic chelates

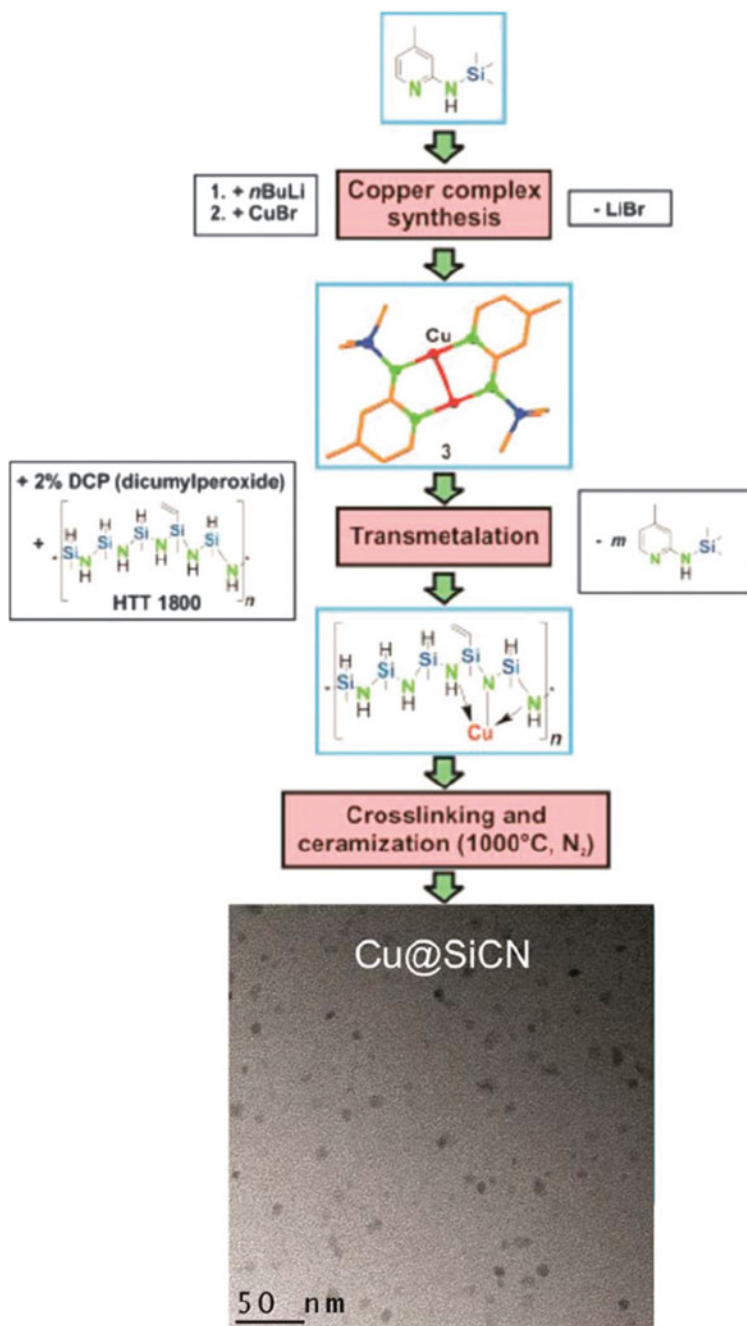


Fig. 8.53 Modification of HTT1800 with an aminopyridinato copper complex leading to Cu-containing SiCN ceramics by pyrolysis to 1000 °C under nitrogen

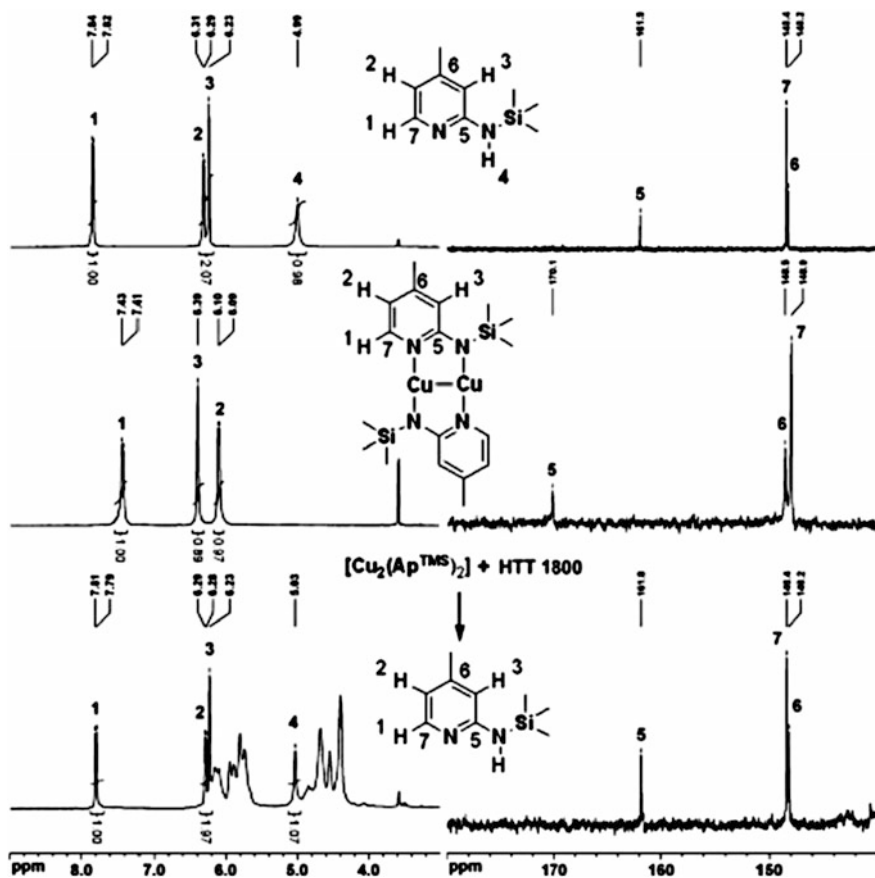


Fig. 8.54 ¹H (left) and ¹³C NMR spectra (right) of ApTMSH (top), [Cu₂Ap₂TMS] (middle), and after its reaction with HTT1800 (bottom)

as precursors of nanomaterials are low temperature of thermolysis, the exact ratio of metal ions, the formed nanoparticle size control, etc. [42, 382–388].

As a typical example, we consider using mixed lanthanide CPs for the production of rare earth oxides [389]. In particular, well-defined cylindrical or spherical micro-morphologies can be prepared by varying solvents (water or THF) which were discovered in the resulting oxides after thermal treatment. Such bimetallic CPs were synthesized by the interaction of chlorides or nitrates of Ce, Nd, Gd with 2,5-dihydroxy-1,4-benzoquinone and used as precursors for mixed oxide ceramics. Thermolysis at 850 °C of the CPs leads to mixed Nd_xGd_(1-x) and Nd_xCe_(1-x) oxides as solid solutions, in which *x* varies between 0 and 1. It should be noted that using well-characterized CPs as precursors allows to controlling over the atom sequences in the chains, the number of coordination bonds and the dimensionality of the precursor structure.

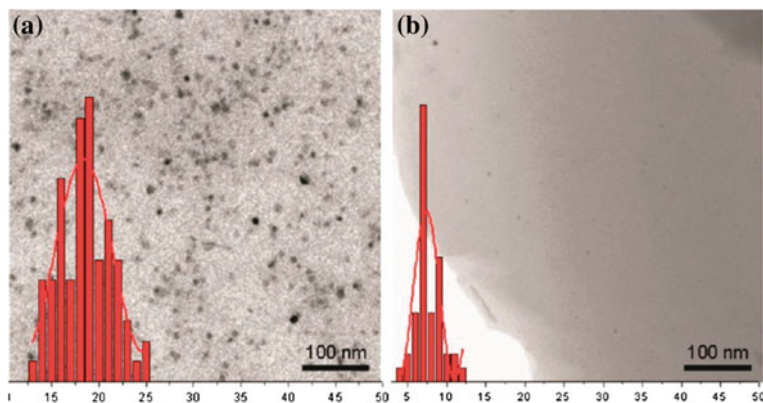


Fig. 8.55 TEM micrographs of Cu@SiCN: **a** Si/Cu = 10 **b** Si/Cu = 100 including particle size distribution statistics

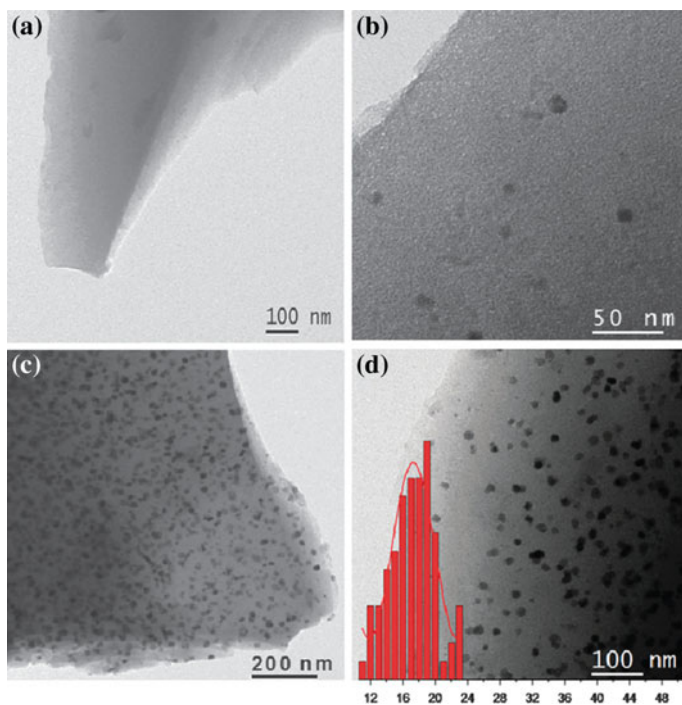


Fig. 8.56 TEM micrographs of ceramic materials. **a** SiCN ceramic without palladium loading does not show any particles; **b** lower loading of palladium (0.2 wt%, Si/Pd ratio 1000) decreases the density of particles keeping their size in the same regime; **c** Pd₂Si particles uniformly distributed over the ceramic support Si/Pd = 20 (8 wt% Pd); **d** particle size distribution for the sample shown in (c)

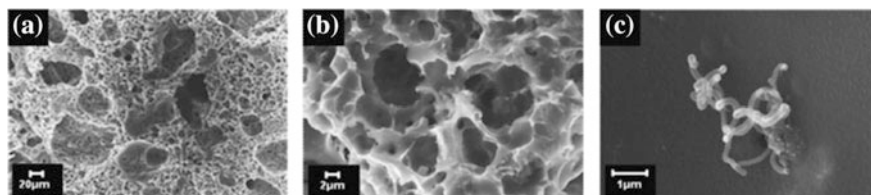


Fig. 8.57 a–c SEM micrographs of an Au@SiCN ceramic (1000 °C/N₂; Au:Si = 1:50)

The thermolysis of CPs [BaCu(L)₂]_n, [BaCu(L)₂(H₂O)]_n and [Ba₃Cu₃(L)₆(H₂O)₁₁]_n·2n(H₂O), where H₂L is 1,1-cyclopropanedicarboxylic, 1,1-cyclobutanedicarboxylic and butylmalonic acid, respectively, occurs above 170 °C and leads to the formation of BaCuO₂ [390]. It is important that the thermolysis conditions have effect on the phase compositions of nanomaterials and the formation of BaCuO₂ proceeds under milder conditions from latter CP than those from the first two CPs.

It should be noted isostructural polymeric complexes [Ln(L)(acac)₂(H₂O)]_n (Ln = Eu, Gd, Tb, Dy, Ho, Er; L = (η⁵-C₅H₄)Mn(CO)₃), thermolysis of which in air and under Ar atmosphere affords LnMnO₃ phases [391]. For the Dy and Ho chelates adiabatic calorimetric data permit to calculate standard thermodynamic functions.

Of interest are 3D-porous CPs [(H₂O)₃(μ-H₂O)₂CuBa(μ₃-L)(L)]_n and [(μ-H₂O)CuBa(μ₃-L)(μ₄-L)]_n, where HL is dimethylmalonic acid [392]. Complete solid-phase thermolysis of the CPs leads to a mixture of BaCuO₂, BaCO₃, and CuO. It is important that a crystalline phase of pure cubic BaCuO₂ can be obtained using special conditions. The thermal dehydration of Ba–Co and Ba–Zn heterometallic 3D CPs [BaM(H₂O)₅(L)₂]_n based on the same ligand occurs in one step [393]. Crystalline BaCoO_{3–x} and BaZnO₂ are products of solid state thermolysis of the CPs under the following conditions: air flow rate 60 ml min⁻¹, heating rate 10 °C min⁻¹ up to *t* = 800 °C (1) or 750 °C (2), followed by storage for 12 h at the same temperatures (Fig. 8.59).

Of interest is using in situ polymerizable complex method for the preparation of a polymeric precursor of the phase La₂Mo₂O₉ [394]. SEM reveals a different morphology of powder nanoparticles after thermolysis at selected temperatures and powder X-ray diffraction patterns were prepared for phase identification (Fig. 8.60).

Mixed-metal oxalates were used for preparation of bimetallic or mixed-oxide nanostructures. Thus, thermolysis of 2D polymetallic oxalate-bridged polymeric networks [395] of the formula [M^{II}(H₂O)₂]₃[M^{III}(ox)₃]₂(18-crown-6)₂ (M^{III} = Cr, Fe; M^{II} = Mn, Fe, Co, Ni; 18-crown-6) leads to pure phases of mixed oxides with spinel-like structures as (Mn,Co,Fe)₃O₄.

Mesoporous nickel ferrite (NiFe₂O₄) spheres were prepared by an aerosol spray pyrolysis method using Pluronic F127 as a structure-directing agent, and metal nitrates were used as inorganic precursors for the oxide [396]. Self-assembly of organic and inorganic species followed by metal nitrate decomposition and inorganic polymerization were accomplished in the ethanol aerosol droplets in N₂

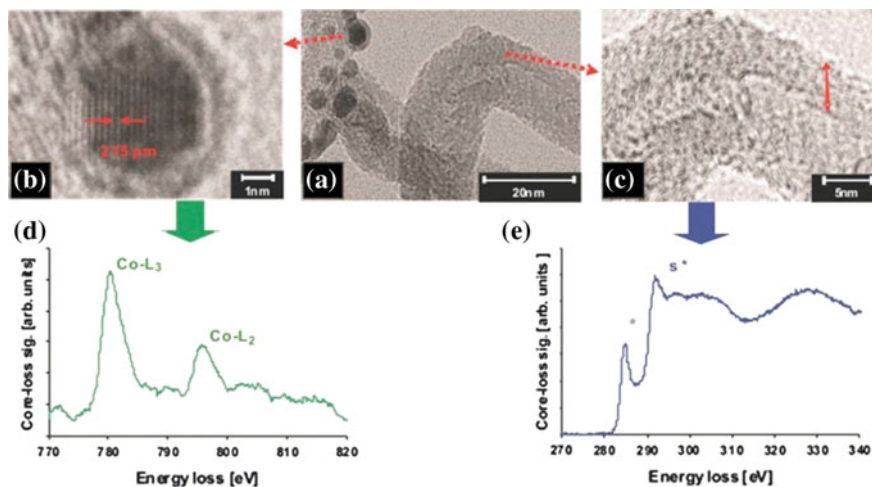


Fig. 8.58 a–c TEM micrographs of a Co@SiCN ceramic (Co:Si ratio = 1:50) d core-loss EELS of the metal particle e core-loss EELS of the carbon nanotube

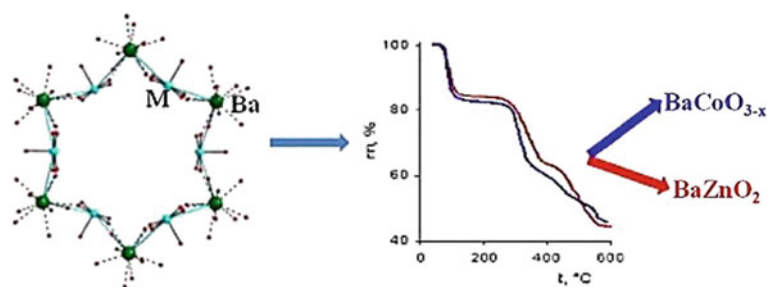


Fig. 8.59 Preparation of crystalline BaCoO_{3-x} and BaZnO_2 as a result of solid state thermolysis of the CPs

atmosphere at 400 °C. It is important that the solvent evaporation at 50 °C in the chamber induced the self-assembly between the structure-directing agent and the metal ions. It should be noted that mesoporous crystalline nickel ferrite spheres were obtained after the spheres were calcined at 300 °C in air to remove the structure-directing agent and increase crystallinity. Mesoporous NiFe_2O_4 spheres of high specific surface area ($278 \text{ m}^2 \text{ g}^{-1}$) with a highly crystalline framework were prepared by adjusting the amount of structure-directing agent and the calcining condition.

Of interest is the preparation of Ni–Fe bimetallic oxide nanotubes with a hollow and porous structure by MOF thermolysis [397]. It is important that the Ni/Fe molar ratios in the binary metal oxide can be regulated. In particular, $\text{Ni}_{0.62}\text{Fe}_{2.38}\text{O}_4$

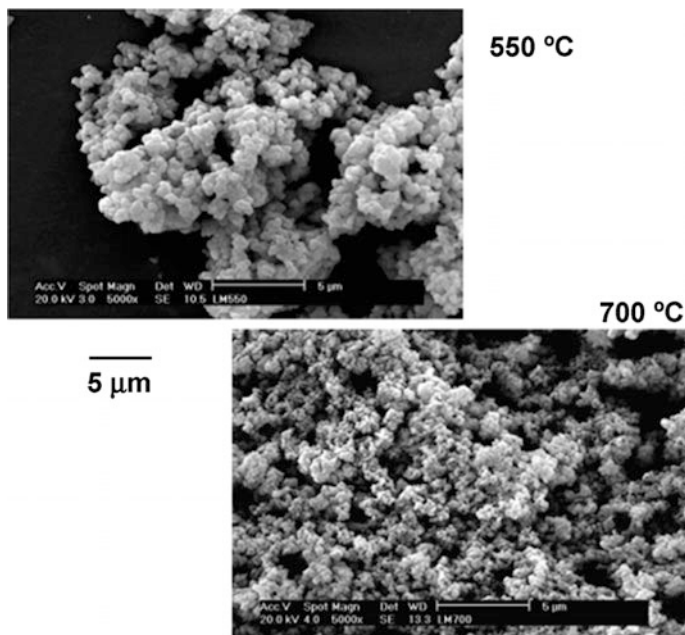


Fig. 8.60 SEM of the phase $\text{La}_2\text{Mo}_2\text{O}_9$ prepared at different temperatures

nanotubes with a tube shell of around 10 nm have a specific surface area of $134.3 \text{ m}^2 \text{ g}^{-1}$ and are composed of nano-sized primary particles.

Of course, the range of nanostructures produced in the course of thermal transformations of PMC is quite wide, and is not limited to the examples discussed here. Huge selection of precursor organometallic structures and coordination polymers with a wide arsenal of synthetic methods for their preparation, ease of many recipes, scalability and acceptable ratio price/quality provide a methodological platform to build on the basis of PMC promising new materials including metal nanostructures [398–400], nanoalloys [401, 402], metal chalcogenides [403–405], metal carbides [406], etc.

References

1. T. Zhang, J. Ge, Y. Hu, Y. Yin, *Nano Lett.*, ASAP Article
2. A.P. Reverberi, N.T. Kuznetsov, V.P. Meshalkin, M. Salerno, B. Fabiano, *Theor. Found. Chem. Eng.* **50**, 59 (2016)
3. W.L. Leong, J.J. Vittal, *Chem. Rev.* **111**, 688 (2010)
4. H. Liu, J. Owen, A.P. Alivisatos, *J. Am. Chem. Soc.* **129**, 305 (2007)
5. L.H. Qu, W.W. Yu, X.P. Peng, *Nano Lett.* **4**, 465 (2004)
6. Z.A. Peng, X.G. Peng, *J. Am. Chem. Soc.* **124**, 3343 (2002)
7. C.R. Bullen, P. Mulvaney, *Nano Lett.* **4**, 2303 (2004)

8. A.D. Pomogailo, G.I. Dzhardimalieva, *Nanostructured Materials Preparation via Condensation Ways* (Springer, Dordrecht, 2014)
9. D. Wöhrle, A.D. Pomogailo, *Metal Complexes and Metals in Macromolecules* (Wiley-VCH, Weinheim, 2003)
10. A.D. Pomogailo, A.S. Rozenberg, I.E. Uflyand, *Metal Nanoparticles in Polymers* (Khimiya, Moscow, 2000)
11. A.D. Pomogailo, G.I. Dzhardimalieva, V.N. Kestelman, *Macromolecular metal carboxylates and their nanocomposites* (Springer, Heidelberg, 2010)
12. G.I. Dzhardimalieva, A.D. Pomogailo, Russ. Chem. Rev. **77**, 259 (2008)
13. A.D. Pomogailo, A.S. Rozenberg, G.I. Dzhardimalieva, Russ. Chem. Rev. **80**, 257 (2011)
14. A.D. Pomogailo, V.V. Savostyanov, *Synthesis and Polymerization of Metal-Containing Monomers* (CRC Press, Boca Raton, London, NY, 1994)
15. A.D. Pomogailo, G.I. Dzhardimalieva, *Monomeric and Polymeric Metal Carboxylates* (Fizmatlit, Moscow, 2009)
16. M.Y. Masoomi, A. Morsali, Coord. Chem. Rev. **256**, 2921 (2012)
17. B.I. Kharisov, O.V. Kharissova, U.O. Méndez, J. Coord. Chem. **66**, 3791 (2013)
18. A.D. Pomogailo, G.I. Dzhardimalieva, *Metallopolymeric Hybrid Nanocomposites* (Nauka, Moscow, 2015)
19. *Nanocrystals: synthesis, properties and application*, eds. by C.N.R. Rap, P.J. Thomas, G.U. Kulkarni (Springer, Berlin, Heidelberg, 2007)
20. O. Carp, Materials Obtained by Solid-State Thermal Decomposition of Coordination Compounds and Metal-Organic Coordination Polymers, in *Reactions and Mechanisms in Thermal Analysis of Advanced Materials*, eds. by A. Tiwari, B. Raj (Scrivener Publishing LLC, Salem, Massachusetts, 2015)
21. Y. Song, X. Li, L. Sun, L. Wang, RSC Adv. **5**, 7267 (2015)
22. J.-K. Sun, Q. Xu, Energy Environ. Sci. **7**, 2071 (2014)
23. M. Ramazani, A. Morsali, Ultrason. Sonochem. **18**, 1160 (2011)
24. M.A. Malik, P. O'Brien, *Organometallic and Metallo-Organic Precursors for Nanoparticles. Precursor Chemistry of Advanced Materials* (Springer, Berlin, Heidelberg, 2005)
25. M. Ramanathana, S.B. Darling, Polym. Int. **62**, 1123 (2013)
26. B.I. Kharisov, H.V. Rasika Dias, O.V. Kharissova, V.M. Jiménez-Pérez, B.O. Pérez, B.M. Flores, RSC Adv. **2**, 9325 (2012)
27. V.A. Logvinenko, F. Paulik, I. Paulik, *Kvaziravnovesnaya Termogravimetriya v Sovremennoi Neorganicheskoi Khimii (Quasi-equilibrium Thermogravimetry in Modern Inorganic Chemistry)* (Nauka, Novosibirsk, 1989)
28. J. Paulik, F. Paulik, Therm. Acta. **100**, 23 (1986)
29. A.S. Shteinberg, *Fast Reactions in Energetic Materials: High-Temperature Decomposition of Rocket Propellants and Explosives* (Fizmatlit, Moscow, 2006)
30. S.V. Pol, V.S. Pol, A. Gedanken, Chem. - Eur. J. **10**, 4467 (2004)
31. J.Q. Sun, X.P. Shen, L.J. Guo, K.M. Chen, Q. Liu, Phys. E. Low Dimens. Syst. Nanostr. **41**, 1527 (2009)
32. J.Q. Sun, X.P. Shen, K.M. Chen, Q. Liu, W. Liu, Solid State. Comm. **147**, 501 (2008)
33. M. Bowtell, Adhes. Age. **40**, 62 (1997)
34. G.P. Shveikin, I.V. Nikolaenko, Theor. Found. Chem. Eng. **43**, 553 (2009)
35. Y.C. Kang, S.B. Park, I.W. Lenggoro, K. Okuyama, J. Mater. Res. **14**, 2611 (1999)
36. I.W. Lenggoro, T. Hata, F. Iskandar, J. Mater. Res. **15**, 733 (2000)
37. H.K. Kammler, L. Mädler, S.E. Pratsinis, Chem. Eng. Technol. **24**, 583 (2001)
38. E.K. Athanassiou, R.N. Grass, W.J. Stark, Nanotechnol. **17**, 1668 (2006)
39. M.T. Swihart, Curr. Opin. Colloid. Interf. Sci. **8**, 127 (2003)
40. C. Boissiere, D. Grosso, A. Chaumonnot, L. Nicole, C. Sanchez, Adv. Mater. **23**, 599 (2011)
41. C.-K. Tsung, J. Fan, N. Zheng, Q. Shi, A.J. Forman, J. Wang, G.D. Stucky, Angew. Chem. Int. Ed. **47**, 8682 (2008)
42. T.A. Ostomel, Q. Shi, C.-K. Tsung, H. Liang, G.D. Stucky, Small **2**, 1261 (2006)

43. L. Li, C.-K. Tsung, Z. Yang, G.D. Stucky, L.D. Sun, J.F. Wang, C.H. Yan, *Adv. Mater.* **20**, 903 (2008)
44. Y. Lu, H. Fan, A. Stump, T.L. Ward, T. Rieker, C.J. Brinker, *Nature*. **398**, 223 (1999)
45. A.K.P. Mann, S.E. Skrabalak, *Chem. Mater.* **23**, 1017 (2011)
46. J.B. Pang, J.N. Stuecker, Y.B. Jiang, A.J. Bhakta, E.D. Branson, P. Li, J. Cesarano, D. Sutton, P. Calvert, C.J. Brinker, *Small*. **4**, 982 (2008)
47. D.S. Jung, S.B. Park, Y.C. Kang, *Korean J. Chem. Eng.* **27**, 1621 (2010)
48. J.-C. Lin, J.W. Gentry, *J. Aerosol Sci.* **31**, 797 (2000)
49. N. Reuge, B. Caussat, *Comput. Chem. Eng.* **31**, 1088 (2007)
50. I.W. Lengggoro, Y. Itoh, K. Okuyama, T.O. Kim, *J. Mater. Res.* **19**, 3534 (2004)
51. W.-N. Wang, A. Purwanto, K. Okuyama, in *Handbook of Atomization and Sprays*, ed. by N. Ashgriz (Springer Science Business Media, LLC, 2011)
52. Y.C. Kang, Y.S. Chung, S.B. Park, *J. Am. Ceram. Soc.* **82**, 2056 (1999)
53. K. Okuyama, I.W. Lengggoro, *Chem. Eng. Sci.* **58**, 537 (2003)
54. W.-N. Wang, I.W. Lengggoro, Y. Terashi, T.O. Kim, K. Okuyama, *Mat. Sci. Eng. B.* **123**, 194 (2005)
55. Y.C. Kang, S.B. Park, *Mater. Res. Bull.* **35**, 1143 (2000)
56. W.-N. Wang, I.W. Lengggoro, Y. Terashi, Y.C. Wang, K. Okuyama, *J. Mater. Res.* **20**, 2873 (2005)
57. I.W. Lengggoro, Y. Itoh, N. Iida, K. Okuyama, *Mater. Res. Bull.* **38**, 1819 (2003)
58. H. Biederman, in *Plasma Polymer Films* (Imperial College Press, London, 2004)
59. A. Biswas, Z. Marton, J. Kanzow, J. Kruse, V. Zaporojtchenko, F. Faupel, T. Strunskus, *Nano Lett.* **3**, 1 (2003)
60. H. Takele, H. Greve, C. Pochstein, V. Zaporojtchenko, F. Faupel, *Nanotechnology.* **17**, 3499 (2006)
61. D. Barreca, A. Gasparotto, C. Maragno, E. Tondello, C. Sada, *Chem. Vap. Deposition.* **10**, 229 (2004)
62. K. Ramasamy, M.A. Malik, P. O'Brien, J. Raftery, *Dalton Trans.* **39**, 1460 (2010)
63. D. Barreca, A. Gasparotto, C. Maragno, R. Seraglia, E. Tondello, A. Venzo, V. Krishnan, H. Bertagnolli, *Appl. Organometal. Chem.* **19**, 129 (2005)
64. S. Mlowe, L.D. Nyamen, P.T. Ndifon, M.A. Malik, J. Raftery, P. O'Brien, N. Revaprasadu, *Inorg. Chim. Acta.* **434**, 181 (2015)
65. S. Mlowe, D.J. Lewis, M.A. Malik, J. Raftery, E.B. Mubofu, P. O'Brien, N. Revaprasadu, *New J. Chem.* **38**, 6073 (2014)
66. R. Morrish, R. Silverstein, C.A. Wolden, *J. Am. Chem. Soc.* **134**, 17854 (2012)
67. V.G. Bessergenev, R.J.F. Pereira, A.M.B. do Rego, *Surf. Coat. Technol.* **201**, 9141 (2007)
68. R.K. Sharma, G. Kedarnath, V.K. Jain, A. Wadawale, M. Nalliath, C.G.S. Pillai, B. Vishwanadh, *Dalton Trans.* **39**, 8779 (2010)
69. C.B. Murray, D.J. Norris, M.G. Bawendi, *J. Am. Chem. Soc.* **115**, 8706 (1993)
70. N.L. Pickett, P. O'Brien, *Chem. Rec.* **1**, 467 (2001)
71. M.A. Malik, N. Revaprasadu, P. O'Brien, *Chem. Mater.* **13**, 913 (2001)
72. J. Rodriguez Castro, K.C. Molloy, Y. Liu, C.S. Lai, Z. Dong, T.J. White, E.R.T. Tiekink, *J. Mater. Chem.* **18**, 5399 (2008)
73. H. Liang, J.M. Raitano, L. Zhang, S.-W. Chan, *Chem. Commun.* 7569 (2009)
74. A. Hosseinian, S. Jabbari, H.R. Rahimpour, A.R. Mahjoub, *J. Mol. Struct.* **1028**, 215 (2012)
75. A. Hosseinian, A.R. Mahjoub, *J. Mol. Struct.* **985**, 270 (2011)
76. A. Hosseinian, A.R. Mahjoub, M. Movahedi, *Int. J. Nano Dim.* **1**, 65 (2010)
77. D. Czakis-Sulikowska, J. Radwanska-Doczekalska, M. Markiewicz, M. Pietrzak, *J. Therm. Anal. Calor.* **93**, 789 (2008)
78. D. Kumar, I.P.S. Kapoor, G. Singh, N. Geol, U.P. Singh, *J. Therm. Anal. Calor.* **107**, 325 (2011)
79. N. Parveen, R. Nazir, M. Mazhar, *J. Therm. Anal. Calor.* **111**, 93 (2013)
80. R. Nazir, M. Mazhar, T. Wakeel, M.J. Akhtar, M. Siddique, M. Nadeem, N.A. Khan, M.R. Shah, *J. Therm. Anal. Calor.* **110**, 707 (2012)

81. V.G. Makhankova, O.V. Khavryuchenko, V.V. Lisnyak, V.N. Kokozay, V.V. Dyakonenko, O.V. Shishkin, B.W. Skelton, J. Jezierska, *J. Solid State Chem.* **183**, 2695 (2010)
82. G. Singh, D.K. Pandey, *Propellant. Explor. Pyrotech.* **28**, 231 (2003)
83. P.R. Ponminniessary, A. Vasudevan, M. Sebastian, U.A. Chennampilly, K.M.Y. Karukapadath, *J. Therm. Anal. Calor.* **100**, 733 (2010)
84. K.S. Pejitha, S. Mathew, *J. Therm. Anal. Calor.* **93**, 213 (2008)
85. S. Bahemmat, M. Ghassemzadeh, M. Afsharpour, K. Harms, *Polyhedron* **89**, 196 (2015)
86. J. Chandradass, K.H. Kim, *Mater. Manuf. Processes.* **24**, 541 (2009)
87. Y. Hanifehpour, B. Mirtamizdoust, S.W. Joo, Z. Anorg, *Allg. Chem.* **638**, 357 (2012)
88. S. Kumar, J.A. Azurdia, R.M. Laine, *J. Ceram. Proc. Res.* **11**, 517 (2010)
89. X. Wang, X.Y. Chen, L.S. Gao, H.G. Zheng, Z. Zhang, Y.T. Qian, *J. Phys. Chem. B* **108**, 16401 (2004)
90. J.Z.L. Zhang, H.R. Geng, L.S. Zheng, D. Du, *J. Alloys Compd.* **392**, 317 (2005)
91. A. Khansari, M. Salavati-Niasari, A.K. Babaheydari, *J. Clust. Sci.* **23**, 557 (2012)
92. F. Mohandes, F. Davar, M. Salavati-Niasari, *J. Magn. Magn. Mater.* **322**, 872 (2010)
93. A. Khansari, M. Enhessari, M. Salavati-Niasari, *J. Clust. Sci.* **24**, 289 (2013)
94. D. Matioszek, W.-S. Ojo, A. Cornejo, N. Katir, M. El Ezzi, M. Le Troedec, H. Martinez, H. Gornitzka, A. Castel, C. Nayral, F. Delpesch, *Dalton Trans.* **44**, 7242 (2015)
95. T. Trindade, P. O'Brien, *Adv. Mater.* **8**, 161 (1996)
96. M. Lazell, P. O'Brien, *J. Chem. Soc. Chem. Commun.* 2041 (1999)
97. D.J. Crouch, P. O'Brien, M.A. Malik, P.J. Skabara, S.P. Wright, *J. Chem. Soc. Chem. Commun.* 1454 (2003)
98. S. Taniguchi, M. Green, *J. Mater. Chem. C* **3**, 8425 (2015)
99. Y.W. Jun, C.S. Choi, J. Cheon, *J. Chem. Soc. Chem. Commun.* 101 (2001)
100. M. Ranjbar, N. Shahsavan, M. Yousefi, *Am. Chem. Sci. J.* **2**, 111 (2012)
101. M. Edrissi, A.R. Keshavarz, *Nano-Micro Lett.* **4**, 83 (2012)
102. P. Bera, C.H. Kim, S.I. Seok, *Solid State Sci.* **12**, 532 (2010)
103. R. Amutha, S. Akilandeswari, A.N. Kannappan, M. Muruganandham, M. Sillanpää, *Adv. Sci. Lett.* **3**, 398 (2010)
104. A.L. Abdelhady, M. Afzaal, M.A. Malik, P. O'Brien, *J. Mater. Chem.* **21**, 18768 (2011)
105. N. Srinivasan, S. Thirumaran, S. Ciattini, *J. Mol. Struct.* **1026**, 102 (2012)
106. N. Srinivasan, S. Thirumaran, S. Ciattini, *Spectrochim. Acta. Part A: Mol. Biomol. Spectr.* **102**, 263 (2013)
107. W. Qingqing, X. Gang, H. Gaorong, *J. Solid State Chem.* **178**, 2680 (2005)
108. S.N. Mlondo, N. Revaprasadu, P. Christian, P. O'Brien, *Polyhedron* **28**, 2097 (2009)
109. Y. Li, X. Li, C. Yang, Y. Li, *J. Mater. Chem.* **13**, 2641 (2003)
110. P.S. Nair, T. Radhakrishnan, N. Revaprasadu, G.A. Kolawole, P. O'Brien, *J. Mater. Chem.* **12**, 2722 (2002)
111. J.C. Bruce, N. Revaprasadu, K.R. Koch, *New J. Chem.* **31**, 1647 (2007)
112. N. Moloto, N. Revaprasadu, M.J. Moloto, P. O'Brien, M. Helliwell, *Polyhedron* **26**, 3947 (2007)
113. G. Kedarnath, V.K. Jain, S. Ghoshal, G.K. Dey, C.A. Ellis, E.R.T. Tiekink, *Eur. J. Inorg. Chem.* 1566 (2007)
114. E.S. Raper, *Coord. Chem. Rev.* **165**, 475 (1997)
115. S. Narayan, V.K. Jain, B. Varghese, *J. Chem. Soc. Dalton Trans.* 2359 (1998)
116. J. Laube, S. Jager, C. Thone, *Eur. J. Inorg. Chem.* 198 (2001)
117. S. Dey, V.K. Jain, J. Singh, V. Trehan, K.K. Bhasin, B. Varghese, *Eur. J. Inorg. Chem.* 744 (2003)
118. G. Kedarnath, V.K. Jain, A. Wadawale, G.K. Dey, *Dalton Trans.* 8378 (2009)
119. M. Chunggaze, M.A. Malik, P. O'Brien, *Adv. Mater. Opt. Electron.* **7**, 311 (1997)
120. P. O'Brien, in *Inorganic materials*, eds. by D.W. Bruce, D. O'Hare (Wiley, NY, 1992)
121. N. Srinivasan, S. Thirumarana, S. Ciattini, *J. Mol. Struct.* **936**, 234 (2009)
122. L.D. Nyamen, A.A. Nejo, V.S.R. Pullabhotla, P.T. Ndifon, M.A. Malik, J. Akhtar, P. O'Brien, *N. Revaprasadu, Polyhedron.* **67**, 129 (2014)

123. S. Mlowe, D.J. Lewis, M.A. Malik, J. Raftery, E.B. Mubofu, P. O'Brien, N. Revaprasadu, *Dalton Trans.* **45**, 2647 (2016)
124. M. Chunggaze, M.A. Malik, P. O'Brien, *J. Mater. Chem.* **9**, 2433 (1999)
125. V.V. Singh, U. Kumar, S.N. Tripathi, A.K. Singh, *Dalton Trans.* **43**, 12555 (2014)
126. Z. Xu, C. Shen, Y. Hou, H. Gao, S. Sun, *Chem. Mater.* **21**, 1778 (2009)
127. W. Bu, Z. Chen, F. Chen, J. Shi, *J. Phys. Chem. C.* **113**, 12176 (2009)
128. L. Manna, E.C. Scher, A.P. Alivisatos, *J. Am. Chem. Soc.* **122**, 12700 (2000)
129. L.D. Nyamen, V.S.R. Pullabhotla, A.A. Nejo, P. Ndifon, N. Revaprasadu, *New J. Chem.* **35**, 1133 (2011)
130. J.M. Rawson, R.E.P. Winpenny, *Coord. Chem. Rev.* **139**, 313 (1995)
131. K. Kandasamy, H.B. Singh, S.K. Kulshreshtha, *J. Chem. Sci.* **121**, 293 (2009)
132. X.G. Peng, L. Manna, W.D. Yang, J. Wickham, E.C. Scher, A. Kadavanich, A.P. Alivisatos, *Nature.* **404**, 59 (2000)
133. N. Pradhan, S. Efrima, *J. Am. Chem. Soc.* **125**, 2050 (2003)
134. N. Pradhan, B. Katz, S. Efrima, *J. Phys. Chem. B.* **107**, 13843 (2003)
135. Y. Li, X. Li, C. Yang, Y. Li, *J. Phys. Chem. B.* **108**, 16002 (2004)
136. W.W. Yu, Y.A. Wang, X.G. Peng, *Chem. Mater.* **15**, 4300 (2003)
137. X.G. Peng, *Adv. Mater.* **15**, 459 (2003)
138. C. Amiens, B. Chaudret, D. Ciuculescu-Pradines, V. Colliere, K. Fajerweg, P. Fau, M. Kahn, A. Maisonnat, K. Soulantica, K. Philippot, *New J. Chem.* **37**, 3374 (2013)
139. G.A. Seisenbaeva, V.G. Kessler, *Nanoscale.* **6**, 6229 (2014)
140. M.A. Malik, M. Afzaal, P. O'Brien, *Chem. Rev.* **110**, 4417 (2010)
141. M. Nell, J. Marohn, G. Mclendon, *J. Phys. Chem. B.* **94**, 4359 (1990)
142. L. Spanhel, M. Haase, H. Weller, A. Henglein, *J. Am. Chem. Soc.* **109**, 5649 (1987)
143. M. Kim, H. Kim, S. Lee, S. Sohn, *Mol. Cryst. Liq. Cryst.* **564**, 162 (2012)
144. J. Xiao, B. Wen, R. Melnik, Y. Kawazoe, X. Zhanga, *Phys. Chem.* **16**, 14899 (2014)
145. G.B. Shombe, E.B. Mubofu, S. Mlowe, N. Revaprasadu, *Mater. Sci. Semicond. Proces.* **43**, 230 (2016)
146. R. Banerjee, R. Jayakrishnan, P. Ayyub, *J. Phys. Condens. Matter.* **12**, 10647 (2000)
147. C. Ricolleau, L. Audinet, M. Gandais, T. Gacoin, *Eur. Phys. J.* **9**, 565 (1999)
148. N.L. Botha, P.A. Ajibade, *Mater. Sci. Semicond. Proces.* **43**, 149 (2016)
149. M. Ghiasi, A. Malekzadeh, H. Mardani, *Mater. Sci. Semicond. Proc.* **42**, 311 (2016)
150. S. Zinatloo-Ajabshir, M. Salavati-Niasari, M. Hamadianian, *J. Mater. Sci. Mater. Electron.* **27**, 998 (2016)
151. Z.R. Ranjbar, A. Morsali, *Ultrason. Sonochem.* **18**, 644 (2011)
152. M.H. Habibi, E. Askari, *Synth. React. Inorg., Met.-Org., Nano-Met. Chem.* **43**, 406 (2013)
153. L.A. Saghatforoush, R. Mehdizadeh, F. Chalabian, *Transition Met. Chem.* **35**, 903 (2010)
154. A.D. Khalaji, D. Das, *J. Therm. Anal. Calorim.* **114**, 671 (2013)
155. M.S. Refat, M.Y. El-Sayed, A.M. Adam, *J. Mol. Struct.* **1038**, 62 (2013)
156. A.S. Burlov, V.N. Ikorskii, S.A. Nikolaevskii, YuV Koschlenko, V.G. Vlasenko, Ya.V. Zubavichus, A.I. Uraev, I.S. Vasilchenko, D.A. Garnovskii, G.S. Borodkin, A.D. Garnovskii, *Russ. J. Inorg. Chem.* **53**, 1566 (2008)
157. A.D. Garnovskii, I.S. Vasilchenko, D.A. Garnovskii, A.S. Burlov, A.I. Uraev, *Ros. Khim. Zh. (Mendeleev Chem. J.)* **53**, 100 (2009)
158. S.A. Nikolaevskii, A.S. Burlov, A.S. Bogomyakov, V.G. Vlasenko, A.D. Garnovskii, A.G. Starikov, Ya.V. Zubavichus, I.S. Vasilchenko, S.I. Levchenkov, A.I. Uraev, *Russ. J. General Chem.* **82**, 1770 (2008)
159. A.S. Burlov, V.G. Vlasenko, Ya.V. Zubavichus, S.I. Levchenkov, YuV Koschlenko, A.S. Bogomyakov, S.A. Nikolaevskii, D.A. Garnovskii, A.I. Uraev, T.V. Lifintseva, E.V. Korshunova, *Russ. J. Coord. Chem.* **39**, 219 (2013)
160. A.D. Pomogailo, A.S. Burlov, N.D. Golubeva, L.A. Petrova, S.A. Mashchenko, S.I. Pomogailo, G.I. Dzhardimalieva, A.D. Garnovskii, *Inorg. Mater.* **47**, 876 (2011)

161. A.D. Pomogailo, G.I. Dzhardimalieva, S.I. Pomogailo, N.D. Golubeva, G.V. Shilov, E.A. Dzhavadyan, A.S. Burlov, S.A. Mashchenko, D.A. Garnovskii, *Izv. Akad. Nauk. Ser. Khim.* **139** (2016)
162. B.A. Komarov, A.T. Kapasharov, E.A. Dzhavadyan, V.A. Lesnichaya, G.I. Dzhardimalieva, A.S. Burlov, A.I. Uraev, S.A. Mashchenko, D.A. Garnovskii, A.D. Pomogailo, *Russ. Chem. Bull.* **64**, 936 (2015)
163. N.B. Shitova, P.G. Tsyrunnikov, D.A. Shlyapin, P.S. Barbashova, D.I. Kochubei, V.I. Zaikovskii, *J. Struct. Chem.* **50**, 268 (2009)
164. G. Carotenuto, B. Martorana, P.B. Perlo, L. Nicolais, *J. Mater. Chem.* **13**, 2927 (2003)
165. A.S. Susha, M. Ringler, A. Ohlinger, M. Paderi, N. LiPira, G. Carotenuto, A.L. Rogach, J. Feldman, *Chem. Mater.* **20**, 6169 (2008)
166. F. Capezzuto, G. Carotenuto, F. Antolini, E. Burresti, M. Palomba, P. Perlo *Exp. Polym. Lett.* **3**, 219 (2009)
167. F. Antolini, A. Ghezlbash, C. Esposito, E. Trave, L. Tapfer, B.A. Korgel, *Mater. Lett.* **60**, 1095 (2006)
168. G. Carotenuto, L. Nicolais, P. Perlo, *Polym. Eng. Sci.* 1016 (2006)
169. A. Petrella, M. Tamborra, M.L. Curri, M. Striccolli, P.D. Cozzoli, A. Adostano, *J. Phys. Chem. B* **109**, 1554 (2005)
170. G. Carotenuto, G. Pepe, D. Davino, B. Martorana, P. Perlo, D. Acierno, L. Nicolais, *Microw. Opt. Technol. Lett.* **48**, 2505 (2006)
171. E.A. Lewis, P.D. McNaughter, Z. Yin, Y. Chen, J.R. Brent, S.A. Saah, J. Raftery, J.A.M. Awudza, M.A. Malik, P. O'Brien, S.J. Haigh, *Chem. Mater.* **27**, 2127 (2015)
172. T. Di Luccio, A.M. Laera, L. Tapfer, S. Kempter, R. Kraus, B. Nickel, *J. Phys. Chem. B.* **110**, 12603 (2006)
173. D. Saikia, P.K. Saikia, P.K. Gogoi, M.R. Das, P. Sengupta, M.V. Shelke, *Mater. Chem. Phys.* **131**, 223 (2011)
174. I.C. McNeill, J.J. Liggat, *Polym. Degrad. Stabil.* **29**, 93 (1990)
175. I.C. McNeill, J.J. Liggat, *Polym. Degrad. Stabil.* **37**, 25 (1992)
176. S.M. Humphrey, M.E. Grass, S.E. Habas, L. Niesz, G.A. Somorjai, T.D. Tilley, *Nano Lett.* **7**, 785 (2007)
177. Y. Zhang, M.E. Grass, S.E. Habas, F. Tao, T. Zhang, P. Yang, G.A. Somorjai, *J. Phys. Chem. C.* **111**, 12243 (2007)
178. A.D. Pomogailo, *Ros. Khim. Zh. (Mendeleev Chem. J.)* **46**, 64 (2002)
179. Y.Y. Wang, Q. Shi, Q.Z. Shi, Y.C. Gao, X. Hou, *Polyhedron* **19**, 891 (2000)
180. Y.Y. Wang, Q. Shi, Q.Z. Shi, *Acta Chim. Sinica.* **58**, 675 (2000)
181. V.A. Shershnev, G.I. Dzhardimalieva, D.P. Kiryuhin, V.A. Zhorin, A.D. Pomogailo, *Izv. Akad. Nauk. Ser. Khim.* 1649 (2013)
182. N.N. Volkova, G.I. Dzhardimalieva, B. E. Krisyuk, N.V. Chukanov, V.A. Shershnev, G.V. Shilov, *Izv. Akad. Nauk. Ser. Khim.* (2016)
183. V.A. Shershnev, G.V. Shilov, G.I. Dzhardimalieva, A.D. Pomogailo, M. Izydorczak, M. Leonowicz, *Macromol. Symp.* **317–318**, 180 (2012)
184. B. Wu, W.-M. Lu, X.-M. Zheng, *Chin. J. Chem.* **20**, 846 (2002)
185. B. Wu, W. Lu, X. Zheng, *Transit. Met. Chem.* **28**, 323 (2003)
186. B. Wu, W. Lu, X. Zheng, *J. Coord. Chem.* **56**, 65 (2003)
187. Y. Lu, W. Lu, B. Wu, L. Wang, *J. Coord. Chem.* **53**, 15 (2001)
188. P.A. Vasiljev, *Zh. Neorg. Khim.* **30**, 1688 (1994)
189. P.A. Vasiljev, A.L. Ivanov, O.N. Rubacheva, A.N. Glebov, *Zh. Neorg. Khim.* **41**, 1747 (1996)
190. A. Gronowski, Z. Wojtczak, *J. Therm. Anal.* **26**, 233 (1983)
191. Z. Wojtczak, A. Gronowski, *J. Therm. Anal.* **36**, 2357 (1990)
192. A.S. Rozenberg, E.I. Aleksandrova, *Izv. Akad. Nauk. Ser. Khim.* 72 (1996)
193. A.S. Rozenberg, N.V. Chukanov, *Izv. Akad. Nauk. Ser. Khim.* 350 (1996)
194. A.S. Rozenberg, V.P. Syepanov, *Izv. Akad. Nauk. Ser. Khim.* 1406 (1996)
195. S.V. Davidovich, F.F. Veher, T.F. Gusev, *Thermochim. Acta.* **89**, 383 (1985)

196. I.V. Fedorova, V.A. Shurov, A.A. Fedorov, M.S. Gaisinovich, Zh Prikl. Khim. **65**, 736 (1992)
197. I.V. Arkhangel'skii, L.N. Komissarova, A. Gorski, A. Kras'nicka, J. Therm. Anal. **32**, 1234 (1987)
198. A. Gorski, A. Kras'nicka, J. Therm. Anal. **32**, 1345 (1987)
199. E. Tirosh, G. Shemer, G. Markovich, Chem. Mater. **18**, 465 (2006)
200. N. Bao, L. Shen, Y. Wang, P. Padhan, A. Gupta, J. Am. Chem. Soc. **129**, 12374 (2007)
201. J.H. Park, N.M. Hwang, T. Hyeon, Nat. Mater. **3**, 891 (2004)
202. S. Sun, H. Zeng, D.B. Robinson, S. Raoux, P.M. Rice, S.X. Wang, G. Li, J. Am. Chem. Soc. **126**, 273 (2004)
203. S. Sun, H. Zeng, J. Am. Chem. Soc. **124**, 8204 (2002)
204. M.M. Lin, D.K. Kim, J. Nanopart. Res. **14**, 688 (2012)
205. K. Liu, H. You, G. Jia, Y. Zheng, Y. Song, M. Yang, Y. Huang, H. Zhang, Crystal. Growth Des. **9**, 3519 (2009)
206. B.L. Chen, Y. Yang, F. Zapata, G.N. Lin, G.D. Qian, E.B. Lobkovsky, Adv. Mater. **19**, 1693 (2007)
207. J.R. William, M.L. Kathryn, H.Y. An, W.L. Lin, W.B. Lin, J. Am. Chem. Soc. **128**, 9024 (2006)
208. V.G. Pol, O. Palchik, A. Gedanken, I. Felner, J. Phys. Chem. B. **106**, 9737 (2002)
209. K.-L. Wong, G.-L. Law, M.B. Murphy, P.A. Tanner, W.-T. Wong, P.K. Lam, L.M. Hon-Wah, Inorg. Chem. **47**, 5190 (2008)
210. L. Zhang, J. Luo, M. Wu, H. Jiu, Q.W. Chen, Mater. Lett. **61**, 4452 (2007)
211. H. Yang, D. Zhang, L. Shi, J. Fang, Acta Mater. **56**, 955 (2008)
212. J. Goldberg, R. Fan, P.D. Yang, Acc. Chem. Res. **39**, 239 (2006)
213. E.I. Aleksandrova, G.I. Dzhardimalieva, A.S. Rozenberg, A.D. Pomogailo, Izv. Akad. Nauk. Ser. Khim. **303** (1993)
214. E.I. Aleksandrova, G.I. Dzhardimalieva, A.S. Rozenberg, A.D. Pomogailo, Izv. Akad. Nauk. Ser. Khim. **308** (1993)
215. A.S. Rozenberg, G.I. Dzhardimalieva, A.D. Pomogailo, Polym. Adv. Technol. **9**, 527 (1998)
216. A.S. Rozenberg, G.I. Dzhardimalieva, N.V. Chukanov, A.D. Pomogailo, Coll. J. **67**, 57 (2005)
217. A.S. Rozenberg, E.I. Aleksandrova, G.I. Dzhardimalieva, A.H. Титков, A.D. Pomogailo, Izv. Akad. Nauk. Ser. Khim. 1743 (1993)
218. A.S. Rozenberg, E.I. Aleksandrova, G.I. Dzhardimalieva, N.V. Kiryakov, P.E. Chizhov, V.I. Petinov, A.D. Pomogailo, Izv. Akad. Nauk. Ser. Khim. 885 (1995)
219. A.D. Pomogailo, A.S. Rozenberg, G.I. Dzhardimalieva, A.M. Bochkina, S.I. Pomogailo, N.D/ Golubeva, V.M. Grischenko, Neorg. Mater. **42**, 164 (2006)
220. A.D. Pomogailo, G.I. Dzhardimalieva, A.S. Rozenberg, V.N. Kestelman, J. Thermoplastic Composite Mater. **20**, 151 (2007)
221. A.S. Rozenberg, E.I. Aleksandrova, N.P. Ivleva, G.I. Dzhardimalieva, A.V. Raevskii, O.I. Kolesova, I.E. Uflyand, A.D. Pomogailo, Izv. Akad. Nauk. Ser. Khim. 265 (1998)
222. A.T. Shuvaev, A.S. Rozenberg, G.I. Dzhardimalieva, N.P. Ivleva, V.G. Vlasenko, T.I. Nedoseikina, T.A. Lubeznova, I.E. Uflyand, A.D. Pomogailo, Izv. Akad. Nauk. Ser. Khim. 1505 (1998)
223. A.S. Rozenberg, A.V. Raevskii, E.I. Aleksandrova, O.I. Kolesova, G.I. Dzhardimalieva, A.D. Pomogailo, Izv. Akad. Nauk. Ser. Khim. 862 (2001)
224. R.A. Lidin, L.L. Andreeva, V.A. Molochko, *Spravochnik po Neorganicheskoi Khimii. Konstanty Neorganicheskikh Veshstv* (The Handbook on Inorganic Chemistry. The Constants of Inorganic Substances). (Khimiya, Moscow, 1987)
225. A.D. Pomogailo, G.I. Dzhardimalieva, A.S. Rozenberg, D.N. Muraviev, J. Nanoparticle Res. **5**, 497 (2003)
226. G.I. Dzhardimalieva, A.D. Pomogailo, S.P. Davtyan, V.I. Ponomarev, Izv. Akad. Nauk. Ser. Khim 1531 (1988)
227. G.I. Dzhardimalieva, A.D. Pomogailo, Macromol. Symp. **131**, 19 (1998)

228. N.P. Porollo, Z.A. Aliev, G.I. Dzhardimalieva, I.N. Ivleva, I.E. Uflyand, A.D. Pomogailo, N.S. Ovanesyan, *Russ. Chem. Bull.* **46**, 362 (1997)
229. A.S. Rozenberg, G.I. Dzhardimalieva, A.D. Pomogailo, *Dokl. Akad. Nauk* **356**, 66 (1997)
230. Y.M. Shulga, O.S. Roschupkina, G.I. Dzhardimalieva, I.V. Chernushevich, A.F. Dodonov, Y.V. Baldokhin, P.Y. Kolotirkin, A.S. Rozenberg, A.D. Pomogailo, *Izv. Akad. Nauk. Ser. Khim.* 1739 (1993)
231. C. McNeiel, S.M. Sadeghi, *Polym. Degrad. Stabilit.* **26**, 233 (1990)
232. N.V. Chukanov, I.V. Kumpanenko, V.V. Losev, N.G. Entelis, *Dokl. Akad. Nauk.* **261**, 135 (1981)
233. R. Das, P. Pachfule, R. Banerjee, P. Poddar, *Nanoscale.* **4**, 591 (2012)
234. R. Coskun, M. Yigitoglu, M. Sacak, *J. Appl. Polym. Sci.* **75**, 766 (2000)
235. D. Bilba, L. Bejan, L. Tofan, *Croat. Chem. Acta.* **71**, 155 (1998)
236. B.W. Zhang, K. Fischer, D. Bieniek, A. Kettrup, *React. Polym.* **24**, 49 (1994)
237. R.X. Liu, B.W. Zhang, H.X. Tang, *J. Appl. Polym. Sci.* **70**, 7 (1998)
238. N. Kabay, H. Egawa, *Sep. Sci. Technol.* **29**, 135 (1994)
239. R. Lei, X. Jie, X. Jun, Z. Ruijun, *J. Appl. Polym. Sci.* **53**, 325 (1994)
240. E.H. Rifi, M.J.F. Leroy, J.P. Brunette, C. Schloesserbecker, *Solvent Extr. Ion Exch.* **12**, 1103 (1994)
241. H. Kubota, Y. Shigehisa, *J. Appl. Polym. Sci.* **56**, 147 (1995)
242. N. Pekel, N. Sahiner, O. Güven, *J. Appl. Polym. Sci.* **81**, 2324 (2001)
243. I.H. Park, J.M. Suh, *Angew. Makromol. Chem.* **239**, 121 (1996)
244. G. Moroi, D. Bilba, N. Bilba, C. Ciobanu, *Polym. Degrad. Stabil.* **91**, 535 (2006)
245. M.N. Patel, V.J. Patel, *Indian J. Chem. A.* **28**, 428 (1989)
246. M.N. Patel, D.H. Sutaria, G.J. Patel, *Synth. React. Inorg. Metal-Org. Chem.* **24**, 401 (1994)
247. O.G. Marambio, G. del C. Pizzaro, M. Jeria-Orell, M. Huerta, C. Olea-Azar, W.D. Habicher, *J. Polym. Sci.: Part A: Polym. Chem.* **43**, 4933 (2005)
248. I. Kaya, A. Solguntekin, *J. Appl. Polym. Sci.* **113**, 1994 (2009)
249. H. Suda, K. Haraya, *Chem. Commun.* **93** (1997)
250. F. Rodeiguez-Reinoso, *Carbon* **36**, 159 (1998)
251. Y. Fang, D. Gu, Y. Zou, Z. Wu, F. Li, R. Che, Y. Deng, B. Tu, D. Zhao, *Angew. Chem. Int. Ed.* **49**, 7987 (2010)
252. J. Maruyama, K. Sumino, M. Kawaguchi, I. Abe, *Carbon* **42**, 3115 (2004)
253. Y. Tao, M. Endo, M. Inagaki, K. Kaneko, *J. Mater. Chem.* **21**, 313 (2011)
254. J. Lee, J. Kim, T. Hyeon, *Adv. Mater.* **18**, 2073 (2006)
255. Y. Xia, Z. Yang, R. Mokaya, *Nanoscale.* **2**, 639 (2010)
256. T.-Y. Ma, L. Liu, Z.-Y. Yuan, *Chem. Soc. Rev.* **42**, 3977 (2013)
257. B. Liu, H. Shioyama, T. Akita, Q. Xu, *J. Am. Chem. Soc.* **130**, 5390 (2008)
258. Q. Tian, Z. Zhang, L. Yang, S. Hirano, *Carbon* **93**, 887 (2015)
259. C.P. Li, J. Chen, C.S. Liu, M. Du, *Chem. Commun.* **51**, 2768 (2015)
260. R. Matsuoka, R. Toyoda, R. Sakamoto, M. Tsuchiya, K. Hoshiko, T. Nagayama, Y. Nonoguchi, K. Sugimoto, E. Nishibori, T. Kawai, H. Nishihara, *Chem. Sci.* **6**, 2853 (2015)
261. W. Xia, A. Mahmood, R. Zou, Q. Xu, *Energy Environ. Sci.* **8**, 1837 (2015)
262. M. Hu, J. Reboul, S. Furukawa, N.L. Torad, Q. Ji, P. Srinivasu, K. Ariga, S. Kitagawa, Y. Yamauchi, *J. Am. Chem. Soc.* **134**, 2864 (2012)
263. W. Chaikittisilp, M. Hu, H. Wang, H.-S. Huang, T. Fujita, K.C.-W. Wu, L.-C. Chen, Y. Yamauchi, K. Ariga, *Chem. Commun.* **48**, 7259 (2012)
264. N.L. Torad, M. Hu, Y. Kamachi, K. Takai, M. Imura, M. Naito, Y. Yamauchi, *Chem. Commun.* **49**, 2521 (2013)
265. L. Radhakrishnan, J. Reboul, S. Furukawa, P. Srinivasu, S. Kitagawa, Y. Yamauchi, *Chem. Mater.* **23**, 1225 (2011)
266. H.-L. Jiang, B. Liu, Y.-Q. Lan, K. Kuratani, T. Akita, H. Shioyama, F. Zong, Q. Xu, *J. Am. Chem. Soc.* **133**, 11854 (2011)
267. J. Hu, H. Wang, Q. Gao, H. Guo, *Carbon* **48**, 3599 (2010)
268. H. Li, M. Eddaoudi, M. O'Keeffe, O.M. Yaghi, *Nature* **402**, 276 (1999)

269. X.C. Huang, Y.Y. Lin, J.P. Zhang, X.M. Chen, *Angew. Chem. Int. Ed.* **45**, 1557 (2006)
270. N.L. Torad, Y. Li, S. Ishihara, K. Ariga, Y. Kamachi, H.-Y. Lian, H. Hamoudi, Y. Sakka, W. Chaikittisilp, K.C.-W. Wu, Y. Yamauchi, *Chem. Lett.* **43**, 717 (2014)
271. R.R. Salunkhe, Y. Kamachi, N.L. Torad, S.M. Hwang, Z. Sun, S.X. Dou, J.H. Kim, Y. Yamauchi, *J. Mater. Chem. A* **2**, 19848 (2014)
272. S.J. Yang, T. Kim, J.H. Im, Y.S. Kim, K. Lee, H. Jung, C.R. Park, *Chem. Mater.* **24**, 464 (2012)
273. A. Comotti, S. Bracco, P. Sozzani, S. Horike, R. Matsuda, J. Chen, M. Takata, Y. Kubota, S. Kitagawa, *J. Am. Chem. Soc.* **130**, 13664 (2008)
274. B. Liu, H. Shioyama, H.L. Jiang, X.B. Zhang, Q. Xu, *Carbon* **48**, 456 (2010)
275. Z. Han, Y. Yu, Y. Zhang, B. Dong, A. Kong, Y. Shan, *J. Mater. Chem. A* **3**, 23716 (2015)
276. J.P. Paraknowitsch, J. Zhang, D. Su, A. Thomas, M. Antonietti, *Adv. Mater.* **22**, 87 (2010)
277. Y. Wang, J. Zhang, X. Wang, M. Antonietti, H. Li, *Angew. Chem. Int. Ed.* **49**, 3356 (2010)
278. A. Thomas, A. Fischer, F. Goettmann, M. Antonietti, J.O. Müller, R. Schloegl, J.M. Carlssonc, *J. Mater. Chem.* **18**, 4893 (2008)
279. W. Chaikittisilp, N.L. Torad, C. Li, M. Imura, N. Suzuki, S. Ishihara, K. Ariga, Y. Yamauchi, *Chem. Eur. J.* **20**, 4217 (2014)
280. N.L. Torad, M. Hu, S. Ishihara, H. Sukegawa, A.A. Belik, M. Imura, K. Ariga, Y. Sakka, Y. Yamauchi, *Small* **10**, 2096 (2014)
281. X. Jin, V.V. Balasubramanian, S.T. Selvan, D.P. Sawant, M.A. Chari, G.O. Lu, A. Vinu, *Angew. Chem. Int. Ed.* **48**, 7884 (2009)
282. M. Hu, J. Reboul, S. Furukawa, L. Radhakrishnan, Y. Zhang, P. Srinivasu, H. Iwai, H. Wang, Y. Nemoto, N. Suzuki, S. Kitagawa, Y. Yamauchi, *Chem. Commun.* **47**, 8124 (2011)
283. W. Bak, H.S. Kim, H. Chun, W.C. Yoo, *Chem. Commun.* **51**, 7238 (2015)
284. L. Zhang, Y.H. Hu, *J. Phys. Chem. C* **114**, 2566 (2010)
285. M. Zhang, Y.-L. Huang, J.-W. Wang, T.-B. Lu, *J. Mater. Chem. A* **4**, 1819 (2016)
286. L. Aboutorabi, A. Morsali, *Inorg. Chim. Acta* **363**, 2506 (2010)
287. H. Sadeghzadeh, A. Morsali, *J. Coord. Chem.* **63**, 713 (2010)
288. B. Mirtamizdoust, D.C. Bienko, Y. Hanifehpour, E.R.T. Tiekink, V.T. Yilmaz, P. Talem, S.W. Joo, *J. Inorg. Organomet. Polym.* **26**, 819 (2016)
289. S. Aghabeygi, F. Bigdeli, A. Morsali, *J. Inorg. Organomet. Polym. Mater.* **22**, 526 (2012)
290. H.-Y. Shi, B. Deng, S.-L. Zhong, L. Wang, A.-W. Xu, *J. Mater. Chem.* **21**, 12309 (2011)
291. R. Zboril, L. Machala, M. Mashlan, V. Sharma, *Cryst. Growth Des.* **4**, 1317 (2004)
292. M. Hu, J.-S. Jiang, Y. Zeng, *Chem. Commun.* **46**, 1133 (2010)
293. W. Cho, S. Park, M. Oh, *Chem. Commun.* **47**, 4138 (2011)
294. X. Xu, R. Cao, S. Jeong, J. Cho, *Nano Lett.* **12**, 4988 (2012)
295. F. Zhang, L. Hao, L. Zhang, X. Zhang, *Int. J. Electrochem. Sci.* **6**, 2943 (2011)
296. B. Liu, X. Zhang, H. Shioyama, T. Mukai, T. Sakai, Q. Xu, *J. Power Sour.* **195**, 857 (2010)
297. C. Li, X. Yin, L. Chen, Q. Li, T. Wang, *Chem. Eur. J.* **16**, 5215 (2010)
298. F. Zhang, D.-D. Qi, X.-G. Zhang, *Int. J. Electrochem. Sci.* **11**, 189 (2016)
299. L. Hu, Y. Huang, F. Zhang, Q. Chen, *Nanoscale* **5**, 4186 (2013)
300. S. Zhang, H. Liu, C. Sun, P. Liu, L. Li, Z. Yang, X. Feng, F. Huo, X. Lu, *J. Mater. Chem. A* **3**, 5294 (2015)
301. M. Moeinian, K. Akhbari, *J. Inorg. Organomet. Polym.* **26**, 1 (2016)
302. B. Mirtamizdoust, B. Shaabani, A. Khandar, H.-K. Fun, S. Huang, M. Shadman, P. Hojati-Talemi, Z. Anorg, *Allg. Chem.* **638**, 844 (2012)
303. Y. Hanifehpour, B. Mirtamizdoust, S.W. Joo, *J. Inorg. Organomet. Polym.* **22**, 816 (2012)
304. Y. Hanifehpour, B. Mirtamizdoust, A.R. Farzam, S.W. Joo, *J. Inorg. Organomet. Polym.* **22**, 957 (2012)
305. F. Bigdeli, A. Morsali, *Mater. Lett.* **64**, 4 (2010)
306. K. Bijanzad, A. Tadjarodi, O. Akhavan, *Chin. J. Catal.* **36**, 742 (2015)
307. H. Kim, M. Park, H. Lee, O.S. Jung, *Dalton Trans.* **44**, 8198 (2015)
308. F. Marandi, L. Hashemi, A. Morsali, H. Krautscheid, *J. Inorg. Organomet. Polym.* **26**, 962 (2016)

309. G.M. Duffy, S.C. Pillai, D.E. McCormack, *Smart Mater. Struct.* **16**, 1379 (2007)
310. F. Zhang, F.-L. Bei, J.-M. Cao, X. Wang, *J. Solid State Chem.* **181**, 143 (2008)
311. V. Safarifard, A. Morsali, *Ultrason. Sonochem.* **19**, 1227 (2012)
312. S.K. Pasha, V.S.V. Satyanarayana, A. Sivakumar, K. Chidambaram, L.J. Kennedy, *Chin. Chem. Lett.* **22**, 891 (2011)
313. A.V. Borhadea, B.K. Uphadeb, D.R. Tope, *J. Chem. Sci.* **125**, 583 (2013)
314. L. Hashemi, A. Aslani, A. Morsali, *J. Inorg. Organomet. Polym.* **22**, 867 (2012)
315. A. Aslani, A. Morsali, *Inorg. Chim. Acta* **362**, 5012 (2009)
316. H. Sadeghzadeh, A. Morsali, *Ultrason. Sonochem.* **18**, 80 (2011)
317. S. Saeednia, P. Iranmanesh, H.A. Rudbari, L. Saeednia, *J. Macromol. Sci. Part A: Pure Appl. Chem.* **53**, 227 (2016)
318. R. Gupta, S. Sanotra, H. Nawaz Sheikh, B. Lal Kalsotra, V. Kumar Gupta, Rajnikant, *J. Coord. Chem.* **65**, 3917 (2012)
319. Z.-F. Liu, A.-X. Zhu, C.-K. Lam, G.-W. Xie, C.-L. Liang, X.-M. Chen, Z.-P. Qiao, *Cryst. Eng. Comm.* **11**, 1303 (2009)
320. L. Wang, H. Zou, Y. Li, X. Li, S. Zhong, *Mater. Manufact. Proc.* (2016)
321. S. Jin, J.P. Hill, Q. Ji, L. Kumar Shrestha, K. Ariga, *J. Mater. Chem. A*, **4**, 5737 (2016)
322. M.S. Yazdan Parast, A. Morsali, *Inorg. Chem. Commun.* **14**, 450 (2011)
323. L. Hashemi, A. Morsali, *J. Inorg. Organomet. Polym.* **22**, 272 (2012)
324. M.A. Alavi, A. Morsali, S.W. Joo, B.K. Min, *Ultrason. Sonochem.* **22**, 349 (2015)
325. A. Mehrani, A. Morsali, Y. Hanifehpour, S.W. Joo, *Ultrason. Sonochem.* **21**, 1430 (2014)
326. W. Cho, Y.H. Lee, H.J. Lee, M. Oh, *Chem. Commun.* 4756 (2009)
327. Z. Li, Y. Xiong, Y. Xie, *Nanotechnology* **16**, 2303 (2005)
328. S. Hei, Y. Jin, F. Zhang, *J. Chem.* **2014**, Article ID 546956 (2014)
329. F. Meng, Z. Fang, Z. Li, W. Xu, M. Wang, Y. Liu, J. Zhang, W. Wang, D. Zhao, X. Guo, *J. Mater. Chem. A*, **1**, 7235 (2013)
330. N. Nasihat Sheno, A. Morsali, S. Woo Joo, *Mater. Lett.* **117**, 31 (2014)
331. W. Cho, Y.H. Lee, H.J. Lee, M. Oh, *Adv. Mater.* **23**, 1720 (2011)
332. M. Hu, A.A. Belik, M. Imura, K. Mibu, Y. Tsujimoto, Y. Yamauchi, *Chem. Mater.* **24**, 2698 (2012)
333. L. Zhang, H.B. Wu, S. Madhavi, H.H. Hng, X.W. Lou, *J. Am. Chem. Soc.* **134**, 17388 (2012)
334. L. Zhang, H.B. Wu, R. Xu, X.W. Lou, *CrystEngComm*, **15**, 9332 (2013)
335. K.J. Lee, T.-H. Kim, T.K. Kim, J.H. Lee, H.-K. Song, H.R. Moon, *J. Mater. Chem. A*, **2**, 14393 (2014)
336. K. Akhbari, A. Morsali, *J. Coord. Chem.* **64**, 3521 (2011)
337. M.Y. Masoomi, A. Morsali, *Ultrason. Sonochem.* **28**, 240 (2016)
338. A. Abbasi, M. Gharib, M. Najafi, *J. Sci. I. R. Iran.* **27**, 217 (2016)
339. L.-B. Ni, R.-H. Zhang, Q.-X. Liu, W.-S. Xia, H. Wang, Z.-H. Zhou, *J. Solid State Chem.* **182**, 2698 (2009)
340. J. Rautio, P. Per, J. Honkamo, H. Jantunen, *Microchem. J.* **91**, 272 (2009)
341. K.S. Cho, J.I. Hong, C.I. Chung, *Polym. Eng. Sci.* **44**, 1702 (2004)
342. A. Tahmasian, A. Morsali, *Inorg. Chim. Acta.* **387**, 327 (2012)
343. A. Morsali, A. Panjehpour, *Inorg. Chim. Acta.* **391**, 210 (2012)
344. A. Hosseinian, S. Jabbari, A. Reza Mahjoub, M. Movahedi, *J. Coord. Chem.* **65**, 2623 (2012)
345. J.H. Lee, Y.J. Sa, T.K. Kim, H.R. Moon, S.H. Joo, *J. Mater. Chem. A*, **2**, 10435 (2014)
346. H. Jiang, C. Wang, H. Wang, M. Zhang, *Mater. Lett.* **168**, 17 (2016)
347. T.K. Kim, K.J. Lee, J.Y. Cheon, J.H. Lee, S.H. Joo, H.R. Moon, *J. Am. Chem. Soc.* **135**, 8940 (2013)
348. Z.-M. Liu, S.-H. Wu, S.-Y. Jia, F.-X. Qin, S.-M. Zhou, H.-T. Ren, P. Na, Y. Liu, *Mater. Lett.* **132**, 8 (2014)
349. J. Xu, Q. Liu, W.-Y. Sun, *Solid State Sci.* **12**, 1575 (2010)
350. K. Akhbari, N.B. Bahman, A. Morsali, P. Retailleau, *J. Iran. Chem. Soc.* **13**, 165 (2016)

351. S.Y. Moon, M.W. Park, T.H. Noh, O.-S. Jung, J. Mol. Struct. **1054–1055**, 326 (2013)
352. F. Marandi, L. Hashemi, A. Morsali, H. Krautscheid, Ultrason. Sonochem. **32**, 86 (2016)
353. L. Chen, C. Zhao, Z. Wei, S. Wang, Y. Gu, Mater. Lett. **65**, 446 (2011)
354. Z. Rashidi, A. Morsali, J. Mol. Struct. **936**, 206 (2009)
355. L. Hashemi, A. Morsali, J. Inorg. Organomet. Polym. **20**, 856 (2010)
356. L. Hashemi, A. Morsali, P. Retailleau, Inorg. Chim. Acta **367**, 207 (2011)
357. F. Shahangi Shirazi, K. Akhbari, Inorg. Chim. Acta **436**, 1 (2015)
358. M. Moeinian, K. Akhbari, J. Solid State Chem. **225**, 459 (2015)
359. A. Mehrani, A. Morsali, J. Inorg. Organomet. Polym. **21**, 476 (2011)
360. A. Mehrani, A. Morsali, P. Ebrahimpour, J. Coord. Chem. **66**, 856 (2013)
361. G.H. Shahverdizadeh, F. Hakimi, B. Mirtamizdoust, A. Souidi, P. Hojati-Talemi, J. Inorg. Organomet. Polym. **22**, 903 (2012)
362. L. Hashemi, A. Morsali, J. Coord. Chem. **64**, 4088 (2011)
363. B. Mirtamizdoust, B. Shaabani, A. Khandar, H. Pourradi, Y. Abbasityula, H. Goudarziafshar, D. Viterbo, G. Croce, P. Hojati-Talemi, J. Inorg. Organomet. Polym. **22**, 1293 (2012)
364. M. Hossienifard, L. Hashemi, V. Amani, K. Kalateh, A. Morsali, J. Inorg. Organomet. Polym. **21**, 527 (2011)
365. Z.R. Ranjbar, A. Morsali, P. Retailleau, Inorg. Chim. Acta **376**, 486 (2011)
366. G. Mera, E. Ionescu, Silicon-Containing Pre ceramic Polymers, in *Encyclopedia of Polymer Science and Technology* (John Wiley & Sons, Inc., Hoboken, NJ, USA, 2013)
367. P. Colombo, G. Mera, R. Riedel, G.D. Sorarù, J. Am. Ceram. Soc. **93**, 1805 (2010)
368. E. Ionescu, R. Riedel, Polymer Processing of Ceramics, in *Ceramics and Composites Processing Methods*, eds. by N. Bansal, A. Boccaccini (Wiley, Hoboken, NJ, USA, 2012)
369. C. Vakifahmetoglu, D. Zeydanli, P. Colombo, Mater. Sci. Eng. R Rep. **106**, 1 (2016)
370. G. Mera, M. Gallei, S. Bernard, E. Ionescu, Nanomaterials. **5**, 468 (2015)
371. R. Riedel, G. Mera, R. Hauser, A. Kloneczynski, J. Ceram. Soc. Jpn. **114**, 425 (2006)
372. G. Mera, R. Riedel, Organosilicon-Based Polymers as Precursors for Ceramics, in *Polymer Derived Ceramics: From Nanostructure to Applications*, eds. by P. Colombo, R. Riedel, G.D. Soraru, H.-J. Kleebe (DEStech Publications Inc., Lancaster, PA, USA, 2010)
373. E. Ionescu, H.-J. Kleebe, R. Riedel, Chem. Soc. Rev. **41**, 5032 (2012)
374. E. Ionescu, C. Gervais, F. Babonneau, Polymer-to-Ceramic Transformation, in *Polymer Derived Ceramics: From Nanostructure to Applications*, eds. by P. Colombo, R. Riedel, G.D. Soraru, H.-J. Kleebe (DEStech Publications Inc., Lancaster, PA, USA, 2010)
375. M. Zaheer, T. Schmalz, G. Motz, R. Kempe, Chem. Soc. Rev. **41**, 5102 (2012)
376. M.S. Bazarjani, H.-J. Kleebe, M.M. Müller, C. Fasel, M.B. Yazdi, A. Gurlo, R. Riedel, Chem. Mater. **23**, 4112 (2011)
377. M. Zaheer, C.D. Keenan, J. Hermannsdorfer, E. Roessler, G. Motz, J. Senker, R. Kempe, Chem. Mater. **24**, 3952 (2012)
378. M. Zaheer, J. Hermannsdorfer, W.P. Kretschmer, G. Motz, R. Kempe, ChemCatChem **6**, 91 (2014)
379. G. Glatz, T. Schmalz, T. Kraus, F. Haarmann, G. Motz, R. Kempe, Chem. – Eur. J. **16**, 4231 (2010)
380. M. Zaheer, G. Motz, R. Kempe, J. Mater. Chem. **21**, 18825 (2011)
381. T. Schmalz, T. Kraus, M. Guenther, C. Liebscher, U. Glatzel, R. Kempe, G. Motz, Carbon **49**, 3065 (2011)
382. D. Ghoshal, T.K. Maji, T. Mallah, T.-H. Lu, G. Mostafa, N.R. Chaudhuri, Inorg. Chim. Acta. **358**, 1027 (2005)
383. M. Sakamoto, K. Manseki, H. Okawa, Coord. Chem. Rev. **219–221**, 379 (2001)
384. E. Coronado, J.R. Galán-Mascaro, C. Martí-Gastaldo, Inorg. Chem. **46**, 8108 (2007)
385. Z.-G. Gu, S.C. Sevov, J. Mater. Chem. **19**, 8442 (2009)
386. B.-H. Ye, M.-L. Tong, X.-M. Chen, Coord. Chem. Rev. **249**, 545 (2005)
387. I.G. Fomina, ZhV Dobrokhotova, G.G. Aleksandrov, M.L. Kovba, V.I. Zhilov, A.S. Bogomyakov, V.M. Novotortsev, I.L. Eremenko, Russ. Chem. Bull. **59**, 699 (2010)

388. E.V. Orlova, A.E. Goldberg, M.A. Kiskin, P.S. Koroteev, A.L. Emelina, M.A. Bykov, G.G. Aleksandrov, ZhV Dobrokhotova, V.M. Novotortsev, I.L. Eremanko, *Izv. Akad. Nauk. Ser. Khim.* **60**, 2195 (2011)
389. T. Demars, M. Boltoeva, N. Vigier, J. Maynadié, J. Ravaux, C. Genre, D. Meyer, *Eur. J. Inorg. Chem.* **2012**, 3875 (2012)
390. Z.V. Dobrokhotova, N.V. Gogoleva, E.N. Zorina-Tikhonova, M.A. Kiskin, V.V. Chernyshev, A.L. Emelina, M.A. Bukov, A.S. Goloveshkin, I.S. Bushmarinov, A.A. Sidorov, A.S. Bogomyakov, M.L. Kovba, V.M. Novotortsev, I.L. Eremanko, *Eur. J. Inorg. Chem.* **2015**, 3116 (2015)
391. A.V. Gavrikov, P.S. Koroteev, Z.V. Dobrokhotova, A.B. Ilyukhin, N.N. Efimov, D.I. Kirdyankin, M.A. Bykov, M.A. Ryumin, V.M. Novotortsev, *Polyhedron*. **102**, 48 (2015)
392. N. Zauzolkova, Z. Dobrokhotova, A. Lermontov, E. Zorina, A. Emelina, M. Bukov, V. Chernyshev, A. Sidorov, M. Kiskin, A. Bogomyakov, A. Lytvynenko, S. Kolotilov, Y. Velikodnyi, M. Kovba, V. Novotortsev, I. Eremanko, *J. Solid State Chem.* **197**, 379 (2013)
393. M.A. Ryumin, Z.V. Dobrokhotova, A.L. Emelina, M.A. Bukov, N.V. Gogoleva, K.S. Gavrichev, E.N. Zorina-Tikhonova, L.I. Demina, M.A. Kiskin, A.A. Sidorov, I.L. Eremanko, V.M. Novotortsev, *Polyhedron* **87**, 28 (2015)
394. R.A. Rocha, E.N.S. Muccillo, *Chem. Mater.* **15**, 4268 (2003)
395. E. Coronado, C. Martí-Gastaldo, J.R. Galán-Mascarós, M. Cavallini, *J. Am. Chem. Soc.* **132**, 5456 (2010)
396. D. Hong, Y. Yamada, M. Sheehan, S. Shikano, C.-H. Kuo, M. Tian, C.-K. Tsung, S. Fukuzumi, *ACS Sustainable Chem. Eng.* **2**, 2588 (2014)
397. Y. Xia, B. Wang, G. Wang, X. Liu, H. Wang, *ChemElectroChem* **3**, 299 (2016)
398. L. Chen, Y. Shen, J. Bai, C. Wang, *J. Solid State Chem.* **182**, 2298 (2009)
399. K. Akhbari, A. Morsali, *Cryst. Eng. Comm.* **12**, 3394 (2010)
400. R. Bashiri, K. Akhbari, A. Morsali, *Inorg. Chim. Acta.* **362**, 1035 (2009)
401. M. Yamada, R. Ohkawa, M. Miyake, *I.E.E.J. Trans, Electron. Inf. Syst.* **127**, 1342 (2007)
402. B. Folch, J. Larionova, Y. Guari, L. Datas, C. Guerin, *J. Mater. Chem.* **16**, 4435 (2006)
403. Y.W. Koh, C.S. Lai, A.Y. Du, E.R.T. Tiekink, K.P. Loh, *Chem. Mater.* **15**, 4544 (2003)
404. M. Nagarathinam, K. Saravanan, W.L. Leong, P. Balaya, J.J. Vittal, *Cryst. Growth Des.* **9**, 4461 (2009)
405. J.X. Yang, S.M. Wang, X.L. Zhao, Y.P. Tian, S.Y. Zhang, B.K. Jin, X.P. Hao, X.Y. Xu, X. T. Tao, M.H. Jiang, *J. Cryst. Growth.* **310**, 4358 (2008)
406. Y. Meng, G.-H. Wang, S. Bernt, N. Stock, A.-H. Lu, *Chem. Commun.* **47**, 10479 (2011)